Invited lectures

Atmospheric Chemical Measurements Related to Climate Forcing, Ozone Depletion and Air Quality

David Hofmann

Climate Monitoring and Diagnostics Laboratory
U. S. National Oceanic and Atmospheric Administration
Boulder, Colorado, USA

Abstract

Concern for the Earth's environment, it's air, water and general quality of life in the future, has created numerous opportunities for scientists to apply measurement techniques in areas directly related to these problems. A notable example was the measurement program of the late Prof. Werner Lindinger, using the proton transfer resonance – mass spectrometry (PTRMS) technique to detect molecules in the atmosphere which could be used to identify important environmental processes, such as biomass burning, and to make continuous measurements over extended periods of time. Such measurements are directly related to important research areas, for example, the quality of the air we breath and the long-range transport of effluents from industrial and anthropogenic sources.

Similarly, in the field of climate forcing, the greenhouse gases and aerosol particles that do the forcing of climate have to be measured continuously and accurately. Research related to the depletion of stratospheric ozone and the Antarctic ozone hole involve measurements of ozone itself but also all those molecules in the atmosphere which contain chlorine or bromine, the primary precursors of ozone depletion when these molecules reach the stratosphere.

In this presentation, the status of the science will be reviewed, focusing on the Intergovernmental Panel on Climate Change (IPCC) 2001 Report, followed by a summary of the relevant measurements conducted by the U.S.'s primary laboratory for monitoring those elements that affect climate and the ozone layer.

Unbottleable Molecules Generated by Collision Induced Electron Transfer in the Gas Phase: An Intersection of Experiment and Theory

Helmut Schwarz

Institut für Chemie, Technische Universität Berlin, D-10623 Berlin,
FAX: ++49 30 314 21102; e-mail: Helmut.Schwarz@www.chem.tu-berlin.de

Over the last decade, neutralization-reionization mass spectrometry (NRMS)[1] has emerged as a powerful method for the generation and structural characterization of small, neutral molecules, which are believed to play a central role in many fields of chemistry, but are usually not accessible in the condensed phase. Systems that will be discussed in detail include the celebrated water oxide and ethylenedione molecules.

Further, experimental and computational studies of small, multiply charged cations (e. g. Olah´s "superelectrophiles")[2] will be presented with emphasis on the generation of *thermochemically stable*, doubly- and triply-charged diatomic molecules by charge stripping (CS) mass spectrometry.[3] This area is of topical interest in chemistry and physics, and examples will be discussed for diatomic cations with *positive* proton affinities or of diatomic trications that are thermochemically stable towards Coulomb explosion.

References

---

[1] Schalley, C. H.; Hornung, G.; Schröder, D.; Schwarz, H. *Chem. Soc. Rev.* **1998**, *27*, 91.
[2] Olah, G. A. *Angew. Chem.* **1993**, *105*, 805.
[3] Schröder, D.; Schwarz, H. *J. Phys. Chem. A* **2000**, *104*, 11257.

A New Surface-Induced Dissociation FTMS Instrument and First Results

Jean Futrell, Julia Laskin, Eduard Denisov, Steven Barlow, Mark Tinkle and Anil Shukla

Pacific Northwest National Laboratory (PNNL), WR Wiley Environmental Molecular Sciences Laboratory (EMSL), PO Box 999, Richland WA 99352 USA

A new FTMS research apparatus and first results are described. Reactant ions are prepared by MALDI or Electrospray ion generation, an ion funnel for efficient ion injection, a triple quadrupole mass selector and ion collisional cooling section and an energy selector preceding ion buncher and injector lenses. A high vacuum probe lock presents an orthogonally mounted surface to the ion beam inside the solenoid field. Reflected primary ions and secondary ions are trapped in a forth-order field-corrected Penning Trap and measured by conventional FT methods. This apparatus is our newest tool for investigating mechanisms of collisional activation and dissociation of ions. In this work we compare spectra obtained with carefully controlled multiple collision SORI excitation and single collisional excitation with a perfluoroalkyl self-assembled monolayer (FSAM). Using protonated model peptides and RRKM modeling of their dissociation we deduce accurate dissociation parameters and energy transfer functions for their collisional activation. Similarities and differences in results obtained in SORI and FSAM collisional activation are rationalized in the context of recent collisional dynamics and kinetics results.

Recombination of H_3^+ and D_3^+ ions with electrons in low temperature plasma

J. Glosík, R. Plašil, A. Pysanenko, V. Poterya, P. Kudrna, P. Zakouřil

Charles University Prague, Mathematics and Physics Faculty, Prague, Czech Republic

ABSTRACT

From the decaying plasma (stationary afterglow) in the mixture of He, Ar and H_2 (or D_2) we determined the overall recombination rate constant (α_{eff}) of the recombination of H_3^+ and D_3^+ ions with electrons at thermal energies. We observed dependence of recombination rate coefficients on partial pressure of hydrogen (and deuterium), which indicates that observed recombination is the three-body process proceeding most probably via formation of long lived intermediate state. From the obtained data we concluded that binary dissociative recombination of H_3^+ and D_3^+ ions with electrons is very slow with rate coefficient $\alpha_{DR} < 3\times10^{-9}$ cm^3 s^{-1} and $\alpha_{DR} < 6\times10^{-9}$ cm^3 s^{-1}, respectively.

1. Introduction

Experimental and theoretical studies of dissociative recombination (DR) of H_3^+ and D_3^+ ions have been pursued for many years. The reason is in importance of H_3^+ in astrophysics [1-7] and it is one of the few polyatomic ions that can be treated theoretically. Calculations of the molecular states of both ions clearly indicate that the curve-crossing mechanism cannot be operative. The early microwave-afterglow experiments [8] showed that H_3^+ recombines with "normal" recombination rate coefficients $\alpha \approx 1\text{-}3\times10^{-7}$ cm^{3}s^{-1}. Persson and Brown in 1955 carried out measurements [9] in high purity stationary afterglow and they obtained very low value of the recombination coefficient $\alpha = 3\times10^{-8}$ cm^{3}s^{-1}. Later in seventies several afterglow and beam experiments were carried out that yielded the recombination rate coefficient for this reaction of the order $2\div3\times10^{-7}$ cm^{3}s^{-1} at 300 K. However, in 1984 Adams *et al.* [10] obtained in FALP apparatus the recombination rate for this reaction $\alpha \approx 2\times10^{-8}$ cm^{3}s^{-1}. Amano in 1990 [11], using an infrared spectroscopic absorption technique in stationary afterglow, obtained $\alpha = 1.8\times10^{-7}$ cm^{3}s^{-1} at 273 K. Important was that Amano specified the vibrational state of recombining ions, namely as ground state ions, $H_3^+(v=0)$. In order to solve this discrepancy, new FALP apparatus was built at University of Rennes in France (FALP-MS) [12], they obtained $\alpha = 1.5\times10^{-7}$ cm^{3}s^{-1} for H_3^+ with a low degree of vibrational excitation $v<2$ and $\alpha = 1.1\times10^{-7}$ cm^{3}s^{-1} for ground state ions $H_3^+(v=0)$ at 650 K. In 1993 Smith and Španěl using the FALP system found the value $\alpha = (1\div2)\times10^{-8}$ cm^{3}s^{-1} for $H_3^+(v=0)$ at 300 K [13,14]. In 1995 Gougousi *et al.* [15] made a new FALP study of the recombination of H_3^+ ion. They suggested that the H_3^+ recombination might proceed via three-body process that involves the formation of autoionising Rydberg states. The values of rate coefficients obtained in several beam experiments are also dispersed over one order of magnitude. Theoretical studies give values of rate coefficients below 10^{-8} cm^{3}s^{-1}.

2. Experiment and data analyses

In our studies of recombination of H_3^+ and D_3^+ ions with electrons we used the apparatus of stationary afterglow type - Advanced Integrated Stationary Afterglow (**AISA).** The main part of AISA is a large cylindrical stainless-steel UHV discharge chamber [16-18] (40 cm long with diameter 40 cm) cooled to below -40ºC during the measurements (see Figure 1). Purified He was used as a buffer gas (impurity level < 0.1 ppm). The plasma was periodically generated by pulses of microwave power (~ 1 kW, 0.2-2 ms pulses and repetition period 40-100 ms). The H_3^+ and D_3^+ ions are produced in the sequence of ion molecule reactions, which are following formation of parent ions during the period of active discharge. We are using "suitable" mixtures of He-Ar-H_2 and He-Ar-D_2 to optimise this formation. In this mixture there is majority of He (~99%), admixture of Ar (up to 1%) and carefully controlled small number densities of H_2 or D_2.

The electron number density (n_e) was determined from Langmuir probe measurements (18 μm in diameter and 7 mm in length). For experimental details see e.g. Refs. [13-17]. The plasma composition was monitored by a mass spectrometer working in "integral" and "time resolved" regime.

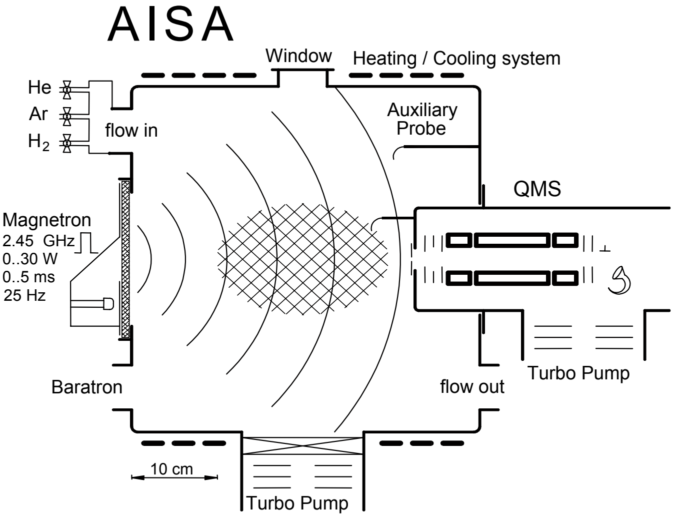

Figure 1. Schematic view of the Advanced Integrated Stationary Afterglow - AISA.

In the Figure 2 are plotted examples of the integral spectra obtained by sampling ions over several cycles in mixture of He-Ar, He-Ar-H_2 and He-Ar-D_2 respectively. These spectra are giving information about ions present in the plasma. Note that Ar^+, ArH^+/ArD^+ and H_3^+/D_3^+ ions are major components of the spectra. In some spectra also traces of H_3O^+ and eventually also N_2H^+ and ArH_3^+ (or corresponding deuterated species) were observed. We realize the complication of the relation between the obtained spectrum and real ionic composition in the centre of the discharge vessel.

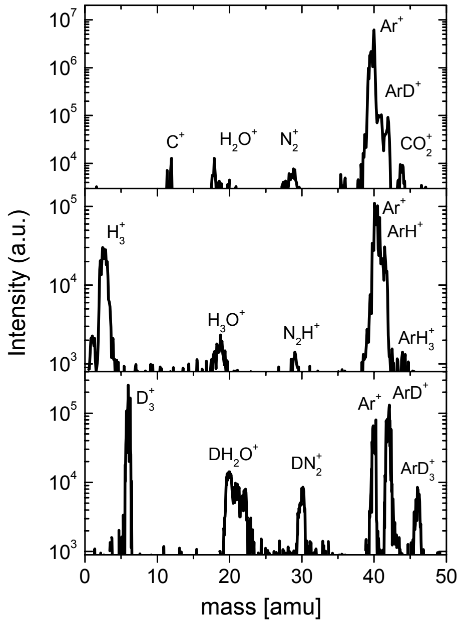

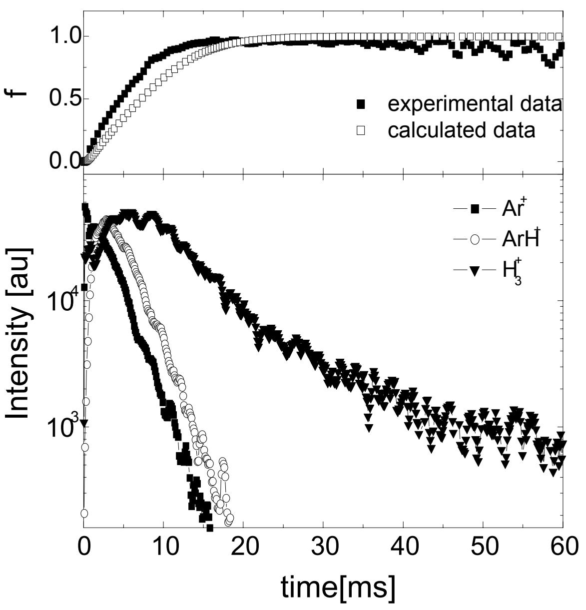

Figure 2. Integral mass spectra obtained in He-Ar, He - Ar - H_2 and He - Ar - D_2 mixture, respectively.

Figure 3*.* The time resolved mass spectra obtained for $[H_2] = 2.65\times10^{11}$ cm^{-3} , *f* is the relative population of H_3^+.

In Figure 3 are plotted time resolved spectra and fraction *f* corresponding to relative ionic population of H_3^+ as obtain from the measurements and from the calculation.

Because of quasi-neutrality of the plasma RHS of the balance equation describing decay of the plasma can be written as a sum of terms corresponding to recombination of H_3^+ ions, recombination of "impurity ions" and common ambipolar diffusion term:

$$\frac{dn_e}{dt} = -\alpha\left[H_3^+\right]n_e - \nu_D n_e - \nu_R n_e \tag{1}$$

Here the recombination of electrons with H_3^+ is accounted for by first term on RHS - $\alpha[H_3^+]\,n_e$. Last term on the RHS is the loss term for the electrons due to the formation of "impurity ions" and their fast recombination. If we assume that in decaying plasma there is fraction $f = f(t) = [H_3^+]/n_e$ of recombining H_3^+ ions (for experiment with D_3^+ is situation similar) the balance equation can be rewritten to the form (using n_e' for dn_e/dt):

$$-\frac{n_e'}{n_e^2} = \alpha_{eff} + \frac{(\nu_D + \nu_R)}{n_e} \tag{2}$$

Introduced $\alpha_{eff}(t) = \alpha f(t)$ represents the effective rate coefficient of the processes in which loss of charged particles is proportional to the n_e^2. If $\alpha_{eff}(t)$ can be considered as a constant, the plot of $-n_e'/n_e^2$ versus $1/n_e$ should be linear with slope given by $(\nu_D + \nu_R)$.

3. Results and discussion

In a He-Ar-H_2 (or D_2) mixture we measured the "de-ionisation rate", α_{eff}, in the plasma containing H_3^+ (or D_3^+) ions. The examples of measured values of $n_e(t)$ obtained in He-Ar-D_2 mixture are plotted in the upper panel of Figure 4; a dependence of the decay of the plasma on [D_2] is evident. In the lower panel of Figure 4 reciprocal values $1/n_e(t)$ are plotted, these plots are used in standard analyses for calculation of α_{eff}. The example of "advance analyse" plots, $(-n_e'/n_e^2 - \nu_D/n_e)$ versus $1/n_e$, are given in Figure 5.

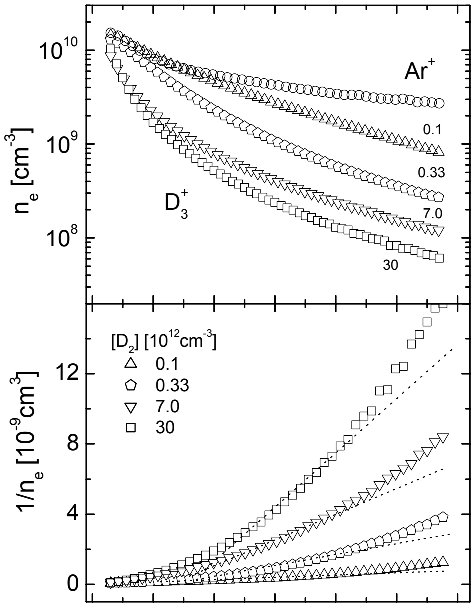

Figure 4. Upper panel: The measured time evolutions of the electron number density, $n_e(t)$, in D_3^+ dominated afterglow. Ar$^+$ indicate the decay curve corresponding to plasma dominated by Ar$^+$ ions. Lower panel: The corresponding values of $1/n_e(t)$.

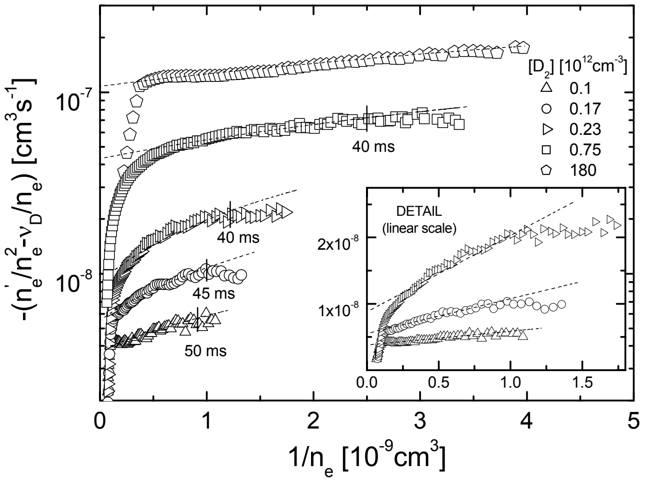

Figure 5. Advanced analysis. Dependence of the decay of D_3^+ dominated afterglow on concentration of D_2. Note that detail in the insert is plotted in linear scale.

We observe that the rate coefficients of recombination of H_3^+ and D_3^+ ions with electrons are dependent on $[H_2]$ and $[D_2]$, respectively. Obtained α_{eff} for the recombination of H_3^+ and D_3^+ are plotted in left and right panel of Figure 6, respectively. Since only three-body recombination have been observed we concluded that the binary channels (dissociative recombination) are negligible. From our study follows that for astronomy fundamental binary dissociative recombination of H_3^+ ions with electrons is very slow process (at ~ 270 K) - with rate coefficient $\alpha_{DR} < 3\times10^{-9}$ cm^3 s^{-1}. For the rate coefficient of dissociative recombination of D_3^+ ions with electrons (at ~ 230 K) we obtained limit $\alpha_{DR} < 6\times10^{-9}$ cm^3 s^{-1}. The results are in accordance with theoretical predictions for the dissociative recombination (see refs. [19,20] and references there in). For detailed discussion see also our previous papers [16,17,18].

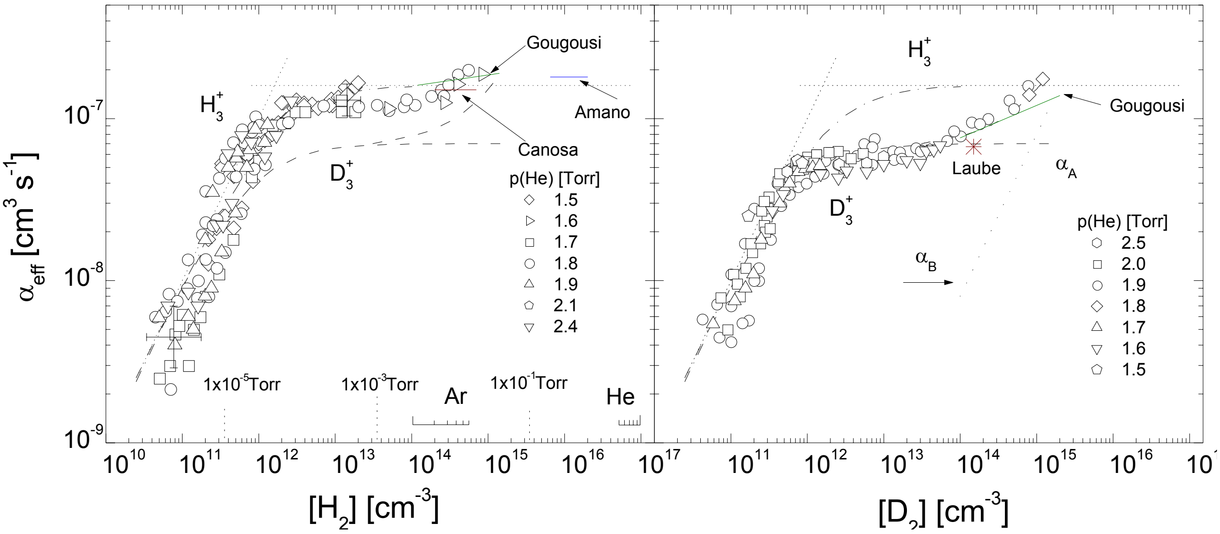

Figure 6. Left panel: Dependence of observed $\alpha_{eff}(H_3^+)$ on $[H_2]$. Right panel: Dependence of observed $\alpha_{eff}(D_3^+)$ on $[D_2]$. Included are also previous results of Laube *et al.* [21], Gougousi *et al.*[15], Canosa *et al.*[12] and Amano[11].

Acknowledgements:

Thanks for financial support are due to GACR (202/00/1689, 202/99/D061, 205/02/0610, 202/02/0948), GAUK (146/2000 B FYZ MFF) and MSM 1132000002. The experiments were carried out with support of EU in frame of the ETR network (HPRN-CT-2000-00142) and with support from EURATOM.

References

---

[1] R. Geballe, K.H. Hinkle, T. Oka, *Science* **279** (1998) 1910
[2] A. Dalgarno, *Adv. At. Mol. Opt. Phys. B* **32** (1994) 57
[3] D. Uy, M. Cordonnier, T. Oka, *Phys. Rev. Lett.* **78** (1997) 3844
[4] T.R. Geballe, T. Oka, *Nature* **384** (1996) 334
[5] E. Herbst, *Philosophical Transactions: Math., Phys., and Eng. Science* **358** (2000) 2523
[6] T.R. Geballe, M.F. Jagod, T. Oka, *Astrophysical Journal* **408** (1993) L109
[7] J.E.P. Connerney, T. Satoh, *Phis. Trans. R. Soc. Lond. A* **358** (2000) 2471
[8] M.A. Biondi and S.C. Brown, *Phys. Rev.* **76** (1949) 1697; J.M. Richardson and R.B. Holt, *Phys. Rev.* **81** (1951) 153; L.J. Varnerin, Jr., *Phys. Rev.* **84** (1951) 563
[9] K.B. Persson and S.C. Brown, *Phys. Rev.* **100** (1955) 729
[10] N.G. Adams, D. Smith, and E. Alge, *J. Chem. Phys.* **81** (1984) 1778
[11] T. Amano, *J. Chem. Phys.* **92** (1990) 6492
[12] A. Canosa, B.R. Rowe, J.B.A. Mitchell, J.C. Gomet, and C. Rebrion, *Astron. Astrophys.* **248** (1991) L19
[13] D. Smith and P. Španěl, *International J. of Mass Spectr. and Ion Processes* **129** (1993) 163
[14] D. Smith and P. Španěl, *Chem. Phys. Letters* **211** (1993) 454
[15] T. Gougousi, R. Johnsen, M.F. Golde, *Int. J. Mass Spectr. Ion Processes* **149/150** (1995) 131

[16] J. Glosik, R. Plasil, V. Poterya, P. Kudrna, M. Tichy, *Chem. Phys. Lett.* **331** (2000) 209

[17] J. Glosik, R. Plasil, V. Poterya, P. Kudrna, M. Tichy, A. Pysanenko, *J. Phys. B-At. Mol. Opt.* **34** (2001) L485

[18] V. Poterya, J. Glosík, R. Plašil, M. Tichý, P. Kudrna, A. Pysanenko, *Phys. Rev. Letter*, 2001 in print

[19] V. Kokoouline, C.H. Greene, B.D. Esry, *Nature* **412** (2001) 891-894

[20] A Suzor-Weiner, I.F. Schneider, *Nature* **412** (2001) 871-872

[21] S. Laube, A. Le Padelleck, O. Sidko, C. Rebrion-Rowe, J.B.A. Mitchell and B.R. Rowe, *J. Phys. B-At. Mol. Opt.* **31** (1998) 2111

ICP/SIFT Studies of Atomic-Metal Ion Reactions

Gregory K. Koyanagi and Diethard K. Bohme

Department of Chemistry, Centre for Research in Mass Spectrometry and Centre for Research in Earth and Space Science, York University, Toronto, Ontario, Canada, M3J 1P3.

An inductively-coupled plasma (ICP) ion source recently has been combined with an existing Selected-Ion Flow Tube (SIFT) mass spectrometer in the Ion-Chemistry Laboratory at York University.[1] This novel ICP/SIFT apparatus provides a powerful and versatile instrument for measuring the kinetics and product distribution of atomic-metal ion-molecule reactions in the gas phase. We are currently engrossed in three different kinds of investigations with this instrument.

1. We are surveying periodicities in the intrinsic reactivities of atomic metal ions across and down the periodic table.
2. We are surveying ligated metal-ion chemistry.
3. We are exploring reactions of bio-metallic ions with biologically important gases.

Experimental Apparatus

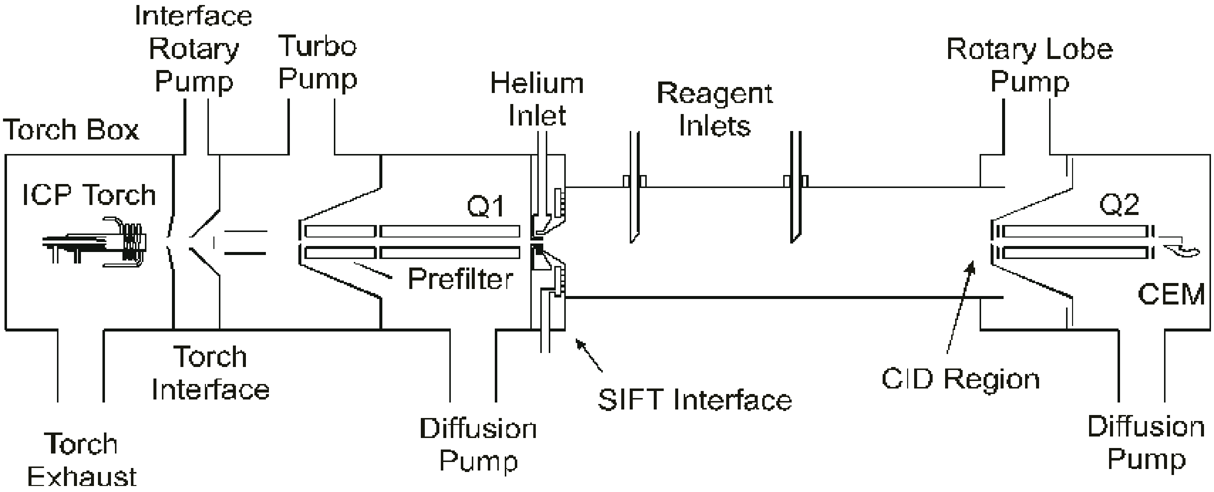

Figure 1. Schematic view of the ICP/SIFT apparatus.

The ICP/SIFT apparatus is shown in Figure 1. ICP ions of interest that traverse the differentially-pumped ICP/SIFT interface are selected from the beam with a quadrupole mass filter and then injected into flowing helium gas at 0.35 Torr. The reacting mixture is analyzed downstream with a second quadrupole mass filter as a function of the neutral reagent added midstream. The internal energy of the metal ions entering the reaction region is determined by the initial internal-energy distribution of the ICP ions at 5500 K and the extent to which this distribution is modified by radiative and collisional electronic-state relaxation. The latter may occur with argon as the extracted plasma cools upon sampling and then by collisions with He atoms in the flow tube. (ca. 4×10^5 collisions) prior to the reaction region, but the actual extent of electronic relaxation (either radiative or collisional) is not known. The collisions with He ensure that the ions reach a translational temperature equal to the tube temperature of 295 ± 2 K prior to entering the reaction region.

Results and Discussion

1. Intrinsic reactivities of bare metal ions: We are surveying periodicities in the intrinsic reactivities of bare metal ions towards small and large molecules. So far the emphasis has been on transition-metal ions and lanthanide cations reacting with O_2, N_2O, COS, NH_3, CH_4 and the aromatic molecules benzene, hexafluorobenzene, pyridine and cyclopentadiene. Our aim is to uncover fundamental parameters such as electronic structure, spin and thermodynamics that determine the reactivities of atomic ions.[2] In the process we also have the opportunity to explore the higher-order chemistry initiated by atomic metal ions. Figure 2 provides data obtained for the chemistry initiated by Nb^+ in N_2O.

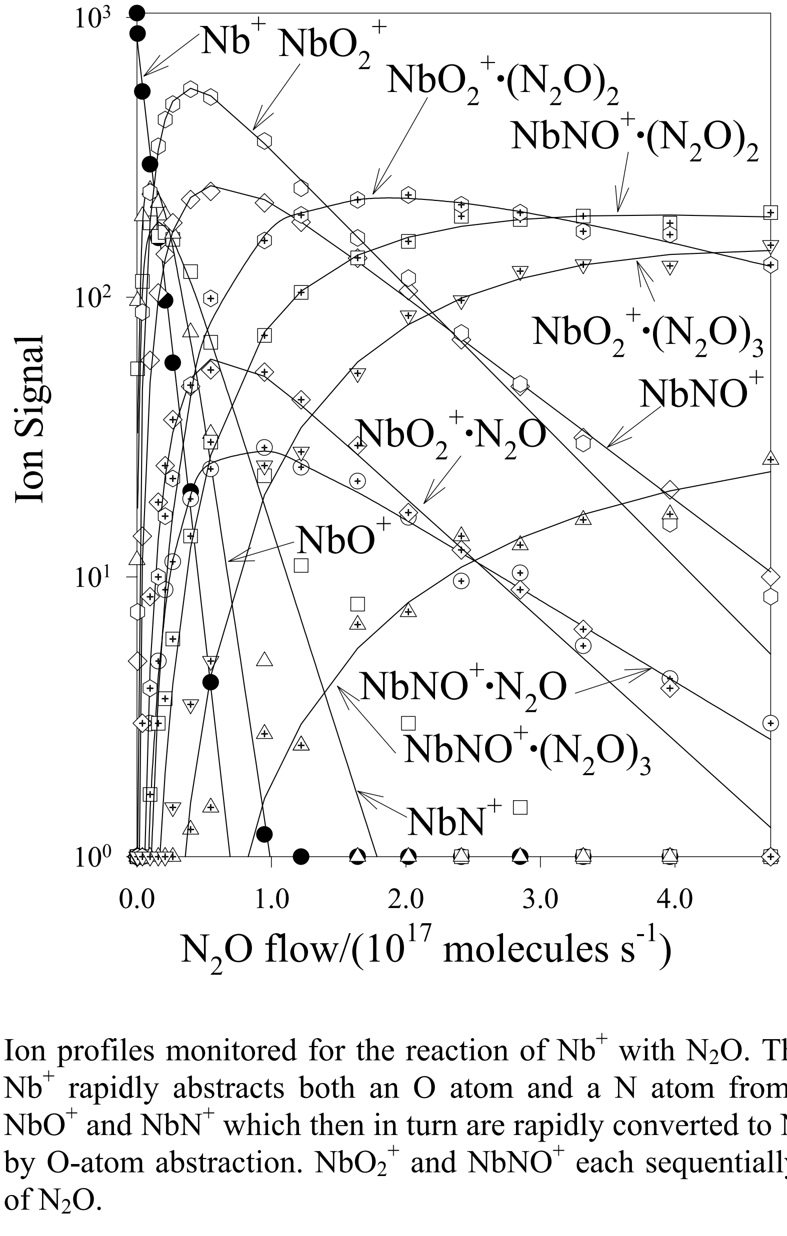

Figure 2. Ion profiles monitored for the reaction of Nb^+ with N_2O. The data shows that Nb^+ rapidly abstracts both an O atom and a N atom from N_2O to establish NbO^+ and NbN^+ which then in turn are rapidly converted to NbO_2^+ and $NbNO^+$ by O-atom abstraction. NbO_2^+ and $NbNO^+$ each sequentially add 3 molecules of N_2O.

Our measurements of atomic-ion reactivities also are directed toward the development of a data base for chemical resolution using ICP/MS and toward the elucidation of specific isobaric interferences.[3]

2. Ligated metal-ion chemistry: Addition of a ligand molecule upstream of the flow tube allows metal ions to be ligated upstream and to be reacted downstream. Our focus so far has been on the use of benzene and large carbonaceous molecules such as coronene, corannulene and C_{60} as ligands. We have completed a survey of reactivities of $M^+(C_6H_6)$ ions towards O_2 across and down the periodic table and in so doing we have identified benzene oxidation mediated and catalyzed by specific metal ions. The large PAHs and C_{60} are large enough to present a carbonaceous "surface" to the metal ion. In this case a comparison of reactivities of bare metal ions and ligated metal ions can provide a measure of carbonaceous "surface" effects. Reactivity studies of these adduct ions can provide insight into the nature of the coordination of the metal ion on the carbonaceous surface. We have completed such studies for Fe^+(benzene), Fe^+(coronene), Fe^+(corannulene) and $Fe^+(C_{60})$.[4]

3. Bio-metallic ion Chemistry: The objective in these studies is to mimic the local metal-atom bond found in a biomolecule and measure their intrinsic reactivities towards biologically important gases such as O_2, CO, CO_2, NO, H_2O and NH_3. Example of such M^+(biomolecule) bonds include the Cu-imidazole bond found in blue copper proteins and the metal-pyrrole bonds found in porphorins and proteins. Biomolecular units that we have employed in these mimicking studies include glycine, methyl-imidazole, pyrrole, benzene and pyridine. Biologically important metals include Cu, Fe, Ag, Zn, and Pt.

The M^+(biomolecule) ions are again created upstream in the flow tube of the ICP/SIFT and then reacted downstream. We have now investigated the reactions of Cu^+(1-methyl imidazole)$_n$ ions (for n = 1-3) with O_2, CO, CO_2, D_2O, ND_3 and N_2O and the reactions of Ni^+(pyrrole) and Cu^+(pyrrole) with O_2, CO and CO_2. Interesting trends in reactivity were observed and, together with parallel theoretical studies, insight was gathered into the structures of some of these M^+(biomolecule) ions. These are early investigations of such biological chemistry but they clearly point toward a very promising future.

Acknowledgements:

Continued financial support from the Natural Sciences and Engineering Research Council of Canada is greatly appreciated. Also, we acknowledge support from the National Research Council, the Natural Science and Engineering Research Council and MDS SCIEX in the form of a Research Partnership grant.

References:

[1] Koyanagi, G.K.; Lavrov, V.V.; Baranov, V.I.; Bandura, D.; Tanner, S.D.; McLaren, J.W.; Bohme, D.K. *Int. J. Mass Spectrom.* **2000**, *194*, L1.
[2] Koyanagi, G.K.; Bohme, D.K. *J.Phys. Chem. A* **2001**, *105*, 8964.
[3] Koyanagi, G.K.; Baranov, V.I.; Tanner, S.D.; Bohme, D.K. *J. Anal. At. Spectrom.* **2000**, *15*, 1207.
[4] Caraiman, D.; Koyanagi, G.K.; Scott, L.T.; Preda, D.V.; Bohme, D.K. *J. Am. Chem. Soc.* **2001**, *123*, 8573-8582

Some Aspects of Ion-Molecule Reaction Mechanisms

Eldon Ferguson

NOAA/CMDL Boulder, Colorado

The Flowing Afterglow technique developed in Boulder in 1964 was applied to the understanding of the ion reactions in the earth's ionosphere. This has subsequently been extended by others and applied to other fields of physics and chemistry. The purpose here is to recount a somewhat neglected aspect of the FA studies, namely their contribution to the understanding of reaction mechanisms. The neglect in reporting these results to the physical chemistry community arose in large part because most of the early results were reported in the geophysical literature where the impact was immediate.

The versatility of the FA led to a huge increase in the number and variety of known reaction rate constants, which led to the discovery of several generalities about reactions. This in turn led to new insights into mechanistic processes.

The generality of fast ion charge-transfer with neutrals that was found overturned theoretical prediction of generally slow CT that had been developed for ionospheric application in the absence of laboratory measurements. The theory invoked, the Adiabatic Principle, is not valid when long-lived complexes are formed as is usually the case for IM reactions at thermal energy. In cases where repulsive chemical interactions dominate the attractive electrostatic potential so that long-lived complexes are not formed, the Adiabatic Principle is valid and has been used to explain some of the observed exceptions to fast reactions. The experimental techniques for the measurement of thermal energy IM reactions prior to the FA involved the ionization of gas mixtures and so were unsuited for the study of CT.

The failure of the Adiabatic Principle was recognized when the FA was first turned on. He buffer gas was ionized and the mass spectrometer detected both O^+ and N^+ ions resulting from He^+ CT with air from a small leak, showing the CT with N_2 to be slightly faster than CT with O_2 , both occurring on essentially every collision. Two years earlier a theory for He escape from the earth's atmosphere by reaction of He^+ with O_2 had been proposed which required non-reaction with N_2 This was assumed to be probable on the basis of the Adiabatic Principle. We were thus able to disprove this He loss theory. Similarly the reaction $N_2^+ + O \rightarrow NO^+ + N$ had been excluded from ionospheric models because it is non-adiabatic, i.e. involves an electronic state change. It turns out, however, that the reaction is efficient and represents the major N_2^+ loss in the earth's ionosphere. The FA versatility allowed the study of reactions with unstable neutrals such as O, N, H atoms.

Another generality (or propensity) found was that exothermic associative-detachment of negative ions by neutrals is usually efficient. Again this requires either complex formation or at least an attractive potential curve. The slow reaction exceptions observed have been explained from this viewpoint. The FA yielded the first measurements of AD. The reaction $H^- + H \rightarrow H_2 + e$, of considerable astrophysical importance, has a rate constant equal to half the Langevin collision rate constant, consistent with one of the two $H^- + H$ entrance channel potential surfaces being attractive into the autodetaching region while the other is repulsive. On the other hand the exothermic $O^- + N_2 \rightarrow N_2O + e$ AD was found to be slow and it was shown that the adiabatic potential surface is repulsive.

The reaction $O^- + H_2 \rightarrow H_2O + e$ is fast due to H atom abstraction forming a complex in which AD occurs, $O^- + H_2 \rightarrow (OH^- \cdots H)^* \rightarrow H_2O + e$. The AD $OH^- + H$ was independently found to be efficient. At elevated KE the complex lifetime becomes too short to allow AD, and the reaction becomes $O^- + H_2 \rightarrow OH^- + H$. The exothermic AD's $C^- + H_2 \rightarrow CH_2 + e$ and $S^- + H_2 \rightarrow H_2S + e$ do not occur because the initial H atom abstractions are endothermic precluding complex formation.

Another generality, for which we have found no exceptions so far, is fast exothermic proton transfer (for small molecular systems). A reaction first thought to be an exception, measured in Christchurch, was proton transfer from HCN^+ to CO_2 . The reaction was finally determined to be $HCN^+ + CO_2 \rightarrow HNC^+ + CO_2$, two sequential fast proton transfers in a complex, i.e. $HCN^+ + CO_2 \rightarrow (CN \cdots HCO_2^+) \rightarrow HNC^+ + CO_2$, the catalytic isomerization of HCN^+ to HNC^+ . Energy dependence studies in Innsbruck proved this mechanism. At higher reactant kinetic energies long lived complexes are not formed and only the initial proton transfer occurs. The Innsbruck studies fortuitiously yielded the first accurate determinations of the heats of formation of HNC and HNC^+ as an unexpected fall-out.

Another generality was the finding of efficient vibrational quenching of diatomic ions by neutrals. This is in marked contrast to the very inefficient vibrational quenching of non-polar neutral diatomics at thermal energy. The first systematic studies of ion vibrational quenching were carried out in Boulder, O_2^+ (v), and Innsbruck, NO^+(v). The difference between ions and neutrals is the generality for long-lived complexes with ions to be formed due to the long range ion-induced dipole forces yielding an attractive well. The several slow exceptions found could be explained by chemical inhibition of complex formation. Our complex quenching model, in combination with complex lifetime measurements (by 3-body association), allowed a determination of the vibrational predissociation rate constant in weak complexes, $\sim 10^9 - 10^{10}$ s^{-1} in several cases. Our quenching model showed a correlation of quenching rate constant with well depth. One application was the deduction of an anomalously strong bond for $CO^+ \cdot N_2$, relative to the expected electrostatic bond strength, based on the observation of very fast quenching of CO^+(v) by N_2 reported by Bierbaum and Leone. This has subsequently been supported by an experimental bond strength determination by Glosik et. al in Innsbruck and by ab initio quantal calculations by Rosmus et. al in 1999. In retrospect the reason for the enhanced attractive force is due to charge-transfer complex formation (which should have been obvious to us years ago!).

Several observed anomalously large three-body association rate constants, led us to develop an "endothermic trapping" model explaining enhanced complex lifetimes, analogous to Feshbach resonances in atomic scattering. Three-body association rate constants involve the collisional stabilization of complexes and hence are proportional to the complex lifetime. A particular example is the three-body association, $Si^+ + O_2 + M \rightarrow SiO_2^+ + M$, of interest in connection with the loss of meteor derived Si^+ in the earth's atmosphere. The three-body rate constant is an order of magnitude larger than that for many similar ions with O_2 , e.g. Mg^+, Ca^+ , Fe^+ , Na^+ and K^+. The trapping mechanism proposed to enhance the complex lifetime is $Si^+ + O_2 \int (SiO^+ \cdots O)^*$. The reaction $Si^+ + O_2 \rightarrow SiO^+ + O$ is slightly endothermic but can be driven by the electrostatic attractive force. Further pursuit of the endothermic $Si^+ + O_2 \rightarrow SiO^+ + O$ reaction as a function of KE in a Flow Drift Tube allowed determination of the endothermicity which yielded an 0.2 eV correction to the literature value of $D(SiO^+)$.

When long-lived complexes are not formed, the Adiabatic Principle does apply and was used long ago by Landau and Teller to derive a theory for the energy dependence of neutral molecule collisional vibrational quenching. The first (and only so far) applications of Landau-Teller theory to ion vibrational quenching have been carried out in Innsbruck. This required having conditions where repulsive interaction dominated attractive interaction so that long-lived complexes were not formed, e.g. using He quencher and elevated KE in a Flow Drift Tube.

What is learned in the case of diatomic ion vibrational quenching is the repulsive exponential parameter, usually given in the form of range parameter, e.g. 0.2Å for $N_2^+(v)$ + He. In the case of He one triatomic ion that has been studied, in Innsbruck, $HCN^+(v)$ + He we were able to determine (a) that HCN^+ is vibrationally enhanced selectively in the CH stretch mode by 30-50 eV electron ionization. This despite the ionized electron being removed from the CN triple bond, whose vibrational frequency is most changed upon ionization, and (b) the vibrational quenching is directly to the ground state (or possibly the low frequency bend mode) rather than cascading via the intermediate frequency CN stretch. Also of course the repulsive potential range parameter. The range parameter, 0.21 Å is about the same as for the isoelectronic N_2^+ , indeed all diatomic repulsive range parameters, both for neutrals and ions seem to be about 0.2 Å. The isotopic $DCN^+(v)$ quenching was also measured.

---

*It is appropriate to dedicate this paper to the memory of Werner Lindinger, a valued friend and colleague for 27 years who collaborated in much of the work described here

Application of Ion Chemistry to Tropospheric VOC measurements*)

Armin Hansel, **Armin Wisthaler, Martin Graus, Wolfgang Grabmer**

Institut für Ionenphysik, Universität Innsbruck, Austria, armin.hansel@uibk.ac.at

Abstract

In Werner Lindingers laboratory we have developed a mass spectrometric technique, named Proton-Transfer-Reaction Mass-Spectrometry (PTR-MS), which utilizes positive ion chemistry to measure trace neutral concentrations in air. During the last few years PTR-MS has been used in food research, in medical applications, and in environmental applications to gain gas phase information of volatile organic compounds (VOCs) at parts per trillion (pptv) levels. The real-time method relies on proton transfer reactions between H_3O^+ primary ions and organic trace gases (VOCs) which have a higher proton affinity than water molecules. Organic trace gases such as hydrocarbons, carbonyls, alcohols, acetonitrile, and others can be monitored on-line. In this paper we will discuss the mass spectrometric method and present recent results on tropospheric VOC measurements.

Introduction

The main interest in tropospheric VOCs originating from biogenic sources such as forests and from anthropogenic sources such as cities is that these reactive trace gases can have a significant impact on levels of oxidants such as ozone (O_3) and the hydroxyl radical (OH), and on secondary organic aerosol formation [1]. In addition, oxygenated VOCs like acetone are an important source of HO_x (=OH + HO_2) radicals in the upper troposphere [2]. Atmospheric degradation of acetone and acetaldehyde produce acetylperoxy radicals. These radicals associate with NO_2 to form peroxyacetic nitric anhydride (PAN; $CH_3C(O)OONO_2$) which acts as a relatively unreactive temporary reservoir for nitrogen oxides (NO_x = NO + NO_2). It is in this form that NO_x equivalents are transported over wide distances, e.g. from urban to rural areas, where they can contribute to photochemical ozone formation with biogenic VOCs.

Photochemical reactions of VOCs in the troposphere are complex, depending on the presence of OH, NO_x and ultraviolet light. The generally accepted net reaction of a simple hydrocarbon (HC) is the following [1]:

$$HC + 4\,O_2 + 2\,h\nu \rightarrow 2\,O_3 + \text{carbonyl(s)} + 2\,H_2O \qquad (1)$$

OH and NO_x do not appear in the net reaction as they are regenerated in other reactions. Notably, atmospheric oxidation of HC (at sufficient NO_x) results in the production of ozone and carbonyl compounds that can undergo further photochemistry. A VOC generally contributes more to ozone formation the higher its density is and the faster its reaction with OH radicals proceeds. Thus, in order to understand quantitatively tropospheric ozone chemistry, it is a necessary prerequisite to know the VOC distribution within the troposphere as well as VOC fluxes from individual sources. The examples below illustrate how the use of the PTR-MS technology [3] has enhanced our understanding of anthropogenic VOC emissions, biosphere-atmosphere exchange processes, and photochemical processing of both anthropogenic and biogenic VOCs in the troposphere.

---

*) This lecture is dedicated to the memory of our teacher, colleague and friend Prof. Werner Lindinger, who passed away in February 2001.

Tropical Troposphere

Tropical regions with reactive hydrocarbon emissions from forests of greater than 10^{15} g C per year are especially important in determining the oxidizing capacity of the atmosphere because of the high abundance of UV radiation and high relative humidity. An other important aspect of tropospheric chemistry is the influence of anthropogenic activities. The rapid growth of human population and industrial development in China and South East Asia will increase air pollution in these tropical regions. An increase in carbonyl compounds in the tropical boundary layer for example has the potential to influence the upper troposphere. Carbonyl compounds transported into the upper troposphere by convection may act as free radical precursor and directly influence the oxidizing capacity of the upper troposphere [2,4].

During the last few years PTR-MS [5] has been used in several field campaigns to gain gas phase information of VOCs at parts per trillion (pptv) levels. Organic trace gases such as hydrocarbons, carbonyls, alcohols, acetonitrile, and others have been recorded in two different tropical regions. In Amazonia (LBA-Claire 1999), a largely unpolluted region which is optimally located to study chemical processes induced by tropical forest emissions [6,7] and above the Indian Ocean. The Indian Ocean Experiment (INDOEX 1999) offered the opportunity to study the influence of anthropogenic pollution in the tropical troposphere. Asia is already a significant source of pollution. Carbon monoxide (CO) from Asia is estimated to be 50 % larger than the combined emissions from Europe and N-America. CO sources are different in Asia from those in Europe and N-America. In India and surrounding countries biofuel use and agricultural burning cause strong CO emissions. Acetonitrile (CH_3CN) is a unique gaseous tracer for biomass burning and can, in combination with other species like acetone, methanol, and CO provide strong indications about air pollution sources. Ship- and airborne PTR-MS measurements of organic trace gases in real time over a broad spatial extent of the Indian Ocean turned out to be of great importance to detect pollution outflow from India and helped to quantify the relative amount of CO originating from biomass burning [8,9,10].

Air Pollution in Cities

During the Southern Oxidants Study (SOS) 1999 campaign ambient air samples were analyzed at Cornelia Fort Airport, Nashville, TN. Even at a ground-based site a high time resolution in VOC measurements is useful to investigate the photochemistry of anthropogenic and biogenic emissions under the influence of varying meteorological conditions. Aromatic species such as benzene and toluene with long atmospheric lifetimes showed strong diurnal variations having enhanced concentrations during night time decreasing shortly after sunrise to rather low values during day time. This frequently found diurnal pattern was a result of strong boundary layer dynamics and local transportation related emission sources. As more reactive species are considered, such as isoprene, a biogenic hydrocarbon (BHC) and its oxidation products methyl vinyl ketone (MVK) and methacrolein (MACR), the isoprene photochemistry [11] appeared to be occasionally enhanced in NO_x rich plumes that were advected to the site over deciduous forested land leading to enhanced peroxymethacrylic nitric anhydride (MPAN) values. MPAN is formed almost entirely from the oxidation of isoprene in the presence of NO_x and is an excellent indicator of recent ozone production from BHC. In contrast peroxypropionic nitric anhydride (PPN) is thought to be a marker for anthropogenic hydrocarbon (AHC) driven photochemistry [12]. Measurements [13] of peroxyacetic nitric anhydride (PAN), a general product of hydrocarbon-NO_x photochemistry, MPAN and PPN were used to estimate the contribution of BHC and AHC to regional tropospheric ozone production, which is a serious air quality problem in the South East of the United States especially during summer time.

During the Texas Air Quality Study (TexAQS 2000) ambient air was analyzed on-board the National Center for Atmospheric Research (NCAR) Electra aircraft using the Innsbruck PTR-MS. Molecular-level information of VOCs such as acetaldehyde, isoprene, toluene, ketones and PAN were obtained at parts per trillion (pptv) levels with a time resolution of typically 30 seconds. This high time resolution was useful in characterizing individual contributions of distinct sources for ozone production in the greater Houston area. On several flights, wind direction and speed were such that these airborne VOC measurements allowed to differentiate among anthropogenic petrochemical, urban, and power plant plumes. In-situ acetaldehyde measurements, taken in aircraft transects of the Houston metropolitan area, confirm the importance of propene emissions from localized point sources to the photochemical processing of NO_x and the rapid formation of ozone and PAN within short distances from the co-located NO_x and propene emission sources. Biogenic isoprene emissions contribute also to ozone formation. Fast response measurements of this compound and its photooxidation products MVK & MACR and hydroxyacetone revealed that biogenic emission sources are primarily located north east of Houston and contribute to ozone formation in the metropolitan Houston area only under certain metrological conditions.

References

[1] Atkinson, R, 2000: Atmospheric chemistry of VOCs and NO_x .*Atmos. Environ.* **34**, 2063-2101.

[2] Singh, H. B., M. Kannakidou, P. J. Crutzen, & D. Jacob, 1995: High concentrations and photochemical fate of carbonyls and alcohols in the global troposphere. *Nature* **378**, 50-54.

[3] Hansel, A., A. Jordan, R. Holzinger, P. Prazeller W. Vogel, W. Lindinger, 1995: Proton transfer reaction mass spectrometry: on-line trace gas analysis at ppb level, *Int. J. of Mass Spectrom. and Ion Processes*, **149/150**, 609-619.

[4] Wennberg, P. O. et al. 1998: Hydrogen radicals, nitrogen radicals, and the production of ozone in the upper troposphere. *Science* **279**, 49-53.

[5] Lindinger, W., A. Hansel, and A. Jordan, 1998: Proton-transfer-reaction mass spectrometry (PTR-MS): on-line monitoring of volatile organic compounds at pptv levels. *Chem. Soc. Rev.* **27**, 347-354.

[6] Warneke, C., R. Holzinger, A. Hansel, A. Jordan, and W. Lindinger, U. Pöschl, J. Williams, P. Hoor, H. Fischer, and P.J. Crutzen, H. A. Scheeren, J. Lelieveld, 2001: Isoprene and its oxidation products methyl vinyl ketone, methacrolein, and isoprene related peroxides measured on-line over a tropical rain forest in Suriname in March 1998, *J. Atmos. Chem.* **38**, 167-185.

[7] Pöschl, U., J. Williams, P. Hoor, H. Fischer, P. J. Crutzen, C. Warneke, R. Holzinger, A. Hansel, A. Jordan, W. Lindinger, H. A. Scheeren, W. Peters, J. Lelieveld, 2001: High Acetone Concentrations throughout the 0-12 km Altitude Range over the Tropical Rainforest in Surinam, *J. Atmos. Chem*. **38**, 115-132.

[8] Lelieveld, J., et al., 2001: The Indian Ocean Experiment: Widspread Air Pollution from South and Southeast Asia, *Science*, **291**, 1031-1036.

[9] Sprung, D., C. Jost, T. Reiner, A. Hansel, and A. Wisthaler, 2001: Airborne measurements of acetone and acetonitrile in the tropical Indian Ocean boundary layer and free troposphere: Aircraft-based intercomparison of AP-CIMS and PTR-MS measurements, *J. Geophys. Res*. **106**, 28511-28528.

[10] Wisthaler, A., A. Hansel, R. R. Dickerson, and P. J. Crutzen, 2001: *Organic* trace gas measurements by PTR-MS during INDOEX 1999, *J. Geophys. Res.* in press.

[11] Stroud, C.A., J.M. Roberts, E.J. Williams, D. Heried, D.D. Parish, W. Angevine, and F.C. Fehsenfeld, A. Wisthaler and A. Hansel, M.Martinez-Harder, H. Harder and W.H. Brune, B. Alicke and J. Stutz, A.B. White, 2002: Nighttime Isoprene trends at an urban forested site during the 1999 Southern Oxidant Study, *J. Geophys. Res.* in press.

[12] Hansel, A., and A. Wisthaler, 2000: A Method for Real-Time Detection of PAN, PPN and MPAN in Ambient Air, *Geophys. Res. Lett.* **27**, 895-898.

[13] Roberts, J.M., et al., 1998, *J. Geophys. Res.*, **103**, 22,473-22,490.

Applications of PTR-MS in Food Flavour Research: Recent Progress and Prospects

Chahan Yeretzian[1], Alfons Jordan[2], Martin Graus[2], Philippe Pollien[1], Werner Lindinger[2]

[1] *Nestlé Research Center, 1000 Lausanne 26, Switzerland*
[2] *Institut für Ionenphysik, Leopold-Franzens-Universität, Technikerstr. 25, 6020 Innsbruck, Austria*

Food products all along the food chain, from raw materials to final products, continuously emit volatile organic compounds (VOC). While VOC's represent only an infinitely small mass-fraction of the food product, they can be probed non-invasively and are related to important properties of the product itself, such as flavour, age or shelf-life, geographic or genetic origin, history of processing, safety, packaging or presence of micro-organisms.

In view of the substantial information that can be gained from knowledge of the chemical composition of the headspace (HS), several analytical techniques were developed that sample and analyse the HS of foods. Up until recently, nearly all HS analysis was based on gas chromatography. Yet, in spite of the advances made over the last twenty years, headspace-GC was rather inadequate when it came to monitor, in real time, the temporal evolution of volatile profiles. GC-based analysis tends to look at the HS as a static phenomenon.

But why is it important to have the added time dimension? We would like to cite just three areas, which benefit from the added time-dimension: (i) Many food-processing steps involve fast transformations of food products. Real-time monitoring of their HS can help to better understand and control these processes. (ii) Flavour generation and flavour degradation are two central issues of food flavour chemistry. Both are intrinsically dynamic processes and hence require analytical techniques that can capture this time-dependence. (iii) When food is being consumed, the temporal evolution of a flavour profile in the mouth is believed to be a crucial attribute for the perceived quality of foods. In order to investigate and understand such dynamic processes, one need analytical techniques that are intrinsically dynamic and capable to capture the time-dependent character of flavour.

Over the last few years, several approaches have been evaluated and implemented which provide temporal information on volatile compositions. Following a brief overview of current on-line techniques for VOC analysis, we will discuss applications PTR-MS, and outline the impact of PTR-MS on food flavour research.

On-line food flavour analysis

To achieve the time-resolution needed for fast on-line measurements of VOCs, GC can be replaced by MS as a means to separate volatile compounds. Yet, prerequisite for separation in a mass filter is ionisation. This introduces complications due to potential ionisation induced fragmentation. It was, therefore, only when soft and sensitive ionisation techniques became available that direct injection into a mass spectrometer developed into a valuable approach for flavour analysis. Currently, two soft ionisation modes have been implemented in actual instruments - chemical ionisation (CI) and laser ionisation. Atmospheric-Pressure Chemical-Ionisation MS (APCI-MS) [1-4] and Proton-Transfer-Reaction MS (PTR-MS) [5,6] are both based on CI. APCI-MS utilises a conventional CI cell combined with a newly developed inlet system, while the strength of PTR-MS is its unique design of the chemical ionisation cell. Both approaches are unselective in their ionisation process, detecting essentially all VOCs in the HS. They are hence one-dimensional techniques and an unambiguous assignment of compounds requires additional sources of information. In contrast, resonance-enhanced multiphoton ionisation (REMPI) introduces selectivity in the ionisation step [7-9]. In combination with a time-of-flight mass filter, REMPI-TOFMS represents a two-dimensional technique that can identify volatile compounds. Common to all three techniques is speed, enabling direct introduction of the volatile compounds into the instruments without any pre-separation process. Therefore, these various instrumentations can be applied to study flavour release and in-situ flavour formation. Here we will concentration on PTR-MS and discuss applications and implications of PTR-MS on food flavour research.

Proton-Transfer-Reaction Mass Spectrometry (PTR-MS)

PTR-MS is based on a novel design for the chemical ionisation cell [10], which had developed out of the swarm technique of flow-drift-tube type [11]. The gas to be analysed is continuously introduced through a ventury type inlet system into the chemical ionisation cell (drift tube), which, besides buffer-gas (air), contains a controlled ion density of H_3O^+. Volatiles that have proton affinities larger than water (proton affinity of H_2O: 166.5 kcal/mol) are ionised by proton transfer from H_3O^+, and the protonated compounds are mass analysed in a quadrupole MS.

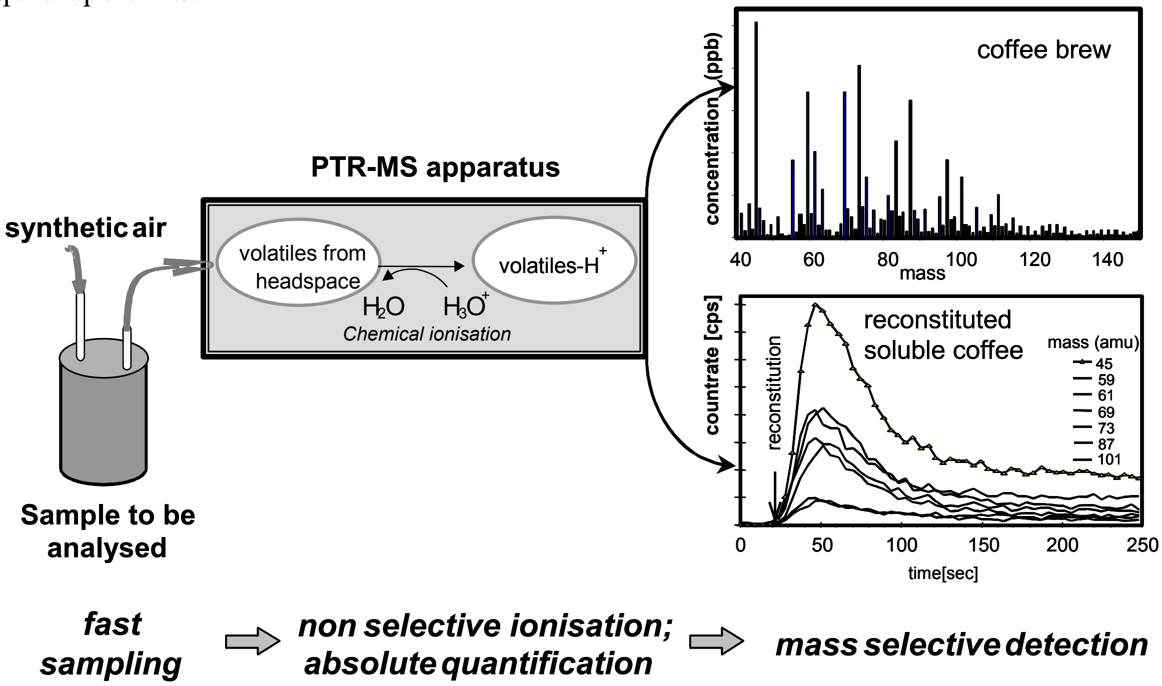

Figure: Two qualitatively distinct types of information can be obtained by PTR-MS. HS profiles can either be averaged over a given time window to yield concentration vs. mass spectra (static data). Alternatively, temporal changes can be analysed via time-intensity plots (dynamic data). The above static data represent an equilibrium HS profile above a coffee brew. The dynamic time-intensity traces below represent the temporal evolution of a series of selected mass while reconstituting soluble coffee.

Since its introduction in 1993, PTR-MS has been steadily improved and applied to a variety of fields. Medical and nutritional applications of breath analysis allow monitoring of metabolic processes in the human body [12,13]. Environmental applications include investigations of volatile emissions from decaying bio-matter [14,15], or diurnal variations of organic compounds in the troposphere. Monitoring of food processing was investigated on the example of coffee roasting [16,17]. Finally, PTR-MS has been shown to be an ideal tool for nose-space analysis while consuming food [18], and to measure Henry's Law Constants [19,20].

PTR-MS experiments provide information that can roughly be divided into two classes, as schematically shown in the figure below. On one hand, one can record direct-sampling mass spectra of a given HS profile, and average this data over a time window (static data). Such spectra closely match genuine HS distributions and can be used to assess authenticity, monitor deviations in production from a reference or classify products and raw materials. Provided mass peaks can be assigned to compounds, absolute HS-concentrations can be determined from HS profiles. On the other hand, one can record the temporal evolution of a series of mass intensities over a given time window (dynamic data).

In this contribution we will discuss a series of applications of PTR-MS to food flavours and outline the potential role and impact of PTR-MS to the future of food flavour science.

References

[1] R.S.T. Linforth, A.J. Taylor (1997) Eur. Patent Appl. 97305409.1

[2] A.J. Taylor, R.S.T. Linforth, B.A. Harvey, A. Blake (2000) *Food Chem.* **71**,327

[3] M.S. Brauss, R.S.T. Linforth, I. Cayeux, B. Harvey, A.J. Taylor (1999) *J. Agric. Food. Chem.* **47**,2055

[4] A.J. Taylor, R.S.T. Linforth (1998) *Nutr. Food Sci.* **4**,202

[5] W. Lindinger, J. Hirber, H. Paretzke (1993) *Int. J. Mass Spectrom. Ion Processes* **129**,79

[6] W. Lindinger, A. Hansel, A. Jordan (1998) *Int. J. Mass Spectrom. Ion Processes* **173**,191

[7] U. Boesl, H.J. Neusser, and E.W. Schlag (1978) *Zeitschrift für Naturforschung* **33a**,1546

[8] U. Boesl (1991) *Journal of Physical Chemistry* **95**,2949

[9] R. Zimmermann, H.J. Heger, C. Yeretzian, H. Nagel, U. Boesl (1996) *Rap. Comm. Mass Spectrom.* **10**,1975

[10] M.S.B. Munson, F.H. Field (1966) *J. Am. Chem. Soc.* **88**, 2621

[11] M. McFarland, D.L. Albritton, F.C. Fehsenfeld, E.E. Ferguson, A.L. Schmeltekopf (1973) *J. Chem. Phys.* **59**,6620

[12] J. Taucher, A. Hansel, A. Jordan, W. Lindinger (1996) *J. Agric. Food Chem.* **44**,3778

[13] J. Taucher, A. Hansel, A. Jordan, R. Fall, J.H. Futrell, W. Lindinger (1997) *Rapid Communications in Mass Spectrometry* **11**,1230

[14] C. Warneke, T. Karl, H. Judmaier, A. Hansel, A. Jordan, W. Lindinger, P. Crutzen (1999) *J. Global Biogeochem. Cycles* **13**,9

[15] R. Fall, T. Karl, A. Hansel, A. Jordan, W. Lindinger (1999) *J. Geophys. Res.* **104**,15963

[16] C. Yeretzian, A. Jordan, H. Brevard, W. Lindinger (2000) 218th ACS National Meeting: ion "*Flavor Release: Linking Experiments, Theory, and Reality*", New Orleans, D. Roberts, A. Taylor eds., American Chemical Society, pp 112-123

[17] C. Yeretzian, A. Jordan, R. Badoud, W. Lindinger (2002) *European Food Research and Technology*, in press

[18] M. Graus, C. Yeretzian, A. Jordan, W. Lindinger (2001) ASIC, *19th International Scientific Colloquium on Coffee*, Trieste (Italy) in press

[19] P. Pollien, C. Yeretzian (2001) ASIC, *19th International Scientific Colloquium on Coffee*, Trieste (Italy) in press

[20] T. Karl, C. Yeretzian, A. Jordan, W. Lindinger (2002) *Int J Mass Spectrom Ion Process,* submitted

Membrane Introduction Proton-Transfer-Reaction Mass Spectrometry

Michael Alexander

Pacific NW National Laboratory, Richland, WA, USA

Elena Boscaini, Tilmann Märk and Werner Lindinger

Institut fürIonenphysik der Leopold-Franzens-Universität, Innsbruck, Austria

Proton-transfer-reaction mass spectrometry (PTR-MS) is a rapidly expanding field that spans disciplines such as ion physics, atmospheric chemistry, food chemistry, and biology. The proliferation of PTR-MS research has been accelerated by the availability of a compact PTR-MS instrument resulting from the work of the late Werner Lindinger and associates at the University of Innsbruck[1]. The PTR-MS does not require calibration because concentrations can be calculated from a ratio of ion signals and well-known rate constants. The inherent accuracy, high sensitivity and rapid time response of the PTR-MS have resulted in multiple applications including the monitoring of volatile organic compound (VOC) emissions from fruit, coffee and meat as well as VOC compounds in the ambient air.

Another area of research in mass spectrometry that has experienced a resurgence of activity in recent years is membrane introduction mass spectrometry[2] (MIMS). In MIMS, the analyte is introduced into the ionization region of a mass spectrometer though a selective, semi-permeable, polymer membrane. The most commonly used membrane materials are silicone polymers, such as poly-dimethylsiloxane (PDMS), used either in a sheet or tube configuration. We present the results of initial studies that combine PTR-MS and MIMS research. First, the unique abilities of the PTR-MS are exploited to measure certain fundamental physical properties of a PDMS membrane, including solubilties and diffusion coefficients. Second, we demonstrate how the chemical selectivity of a PDMS membrane can be used to extend the capabilities of the PTR-MS instrument for two separate applications.

MIMS introduces the analyte into the mass spectrometer through a semi-permeable membrane using a process known as pervaporation. Three steps are involved in this process, adsorption of the analyte onto the membrane, diffusion through the membrane, and desorption from the inner surface of the membrane into the low-pressure ionization region. The permeation process is described by Fick's diffusion equations, given below in (Eqs. 1- 4) with the solutions for a hollow fiber membrane[3]:

$$1)\qquad \mathrm{F}(\mathrm{x},\mathrm{t}) = -\mathrm{AD}\cdot\left[\frac{\partial \mathrm{C}\,(\mathrm{x},\mathrm{t})}{\partial \mathrm{x}}\right] \qquad \longrightarrow \qquad \mathrm{F}_{\mathrm{st}} = \frac{2\pi \mathrm{LD}\cdot\left(\mathrm{C}_{\mathrm{S1}} - \mathrm{C}_{\mathrm{S2}}\right)}{\ln\left(\mathrm{r}_0\big/\mathrm{r}_1\right)} \qquad 3)$$

$$2)\qquad \frac{\partial \mathrm{C}\,(\mathrm{x},\mathrm{t})}{\partial \mathrm{t}} = \mathrm{D}\cdot\left[\frac{\partial^2 \mathrm{C}\,(\mathrm{x},\mathrm{t})}{\partial \mathrm{t}^2}\right] \qquad \longrightarrow \qquad t_{10-90\%} = 0{,}237\left(\frac{l^2}{D}\right) \qquad 4)$$

F(x,t) is the flow rate of analyte molecules through the membrane, C(x,t) is the concentration inside the membrane, D is the diffusion coefficient, A is the surface area of the membrane, x is the depth in the membrane, t is time, $t_{10\text{-}90\%}$ the rise time from 10% to 90% of the final signal level, L is the length of a tubular membrane, l is the membrane thickness, r_0 and r_1 are the inner and outer membrane diameters, F_{st} is the steady-state flow and C_{S1} and C_{S2} are the concentrations of analyte in the membrane at the entrance surface and exit surface, respectively. These quantities are illustrated schematically in Fig. 1 below.

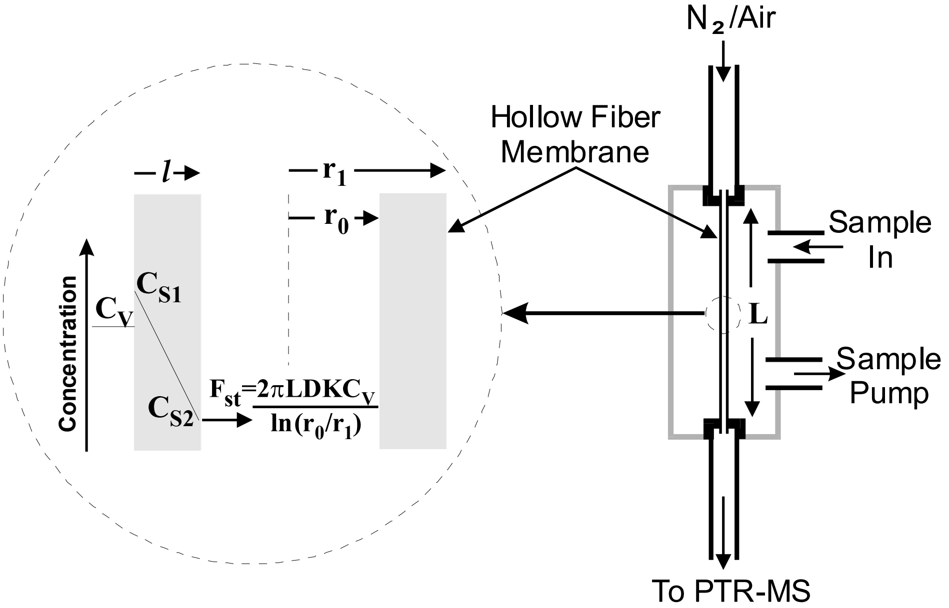

Fig. 1 Schematic diagram of the interface of the hollow fiber membrane to the PTR-MS with an illustration of the relevant experimental parameters

The right-hand side of Fig. 1 shows how the hollow fiber membrane physically interfaces with the sample stream and the PTR-MS. The membrane is mounted inside a stainless steel tube and sealed at each end as shown in Fig. 1. The interior of the membrane feeds directly into the PTR-MS drift region, held at a pressure of approximately 2 mbarr. A mass flow controller limits the flow of air or nitrogen through the membrane to 10 – 50 sccm, keeping the pressure near 2 mbarr. Sample air is drawn into the membrane assembly at atmospheric pressure and flows around the outside of the membrane at 100 – 200 sccm.

The left hand side of Fig. 1 shows a magnified section of the membrane labeled with the quantities described in Eqns. 1- 4. The steady state flow rate has been rewritten by setting $C_{S2} = 0$, because the inner surface of the membrane is swept by a carrier gas at very low pressure. The validity of this approximation will be demonstrated with experimental data. We then use the relationship $K = C_{S1}/C_V$, where K is the partition coefficient[4] to rewrite F_{st} in Eqn. 5:

5) $$F_{st} = \frac{2\pi LDKC_V}{\ln\left({r_0}/{r_1} \right)}$$

We demonstrate how the PTR-MS can be used to determine F_{st} and $t_{10\%-90\%..}$ These results can be related to the diffusion coefficient D and the partition coefficient K. The data will be presented as a function of membrane thickness and flow rate for VOC's with various functional groups that display a range of molecular properties such as polarity, polarizability and mass. Data will also be presented on the effect of temperature on both F_{st} and $t_{10\%-90}$. These will be explained using an Arrhenius-type relationship. An example of these results is shown in figure 2.

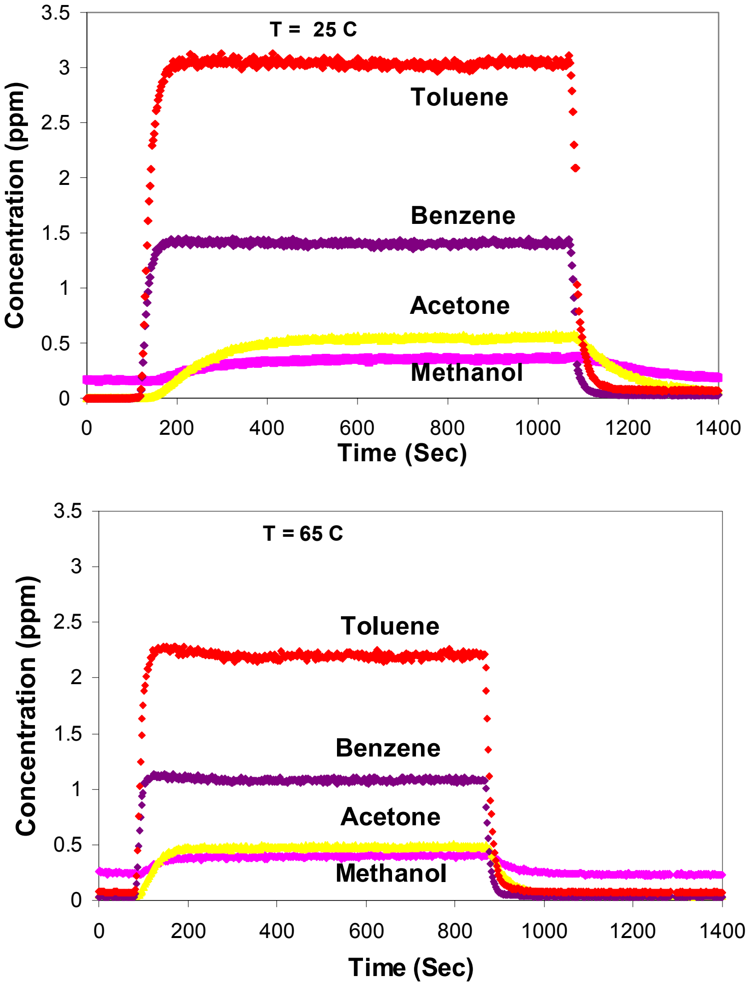

Fig. 2 Time dependent concentrations of VOC's inside the membrane for temperatures of 25 and 65 C

These data were obtained by using a three-way valve to modulate the composition of the sample stream between zero air and a mixture of several VOC's. The concentration of the VOC's in the mixture were determined by direct introduction into the PTR-MS and found to be 5 ppm for acetone, 3.5 ppm for benzene and toluene, and 2.8 ppm for methanol. Fig. 2 illustrates both the rise time and the steady state flow dependence of the different VOC's at two different temperatures. This serves as an illustration of how the ability of the PTR-MS to measure absolute concentrations of multiple chemical species can be used to quickly characterize critical physical properties of a semi-permeable membrane. Although this initial work used a relatively well-characterized membrane material, these results clearly demonstrate the potential of the PTR-MS to rapidly characterize new membrane materials for use in a variety of applications.

The second area that will be presented is the use of the properties of the semi-permeable membrane to enhance the capabilities of the PTR-MS. We demonstrate how the difference in transmission rates through the membrane can be used to eliminate certain isobaric interferences in the PTR-MS such as acetone and propanal at m/Z = 59. Fig. 3 shows the difference in both rise time and steady state concentration when 200 ppb samples of acetone and propanal are introduced to the membrane. The potential for time modulated MIMS in resolving this type of isobaric interference in the PTR-MS is discussed.

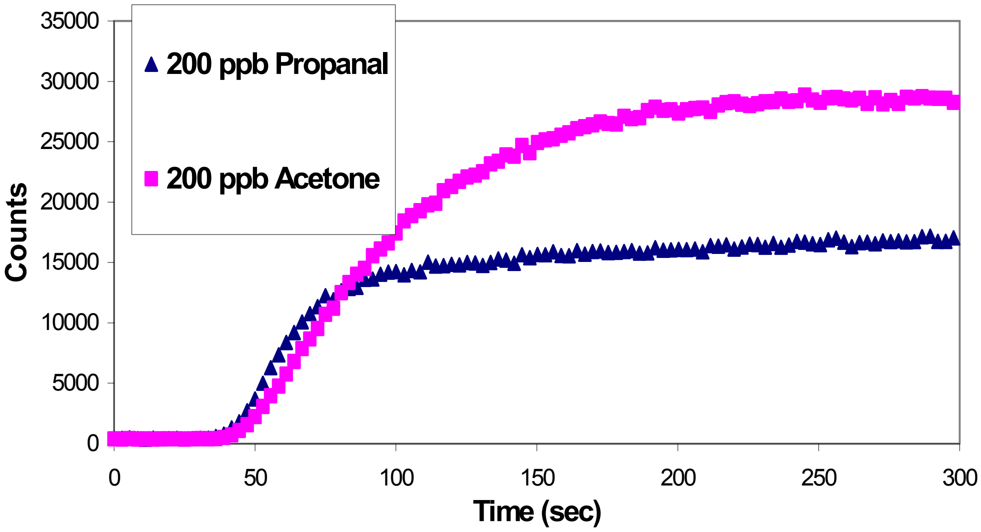

Fig. 3 Variations in rise time and steady state values for m/Z =59 obtained for 200 ppb propanal and 200 ppb acetone in separate experiments

Finally, data will also be presented that show how the ability of the membrane to exclude water while transmitting volatile organic compounds can allow the use of the PTR-MS for making measurements in extremely humid environments. This further extension of the PTR-MS capabilities using membrane introduction is demonstrated in measurements of VOC's over the headspace of hot soup. The significance of these results and future research directionswill be discussed.

Acknowledgements

We would like to acknowledge the US DOE and the University of Innsbruck, Austria for supporting this work as well as additional support in part by the Austrian FWF, Wien, Austria.

References

---

[1] W.Lindinger, A. Hansel and A, Jordan, *Chem. Soc. Rev*. **27** (1998) 347

[2] N. Srinivasan, R.C. Johnson, N. Kasthurikrishnan, P. Wong and R.G. Cooks, *Anal. Chim. Acta* **350** (1997) 257

[3] F.L. Overney and C.G. Enke, *J. Am. Soc. Mass Spectrom* **7** (1996) 93

[4] J.W. Grate and M.H. Abraham, *Sensors and Actuators B* **3** (1991) 85

Bond-forming ion molecule reactions

D. Ascenzi, P. Franceschi, T.G.M. Freegarde, P. Tosi and D. Bassi[*]

Dipartimento di Fisica and INFM, Università degli Studi di Trento, I-38050 Povo, Italy

The dynamics of ion molecule reactions are characterized by the presence of a variety of reaction channels. Major reaction channels are generally related to charge-exchange processes [1], eventually associated with dissociation phenomena. Bond-forming reaction channels, *i.e.* collisions leading to the formation of new chemical bonds are usually less probable than charge-exchange channels. However – even when their cross-section is relatively small – they are of great interest because they play a key role in the synthesis of molecular species in interstellar space.

In Trento, bond-forming ion molecule reactions have been extensively investigated using a high-sensitivity guided beam apparatus [2]. Collisions involving both singly and doubly charged ions have been considered. In particular, we have focused our attention on the formation of molecular dications [3-5] and on the synthesis of polyatomic molecules containing the CN bond [6].

In recent years the structure and the gas-phase reactivity of small doubly charged molecules have attracted increasing interest [7-10]. These species are usually unstable because of the Coulomb repulsion $XY^{2+} \rightarrow X^+ + Y^+$, however, in some cases they can be either thermodynamically stable or long lived [11]. Such molecules exhibit high reactivity and their exoergic reactions with other molecules may release several electron volts in kinetic energy of the products. As an example, He_2^{2+} has been proposed as a source of propulsive energy with properties which far exceed those of all known propellants [12].

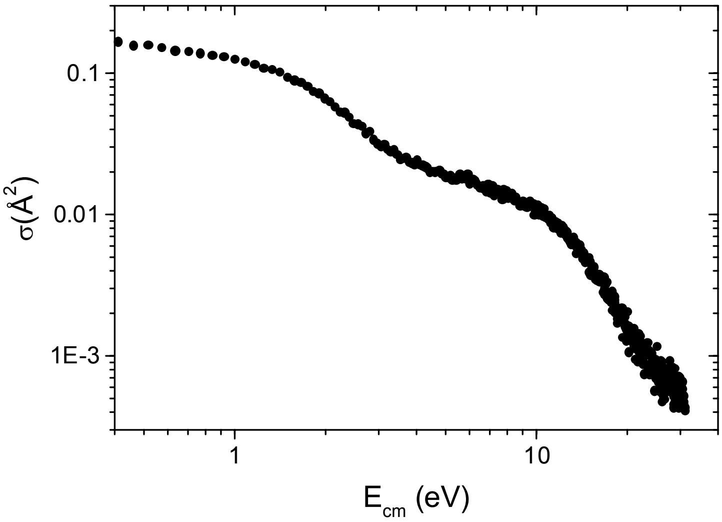

Figure1: Integral cross-section as a function of collision energy for the production of ArC^{2+} in the reaction of Ar^{2+} with CO [4].

We have produced molecular dications such as ArX^{2+} (where X= C, N, O) [3-5,13] by reaction of an atomic or molecular dication with a neutral partner. The remarkable feature of these reactions is the formation of a new bond in a process which involves doubly charged ions both as reactants and products. Bond-forming reactions usually produce singly charged ionic products [14-17].

Aromatic and polyaromatic molecules are known to be present in extraterrestrial matter such as carbon stars, molecular clouds and meteorites; their presence has been observed in astronomical spectra [18-20] and the recent observation of benzene in interstellar space [21] has aroused further interest in the chemical behaviour of the entire class of molecules for the

---

[*] bassi@science.unitn.it

modelling of astrophysical processes. Given the relevance of molecules containing carbon and nitrogen atoms in such context, an understanding of mechanisms by which C-N bonds might be formed from C-C chain or ring reactants should provide insights into the possible astrophysical origin of life's building blocks [22,23].

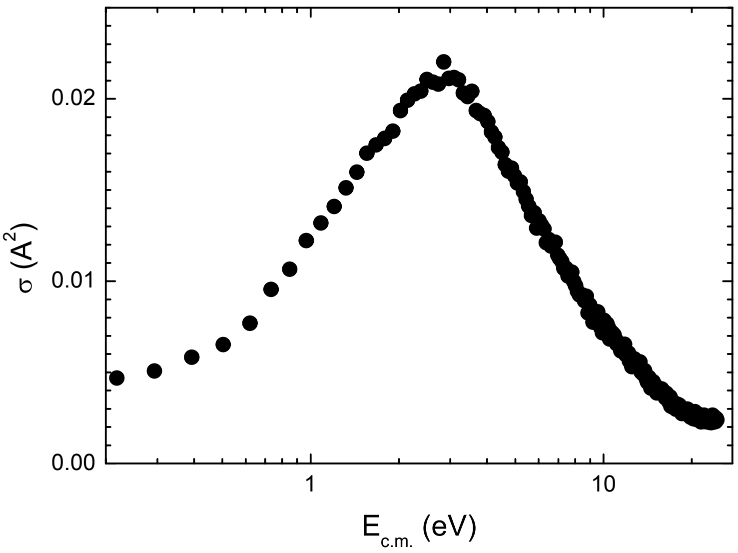

Figure 2: Integral cross-section as a function of collision energy for the reaction $CO^{2+} + Ar \rightarrow ArC^{2+} + Ar$ [5].

To this end, much attention has recently been devoted to studying the growth of complex molecules containing C-N bonds. Several reaction mechanisms have been proposed including the reaction of CN radicals with unsaturated hydrocarbons [24-26], and the aggregation of cyanoacetylene, which may be catalysed by doubly charged PAH or fullerene cations [27]. We have investigated another possible pathway based on the reaction of N^+ with benzene [6]. This was suggested by the observation that the nitrogen ion is isoelectronic with the neutral carbon atom, whose insertion into a benzene ring has recently been observed both experimentally [28] and computationally [29] to form, under single collision conditions, the seven-membered ring C_7H_5 radical. The reaction of C^+ ions with benzene has been studied in the past [30,31] providing the first evidence of a $C_7H_5^+$ intermediate.

We have observed product ions such as cyanoallene CH_2CCHCN^+, cyanopolyacetylene HC_5N^+, and HC_5NH^+, as well as lighter compounds such as H_2CN^+ and $C_2NH_2^+$. Our results indicate that aromatic hydrocarbons can be directly converted into cyano and amino molecules, thus giving a complementary pathway to the reaction mechanisms mentioned above.

Acknowledgements.

We acknowledge the financial support of the European Commission, grant No. HPRN-CT-2000-00027.

References

[1] R. Candori, S. Cavalli, F. Pirani, A. Volpi, D. Cappelletti, P. Tosi and D. Bassi, *J. Chem. Phys.* **115** (2001) 8888
[2] D. Bassi, P. Tosi, and R. Schlögl, *J. Vac. Sci. Technol. A* **16** (1998) 114
[3] P.Tosi, R. Correale, W. Lu, S. Falcinelli and D. Bassi, *Phys. Rev. Letters* **82** (1999) 450
[4] P.Tosi, R. Correale, W. Lu, and D. Bassi, *Chem. Phys. Letters* **310** (1999) 180
[5] W. Lu, P. Tosi, and D. Bassi, *J. Chem. Phys.* **112** (2000) 4368
[6] D. Ascenzi, P. Franceschi, T.G.M. Freegarde, P. Tosi and D. Bassi, *Chem. Phys. Lett.* **346** (2001) 35
[7] M. Larsson, *Comments At. Mol. Phys.* **29** (1993) 39
[8] D. Mathur, *Phys. Rep.* **225** (1993) 193

[9] Z. Herman, *Int. Rev. Phys. Chem.* **15** (1996) 299

[10] D. Schröder and H. Schwarz, *J. Phys. Chem. A* **103** (1999) 7385

[11] A. S. Mullin, D. M. Szaflarski, K. Yokoyama, G. Gerber, and W. C. Lineberger, *J. Chem. Phys.* **96** (1992) 3636

[12] C. A. Nicolaides, *Chem. Phys. Lett.* **161** (1989) 547

[13] Work in progress (in cooperation with J. Harvey and coworkers)

[14] S. D. Price, M. Manning, and S. R. Leone, *J. Am. Chem. Soc.* **116** (1994) 8673

[15] Z. Dolejšek, M. Fárník, and Z. Herman, *Chem. Phys. Lett.* **235** (1995) 99

[16] K. A. Newson and S. D. Price, *Chem. Phys. Lett.* **269** (1997) 93

[17] K. A. Newson and S. D. Price, *Chem. Phys. Lett.* **294** (1998) 223

[18] F. Salama, G.A. Galazutdinov, J. Krelowski, L.J. Allamandola and F.A. Musaev, *Astrophys. J.* **526** (1999) 265

[19] S. Messenger, S. Amari, X. Gao, R.M. Walker, S.J. Clemett, X.D.F. Chillier, R.N. Zare and R.S. Lewis, *Astrophys. J.* **502** (1998) 284

[20] D.A. Beintema, *Astrophys. Space Sci.* **255** (1998) 507

[21] J. Cernicharo, A.M. A.G Heras, G.M. Tielens, J.R. Pardo, F. Herpin, M. Guelin and L.B.F.M. Waters, *Astrophys. J.* **546** (2001) L123

[22] A.G.G. M. Tielens and B. Charnley, *Orig. Life Evol. Biosph.* **27** (1997) 23

[23] P. Ehrenfreund and S.B. Charnley, *Annu. Rev. Astron. Astrophys.* **38** (2000) 427

[24] N. Balucani, O. Asvany, L.C.L. Huang, Y.T. Lee, R.I. Kaiser, Y. Osamura and H.F. Bettinger, *Astrophys. J.* **545** (2000) 892; L.C.L. Huang, O. Asvany, A.H.H. Chang., N. Balucani, S.H. Lin, Y.T. Lee, R.I. Kaiser and Y. Osamura, *J. Chem. Phys.* **113** (2000) 8656 and references therein.

[25] L.C. Huang, N. Balucani, Y.T. Lee and R.I. Kaiser, *J. Chem. Phys.* **111** (1999) 2857

[26] D. Smith and P. Spanel, *Mass Spec. Rev.* **14** (1995) 255

[27] R.K. Milburn, A.C. Hopkinson, J. Sun and D.K. Bohme, *J. Phys. Chem. A* **103** (1999) 7528

[28] R.I. Kaiser, I. Hahndorf, L.C. Huang, Y.T. Lee, H.F. Bettinger, P.v.R. Schleyer, H.F. Shaefer III and P.R. Schreiner, *J. Chem. Phys.* **110** (1999) 6091

[29] H.F. Bettinger, P.v.R. Schleyer, H.F. Shaefer III, P.R. Schreiner, R.I. Kaiser and Y.T. Lee, *J. Chem. Phys.* **113** (2000) 4250

[30] R.D. Smith and J.J. DeCorpo, *J. Phys. Chem.* **80** (1976) 2904

[31] D.K. Bohme, A.B. Rakshit and H. I. Schiff, *Chem. Phys. Lett.* **93** (1982) 592

From Quantum Calculations

F.A. Gianturco, F. Sebastianelli, E. Scifone

Department of Chemistry, The University of Rome,
Citt Unversitaria, 00185 Rome, Italy

The ionization of pure rare gas (Rg) clusters by photon or electron impact causes a great deal of energy to be deposited in these weakly bound, van der Waals (vdW) aggregates. We have focussed our attention on $^4He_n^+$ and Ne_n^+ clusters with a fairly small number of particles as result of the impact ionization of much larger droplets and have considered the nanoscopic processes which are likely to occur in them after the initial electron emission has taken place. Quantum, ab initio calculations of the interaction forces [1,2] and examination of the most stable confgurations [3] when the most probable ionic cores are considered, have been able to tell us what is the most frequent occurrence within such aggregates even when the number of particles is fairly small. Our theoretical treatments and our numerical calculations will be shown to provide a rather detailed descriptions of such ionic cores and of the layering of the solvent atoms around them after their formation [4]. Such results are indicative of a rather fast nucleation process in such systems and of a very limited charge propagation after the initial ionic monomer is formed by the impinging projectiles. The most recent results from quantum dynamics will be presented at the Meeting.

References

[1] F.A. Gianturco and F. Filippone, *Europhys. Lett.* **44** 585 (1998)
[2] F.A. Gianturco and F. Sebastianelli, *Eur. Phys. J. D* **10** 399 (2000)
[3] E. Scifone and F.A. Gianturco, in preparation
[4] F.A. Gianturco, F. Sebastianelli and E. Yurtsever, *Int. J. Mass. Spectr.* (2001)

Pseudorotational Dynamics of Small Molecular Species

Frank Hagelberg

Computational Center for Molecular Structure and Interactions,
Jackson State University,
Jackson, MS 39217, U.S.A.

The adiabatic approximation has been successful in describing numerous classes of molecular motion and interaction phenomena /1/. It relies on the concept of the Potential Energy Surface (PES) and assumes that a molecular system adopts its parameter dependent ground state at any stage of its evolution. Within the confines of the adiabatic approximation, the molecular motion is computationally predictable if the ground state PES of the respective system is known. This approach, however, meets its limits wherever highly dynamic situations are involved, such as in fast collisions or scattering reactions at high energy. Further, the adiabatic approximation loses its validity in cases of degenerate or near-degenerate electronic ground states, as is encountered in the vicinity of a conical intersection /1/. This contribution focuses on a third type of molecular processes which transcends the regime of this approximation, namely the dynamic behavior of molecules close to the threshold of dissociation. Since disintegration phenomena frequently involve high kinetic energies, their adequate representation demands in general the use of a theory that allows for the inclusion of non-adiabatic effects.

Such a formalism is available with the Electron Nuclear Dynamics (END) Theory /2/, which has been designed to provide a full description of the dynamic development of the electronic system. A particular strength of the END Theory, which makes this approach a particularly plausible choice for the investigation at hand, consists in its independence of any PES constructions. Since the processes studied in this work are characterized by a sizeable dynamic coupling between electrons and nuclei, as will be outlined in further detail in Sec. III, any use of the PES concept appears artificial or, in the best case, computationally unnecessarily extensive, requiring the implementation of a complex scheme of multiple PES.

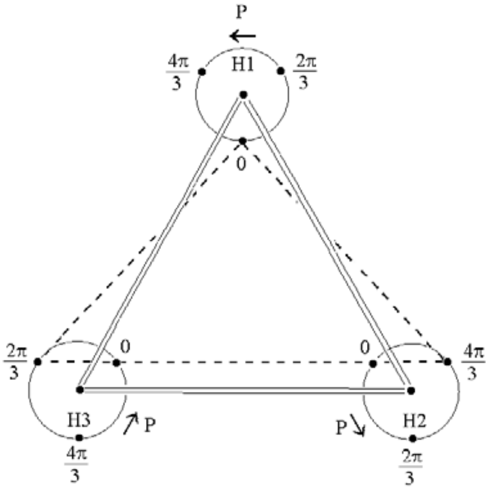

Fig1.: The model adopted for the description of pseudorotation. P denotes the initial momentum imparted to each nucleus in H_3^+.

The present work emphasizes triatomic species as well as a particular type of molecular motion, namely pseudorotation, involving the coordinated, phase related motion of all atoms in a molecule or cluster. The ideal case of circular pseudorotation of a triatomic unit is indicated in Fig.1.

Pseudorotation of a triatomic molecule is conveniently defined in terms of the two orthogonal deformation coordinates of such a unit. In the special case of circular pseudorotation, these two degrees of freedom behave like sinusoidal functions of time, being equal in amplitudes and shifted with respect to each other by a phase angle of $\pi/2$.

We will clarify that this process is a particularly worthwhile object of dynamics studies, since it exhibits an extraordinary range of interactions of nuclear degrees of freedom, both among themselves and with electronic degrees of freedom/3,4/. More specifically, simulations based on END theory are performed with the aim to extend the current understanding of the dynamic features of pseudorotation into the non-adiabatic regime. By the examples of H_3^+ and Li_3^+, it is shown that the total nuclear angular momentum of the molecules, which is considered as a conserved quantity in the adiabatic region, provides a useful guideline for the dynamic evolution of the system as a function of the difference ΔE between the total energy of the dynamic molecule and its static equilibrium energy in the ground state. Thus, the total nuclear angular momentum is mostly pseudorotational in nature at low energy where the kinetic effects are sufficiently small. In an intermediate energy interval, it is a combination of components due to both pseudorotation and spatial rotation. At still higher energy, it ceases to be a constant of motion, which it attributed to the onset of a sizeable dynamic coupling between the nuclear and the electronic system.

Correspondingly, we characterize the electron dynamics of the molecular species in terms of electronic angular momentum expectation values. At energies ΔE in excess of about 3 eV for H_3^+ and 0.1 eV for Li_3^+, a rapid angular momentum exchange between the alpha and the beta system is recorded. This phenomenon coincides with the occurrence of maximum interatomic distances within the molecule and is thus interpreted as an electronic response to an extreme amount of bond stretching. This behavior signifies a partial rupture of the covalent bond and thus precedes the dissociation of the molecule as a whole. It is also demonstrated that the divergent reactions of the alpha and the beta system correlate with the formation of nonzero spins at the atomic centers of the molecules and in further consequence with a complex pattern of spin exchange processes between these centers. With the elapse of time, the phase relation between the angular momentum contributions of the alpha and the beta system is lost, and the angular momentum exchange proceeds between all molecular components, i.e. the nuclear and the electronic degrees of freedom.

The observations summarized above can be cast into the language of electronic excitations. By evaluating a sequence of electronic bases, each consisting of the UHF molecular ground state determinant and all determinants arising from single and double substitutions for a succession of geometries adopted by the molecule in the course of its evolution in time, it is possible to calculate expansion coefficients which carry the information about the excitation content of the electronic system at any stage of the motional process (see Fig.2). This analysis yields characteristic differences between spin alpha and spin beta projections of the dynamic wavefunctions. In particular, it turns out for Li_3^+ in the examined energy interval that the promotion of the HOMO to the LUMO is associated with a near – constant phase difference of about π between the corresponding excitation coefficients, giving rise to the emergence of pronounced spin polarization effects within the molecule.

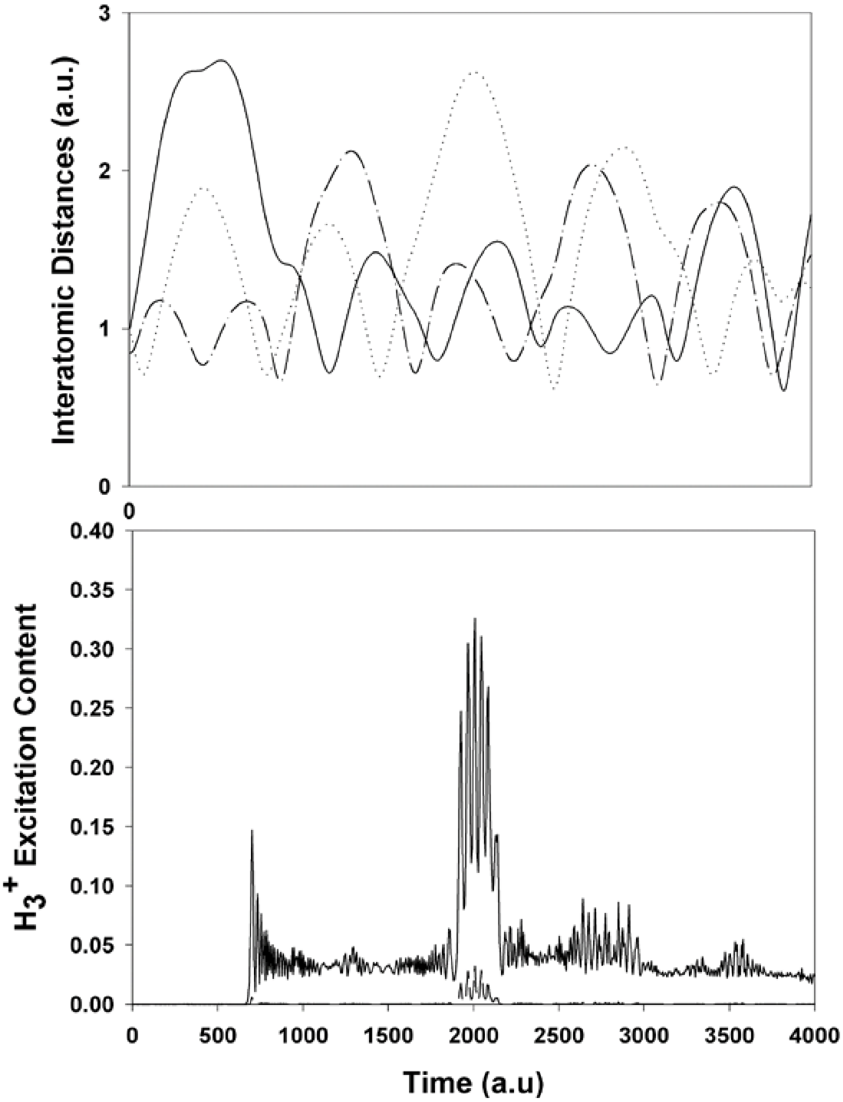

Fig.2: Upper panel: The three interatomic distances of H_3^+ in pseudorotation at $\Delta E = 3.9$ eV versus time. Lower panel: For the same situation, the total electronic excitation probability versus time.

The concepts introduced in this work are suitable for the investiagtion of pseudorotating open shell species such as Alkali$_3$, which have been experimentally studied in great detail /5/, under the aspect of dynamic coupling between the nuclear and the electronic systems.

References

---

[1] See for instance: Englman, R., The Jahn-Teller Effect in Molecules and Crystals; Wiley-Interscience: London, 1972; p.9.

[2] Deumens E., Diz A., Longo R., Öhrn, Y. *Rev Mod Phys* 1994, **66**, 917.

[3] F.Hagelberg, *Int.J.Quant.Chem.*, 2000, **80**, 966.

[4] F.Hagelberg, *Int.J.Quant.Chem.*, 2001, **85**, 72.

[5] Delacretaz, G., Grant, E.R., Whetten, R.L., Wöste, L., Zwanziger, J.W. *Phys Rev Lett* 1986, **56**, 2598; Dugourd,Ph., Chevaleyre,J., Antoine,R., Broyer,M., Wolf,J.P., Wöste,L., *Chem Phys Lett.* 1994, **225**, 28 .

Acknowledgment.

This work was supported by the National Science Foundation through the CREST Program (HRD-9805465).

Quantum Chemical Calculations of Ionization Potentials and Dimerization Energies of Ozone and Chloro-oxides: Two Easy Cases and a Difficult One

Michael Probst*, K. Hermansson†, Jan Urban‡, P. Mach‡, J. Fedor‡ and T. D. Märk*

* *Institut für Ionenphysik, Universität Innsbruck, Technikerstraße 25, 6020 Innsbruck, Austria*
† *The Angström Laboratory, Materials Chemistry, University of Uppsala, Box 538, 75121 Uppsala, Sweden*
‡ *Department of Biophysics and Chemical Physics, Comenius University Bratislava, Mlynska dolina F1, 84248 Bratislava, Slovakia*

Introduction

Ionization potentials (IPs) of Cl_2O [1] and of ClO_2 and O_3 [2] and their dimers were recently measured via electron impact ionization close to threshold. For these systems, we have performed quantum chemical calculations to verify the experimental results, to find the equilibrium structures of the three dimers and to obtain information about the electronic structure of monomers and dimers. It turns out that the two chloro-oxides pose no particular difficulties (Cl_2O: 11.15 eV and ClO_2: 10.55 eV; dimers ~0.5 eV lower) but that in case of ozone measurement and calculation disagree severely. This leads to an investigation of the structure of ozone dimer and it is suggested that not a weekly bound O_3+O_3 complex but an O_6 or O_4+O_2 entity is causing the signal.

Calculations

All quantum chemical calculations were performed with the 6-311++(2df,2p) basis set. The MP2 method (perturbation theory after a Hartree-Fock calculation) and density functional (DFT) calculations with the 3-Parameter Becke exchange functional and the Lee-Yang-Parr correlation functional were checked against each other. We found no case where their results disagree with each other and can therefore recommend the DFT calculations also for calculations of energetic properties of these molecules. This is not evident a priori because the electronic state of ozone and chloro-oxides is expected to partially have an open-shell character with contributions from more than one determinant.

a) ClO_2 and its dimer:

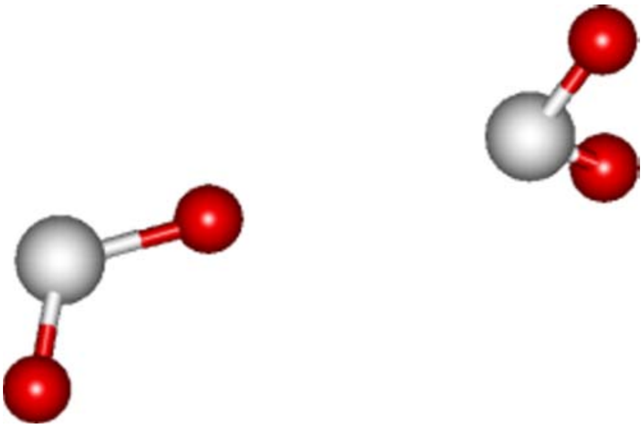

There is good agreement between the values of the experiment (10.55±0.02 eV) and the ionization potential calculated as the difference between the energies of ClO_2 and ClO_2^+ (10.76 eV). This also indicates that the species present is O-Cl-O and not, for example the isomer Cl-O-O. Good agreement is also found for $(Cl_2O)_2$. The 'solvation effect' caused by dimerization leads to a lowering of the IP to 10.04 eV (Experiment [2]: 9.87±0.2 eV). The dimer is found to have the structure depicted above. Its nearly linear Cl-O···Cl angle resembles the water dimer. An analysis of the charge distribution shows that the binding energy of ~0.06 eV (~1.4 kcal/mol) and the dimer structure is mostly a result of the interaction of the positive partial charge of one oxygen (δ^+=0.3e) with the dipole moment of the other monomer unit.

b) Cl_2O and its dimer:

There is good agreement between calculated (11.15 eV) and experimental (11.04±0.01 eV) ionization potentials. Dimerization lowers the IP to 10.66 eV (experiment: 10.47±0.01 eV). While the most stable structure of the monomer is Cl-O-Cl (C_{2V} symmetry), the dimer exhibits a more asymmetric structure compared to ClO_2 (picture on the right side; the shortest Cl-O distance between both monomers is ~2.75 Å). The dimer binding energy is more than twice as large than for ClO_2 (~0.14 eV = ~3.2 kcal/mol). An analysis of the bonding in terms of electrostatic multipoles is more complicated in this case since the dipole moment of Cl_2O is rather small.

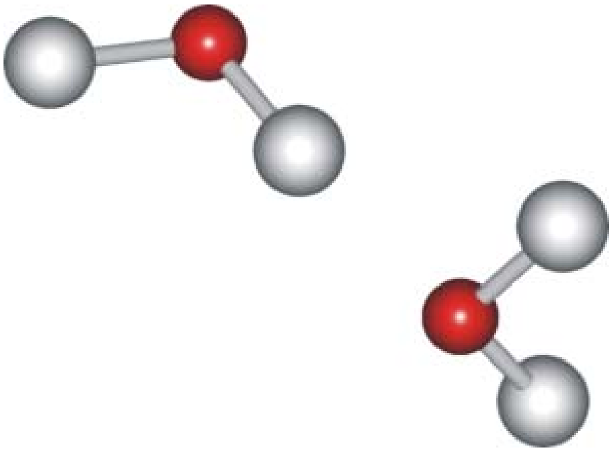

c) O_3 and its dimer:

The calculated IP of O_3 (12. 65 eV) is close to experimental values ([2]: 12.70 ± 0.02 eV; other experiments gave results between this value and 12.87 eV). The *neutral* ozone dimer seems to be asymmetric and very weekly bound (right side). Indeed, only if the calculations are not corrected for the artificial stabilization caused by the basis set superposition error, a binding energy of ~0.1 eV is obtained and more precise calculations lead binding energies between zero and this value.

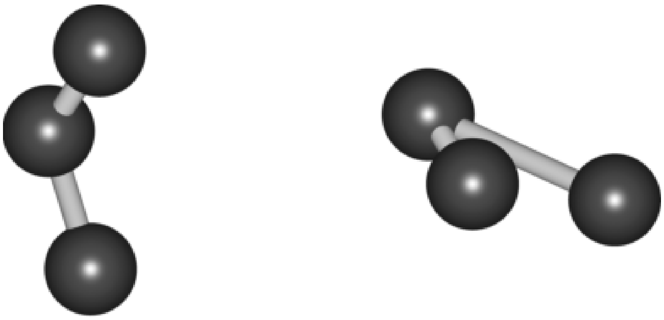

The binding energy of the *cationic* dimer was calculated to ~0.7 eV (Due to convergence problems, this value corresponds to a nearly but not fully optimized geometry). This is in disagreement with dimerization energy deducted from the ionization experiments:

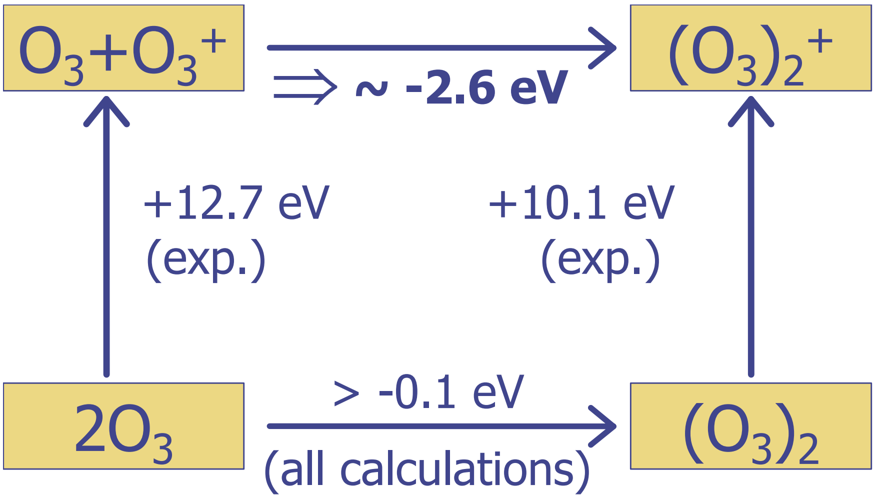

From this thermodynamic cycle, it is evident that – provided the monomer binding energy is really close to zero – the unusually large difference between the measured IP of the monomer and that of the dimer leads to a large binding energy of the dimer cation.

Provided that both calculation and experiment are in principle correct, this discrepancy can be only resolved if alternative structures for the O_6 unit are considered and the idea of a 'conventional' O_3 dimer is abandoned. Among the candidates screened by us, we found only one metastable structure in agreement with the measured IP of 10.1 eV. This structure (picture below) can be viewed as an O_4+O_2 adduct. Other candidates like cyclic or octahedral O_6 exhibit interesting features but are either extremely unstable or have an incompatible IP. The IP of this O_4+O_2 complex is calculated to be 10.4 eV – still within the experimental error limits. While this is not a proof that this and no other compound causes the measured signal, it is a strong indication that the seemingly too low experimental IP for the dimer can be explained by this or a similar species and that probably an interesting rearrangement $(O_3)_2 \rightarrow O_2+O_4$ takes place. It is noteworthy that after our calculations were completed, an unambiguous chemical analysis of O_4 has been described for the first time [3].

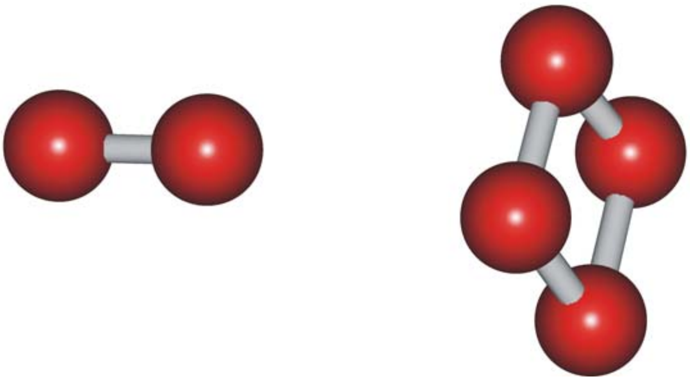

References

[1] G. Hanel, J. Fedor, B. Gstir, M. Probst, P. Scheier T. D. Märk, P. Tegeder and N. J. Mason, *J. Phys. B*, in print, 2002

[2] M. Probst, K. Hermansson, J. Urban, P. Mach, D. Muigg, G. Denifl, T. Fiegele, N. J. Mason, A. Stamatovic, T. D. Märk, *J. Chem. Phys.* **116** p.984, 2002

[3] F. Cacace, G. de Petris, A. Troiani, *Angew. Chem.* **113**, p.4186, 2001

IR-Photodissociation Spectroscopy of Mass-selected Gas Phase Cluster Ions

Knut R. Asmis

Institut für Experimentalphysik, Freie Universität Berlin, Arnimallee 14, D 14195 Berlin

Recent results on the IR-photodissociation spectroscopy of mass-selected gas phase cluster ions in the spectral region from 600 to 1600 cm^{-1} are presented. The experiments were performed employing a novel experiment setup, consisting of a tandem mass spectrometer, a temperature-controllable He-filled radio frequency ion trap and the free electron laser FELIX (FOM Institute for Plasmaphysics, Nieuwegein, The Netherlands). The application of this technique to the study of the IR-spectroscopy of transition metal oxide cluster cations and halogen atom - halogenhydrid cluster anions of the type $Br^{-}\cdot(HBr)_n$ with $n = 1\text{-}3$ is described. In combination with electronic structure calculations these results allow for a unique structural characterization of the studied cluster ions. For both types of cluster ions these experiments represent, to the best of our knowledge, the first experimentally determined gas phase IR spectra of these compound classes.

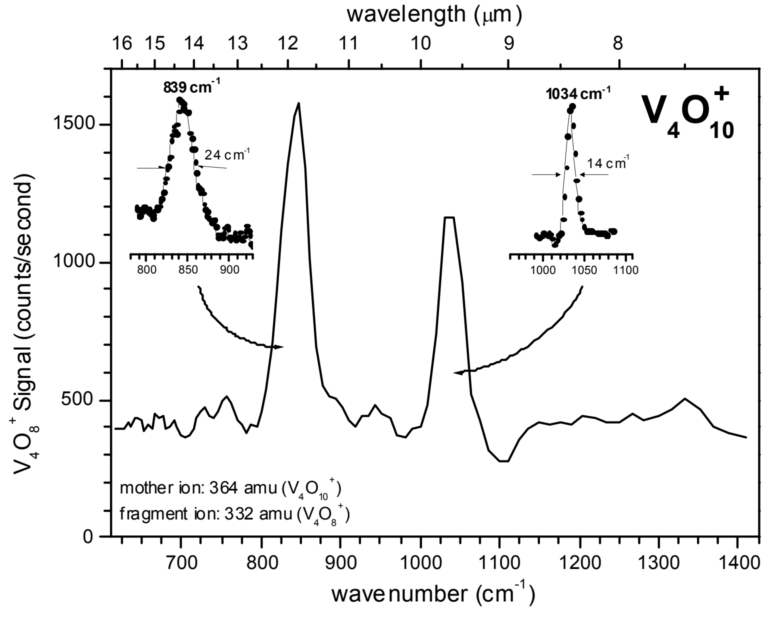

Fig. 1: IR-photodissociation spectrum of $V_4O_{10}^+$ measured by monitoring the O_2-loss channel ($V_4O_8^+$).

Collisions of Na^+ with C_{60}: Energetics of Endohedral $Na@C_{60}^+$, and Heat Capacity of C_{60}

R. Deng and O. Echt

Department of Physics, University of New Hampshire, Durham, NH 03824, USA

Abstract:

We generate endohedral $Na@C_{60}^+$ by gas-phase collisions of Na^+ with C_{60}. A model that includes radiative cooling and a distribution of energies accurately reproduces the ion yield from its appearance at 29.6 eV to its disappearance above 55 eV. We derive a dissociation rate of 94 000 s^{-1} when the internal excitation energy of $Na@C_{60}^+$ reaches 49.1 ± 0.5 eV. Its dissociation energy is found to be 10.17 ± 0.02 eV (statistical error) if one assumes an Arrhenius factor of $\nu_o = 5\times10^{19}$ s^{-1}. The dependence of the breakdown energy on the temperature of the effusive C_{60} source implies a vibrational heat capacity of C_{60} of 12.6 ±1.4 meV/ºC for temperatures of 500 to 570 ºC.

Introduction:

Many elements have been incorporated into C_{60} or larger fullerenes. One method involves implantation of energetic ions or atoms into pre-formed fullerenes. Particles may be implanted either into fullerene films [1-3], or into gas-phase fullerenes [4, 5]. In the latter case, quantities of particular interest are the insertion threshold energy, and the "breakdown energy" which we loosely define as the energy at which the adduct ion will be so highly excited that it has 50 % probability of breaking before it can be identified. These quantities have been determined for a number of systems, but experimental uncertainties are usually large. No attempts have been reported to quantitatively model the observed yield of adduct ions over an extended range of collision energies.

The insertion threshold may range from a few eV to a value that is too large to form a long-lived adduct ion as, for example, in the case of $K^+ + C_{60}$ collisions [3, 4]. On the other hand, the breakdown energy will reflect the stability of the collision complex and agree closely with the dissociation energy of C_{60}^+ if loss of C_2 is the preferred decay channel, and the caged atom or ion does not significantly weaken or strengthen the carbon-carbon bonds. In the present contribution we report an experimental study of gas-phase collisions between Na^+ and C_{60}. We model our data with due consideration of the energy spread in the collision complex as well as radiative cooling. The breakdown energy is found to depend on the temperature of the effusive C_{60} beam which provides a novel method to measure its heat capacity.

Experiment:

Fig. 1 shows an overview of the setup. In short, a pulsed beam of sodium ions, accelerated to the desired energy, collides with an effusive beam of C_{60} under 90° in the ion source of a time-of-flight (TOF) mass spectrometer. Product ions that are formed as a result of collisions are accelerated by pulsed extraction potentials towards the ion detector at the end of a drift tube. The TOF mass spectra reflect the ion distribution 9 to 11 μs after the collision. Sodium ions are generated by surface ionization. These sources provide ion beams with a very small kinetic energy spread of about $2\,k_BT \approx 0.3$ eV [6].

The Na^+ ion current is measured for each spectrum by moving an electrode into the ion beam where it intersects the C_{60} beam. The C_{60} flux is continuously monitored by a quartz microbalance. Data are corrected for changes in ion current and C_{60} flux. For additional details see [7].

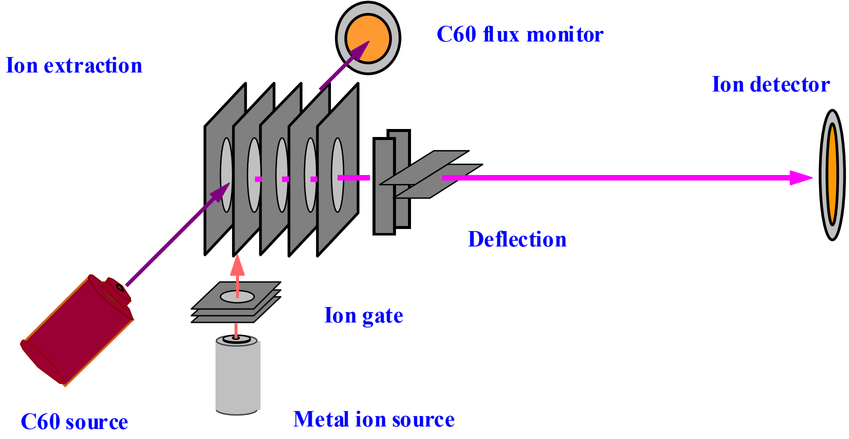

Fig. 1 Experimental setup. A beam of C_{60} collides with Na^+ ions emitted from a surface ionization source. Collision product ions are extracted into a TOF mass spectrometer by pulsed potentials.

Data analysis:

We model dissociation of the parent ion $Na@C_{60}^+$ with the Arrhenius relation for the rate constant $k(T)$ of a canonical ensemble at temperature T,

$$k = \nu_o \exp\left(-\frac{E_a}{k_B T}\right) \tag{1}$$

ν_o is a frequency factor taken to be 5×10^{19} s^{-1} [8, 9], k_B is Boltzmann's constant, and E_a is the activation energy for dissociation. Finite heat bath theory [10] is applied to transform the excitation energy E^* of $Na@C_{60}^+$ into a fictitious heat bath temperature T. E^* is the sum of three terms,

$$E^* = E_{cm} + E_{ov} + E_{endo} \tag{2}$$

E_{cm} is the center-of-mass collision energy between Na^+ and C_{60}; E_{ov} is the average internal energy of a canonical ensemble of C_{60} that emerges from the Knudsen cell kept at temperature T_{ov}. E_{endo}, the adiabatic complexation energy of $Na^+ + C_{60}$, has been calculated by a variety of different ab-initio methods [11]. The value of 1 eV that we adopt in this study agrees with published values within about ± 0.5 eV.

The experimental breakdown curves are simulated as a product of the cross section for collisional formation of $Na@C_{60}^+$, and the probability that this ion will not undergo unimolecular dissociation within a time window $t \le t_{max}$ which is determined by experimental parameters. Our data suggest that the formation cross section $\sigma(E_{cm})$ increases linearly above some threshold energy E_{thresh}, in agreement with the results of molecular dynamics simulations for $Li^+ + C_{60}$ collisions [12]. We have fitted a large number of spectra and consistently obtained E_{thresh} = 29.6 eV (in the center-of-mass system). Hence, the following relation is used to model the observed yield of adduct ions,

$$I_{NaC60} = \sigma_o \cdot (E_{cm} - E_{thresh}) \cdot \exp(-kt_{max}) \tag{3}$$

We incorporate the following features into this model: 1) E_{cm} and E_{ov} are described by distributions; their combined width is obtained by a fit to the data. 2) E^* and $k(T(E^*))$ are time dependent because radiation will gradually cool the adduct ion; this will shift the breakdown curve to higher collision energies. We describe radiative energy loss by the expression [13] $k_{rad} = 4.5\cdot10^{-17} T^6$ eV/s with T in Kelvin.

Results and Discussion:

Fig. 2 displays the yield of adduct ions, Na@C_{60}^+, measured for three different C_{60} source temperatures. The dashed line represents a fit to the data obtained for a source temperature of 570 °C. It invokes four parameters: The combined width of the energy distributions, the dissociation energy E_a, the formation threshold E_{thresh}, and the initial slope σ_o.

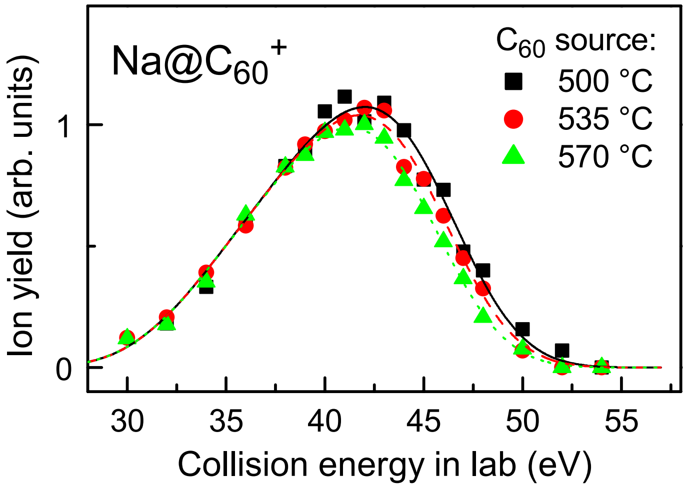

Fig. 2 Full dots: Dependence of the yield of Na@C_{60}^+ on collision energy for three different C_{60} source temperatures. Lines: Fit to data taking into account radiative cooling and distribution of excitation energies. Data are normalized to exhibit same rising slopes.

Data for the other source temperatures were fitted similarly, but the values of E_a and E_{thresh} were adopted from the previous fit. The observed shift in the breakdown energy is accounted for by varying the initial thermal energy of C_{60}, see Eq. 2. The results of the data analysis may be summarized as follows:

- The model provides an excellent fit to the yield of Na@C_{60}^+.
- The insertion threshold E_{thresh} in the center-of-mass system amounts to 29.6 eV (estimated statistical error 1.0 eV). This value is some 10 eV higher than the value reported by Anderson and coworker [4]. Presumably, their lower energy resolution resulted in much broader yield curves, and in an underestimate of the insertion threshold.
- The dissociation energy of Na@C_{60}^+ with respect to C_2 loss is $E_a = 10.17 \pm 0.02$ eV (statistical uncertainty). It is strikingly close to the average dissociation energy of C_{60}^+, 10.0 ± 0.2 eV (*rms* standard error) that was recently derived from a comprehensive analysis of all experimental data published during the past decade, under the assumption that $\nu_o = 5\times10^{19}$ s^{-1} [9], and to the value of 10.2 eV that Boese and Scuseria obtained from a density functional study of C_{60}^+ [14].
- The breakdown energy of Na@C_{60}^+ (50 % survival probability for a time interval of 10 µs, computed from $k(E^*)$) is $E^* = 49.1 \pm 0.5$ eV; its dissociation rate is $k = 94\,000$ s^{-1} (E^* and k are the values immediately after collision; radiative cooling will reduce them over the experimental time interval of 10 µs).
- The abruptness of the breakdown graph provides a lower limit to ν_o. As can be seen from eq. 1, the lower the activation energy, the more gradually the rate will increase with T, and E^*. If we assume a pre-exponential less than 2×10^{14} s^{-1} and a correspondingly small activation energy to match the breakdown energy, then the experimental data cannot be fitted unless we assume an energy spread less than the lower bound that one can compute from Eq. 2.
- The shift in the breakdown energies that is apparent from Fig. 2 provides us with a novel method to determine the heat capacity of C_{60}. (The temperature dependence of the appearance energy of C_{58}^+, formed from C_{60} by electron impact ionization, presents a closely related method, but the accuracy of those data appears to be inferior [15]). Fig. 3

shows how the thermal energy of C_{60} (E_{ov} in Eq. 2) that one needs to assume in order to fit the data at 500 and 535 °C decreases with decreasing T_{ov}. The slope of the straight line that we fitted to our data yields the vibrational heat capacity of C_{60}, $\Delta E/\Delta T = 12.6 \pm 1.4$ meV/°C. For comparison, the equipartition theorem predicts a value of 15.0 meV/°C.

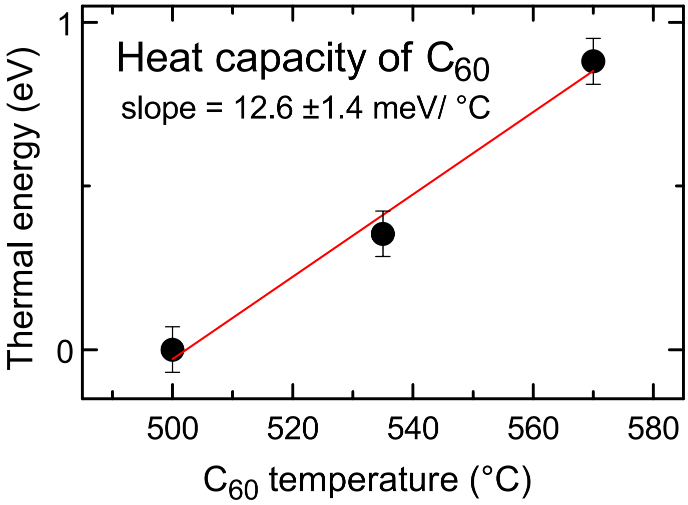

Fig. 3. Full dots: thermal energies of C_{60} relative to that at 500 °C, extracted from the shift in breakdown energies (cf. Fig. 2). Solid line: least-squares fit of a straight line. Its slope, $\Delta E/\Delta T$ = 1.26 ± 1.4 meV/°C, measures the heat capacity of C_{60}.

Acknowledgement:

This material is based upon work supported by the National Science Foundation under Grant No. 9507959.

References

[1] E.E.B. Campbell, R.Tellgmann, N.Krawez, I.V.Hertel, J.Phys.Chem.Solids 58 (1997) 1763.
[2] A. Weidinger, M. Waiblinger, B. Pietzak, T. A. Murphy, Appl. Phys. A 66 (1998) 287.
[3] R. Deng, R. MacCrimmon, O. Echt, in *Cluster and Nanostructure Interfaces*, edited by P. Jena, S. N. Khanna, B. K. Rao (World Scientific, Singapore, 2000), p. 437 .
[4] Z. Wan, J. F. Christian, Y. Basir, S. L. Anderson, J. Chem. Phys. 99 (1993) 5858.
[5] Y. J. Basir, S. L. Anderson, Int. J. Mass Spectrom. 187 (1999) 603.
[6] G. D. Alton, in *Experimental Methods in the Physical Sciences*, edited by F. B. Dunning, R. G. Hulet (Academic Press, San Diego, 1995), Vol. 29A, p. 69.
[7] R. Deng, O. Echt, Chem. Phys. Lett. in print (2001).
[8] S. Matt, R. Parajuli, A. Stamatovic, P. Scheier, T. D. Märk, J. Laskin, C. Lifshitz, Eur. Mass Spectrom. 5 (1999) 477.
[9] S. Matt, O. Echt, P. Scheier, T. D. Märk, Chem. Phys. Lett. 348 (2001) 194.
[10] C. E. Klots, Z. Phys. D 20 (1991) 105.
[11] J. Cioslowski, *Electronic Structure Calculations on Fullerenes and Their Derivations* (Oxford University Press, Oxford, 1995).
[12] V. Bernshtein, I. Oref, J. Chem. Phys. 109 (1998) 9811.
[13] S. Tomita, J. U. Andersen, C. Gottrup, P. Hvelplund, U. V. Pedersen, Phys. Rev. Lett. 87 (2001) 073401.
[14] A. D. Boese, G. E. Scuseria, Chem. Phys. Lett. 294 (1998) 233.
[15] C. Lifshitz, Int. J. Mass Spectrom. 198 (2000) 1.

Dynamics of Highly Excited Fullerenes

E.E.B. Campbell

Dept. of Experimental Physics, School of Physics and Engineering Physics, Göteborg University and Chalmers, SE-41296 Göteborg, Sweden.

Fullerenes are very interesting and fruitful model systems for investigating the dynamics of complex molecular systems with a large number of degrees of freedom. In this talk I will discuss two different manifestations of the dynamics of highly excited fullerenes. In the first example the molecular fusion reaction of two colliding fullerenes will be discussed. In earlier work the fusion reaction was described in the context of simple two-body models such as the absorbing sphere model (otherwise known as line-of-centres model) as applied to nuclear physics collisions [1]. The experimental results differed from the simple models in three important aspects as illustrated in Figure 1: the form of the cross section close to threshold, the absolute magnitude and the very rapid decrease of the cross section to higher energies. Here I will discuss these models and provide some explanations for the different behaviour observed experimentally [2]. The fragmentation behaviour of the highly excited fusion product (mass and angular distributions of the fragments as a function of collision energy) will also be discussed in the context of simple statistical models [2,3].

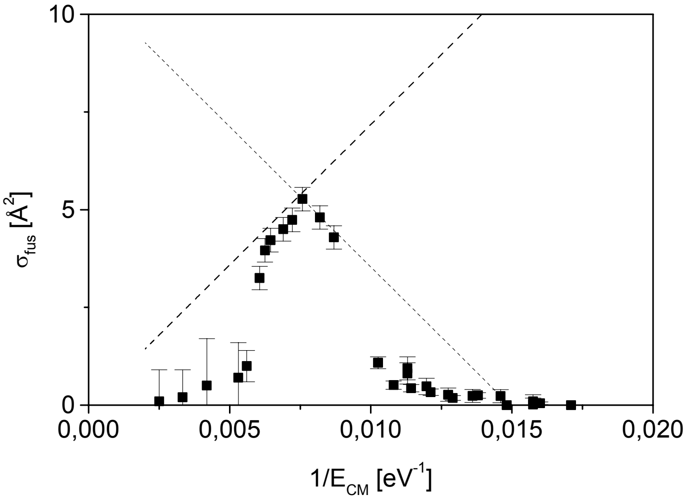

Fig. 1. Cross section for the fusion reaction in C_{60}^{+} + C_{60} collisions. Squares: experimental data, Dashed line: line-of-centres model multiplied by 0.07 with centrifugal cut-off at high energies.

Another very interesting property of C_{60} is its tendency to undergo delayed (μs) ionisation after excitation with ns laser pulses. This is generally described in terms of a statistical thermal electron emission, akin to thermionic emission from bulk metals [4]. The delayed ionisation occurs due to the strong coupling of electronic to vibrational degrees of freedom during the timescale of the laser pulse leading to a strong vibrational heating to temperatures on the order of 3000-4000 K. Since the activation energy for the lowest energy fragmentation process (C_2 emission) is higher than the ionisation potential in fullerenes, delayed ionisation is an observable reaction channel, in competition with neutral fragmentation. This work explores the ionisation behaviour when the excitation time scale is reduced below the time scale for electron-phonon coupling [5]. Three distinct ionisation mechanisms are observed for different excitation timescales as illustrated in Figure 2. For the shortest laser pulses (25 fs), the ionisation is a direct multiphoton ionisation for intensities up to ca. 10^{14} Wcm^{-2} where

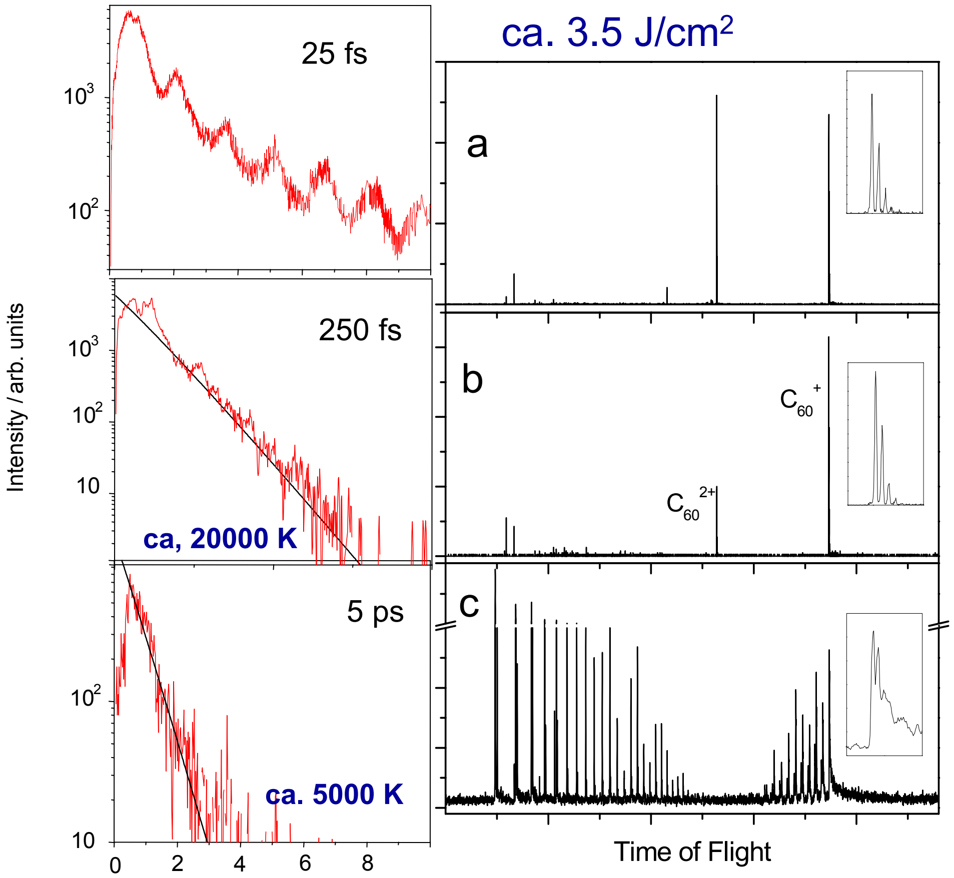

Fig. 2. PES (left) and ToF mass spectra (right) produced from photoionisation with laser pulses of different pulse duration but the same fluence (3.5 J/cm^2). (a) 25 fs pulses, direct above threshold ionisation (b) 200 fs pulses, thermal electron emission from vibrationally cold fullerenes (c) 5 ps pulses, thermal electron emission from vibrationally hot fullerenes. Adapted from [5]

tunnel ionisation onsets. This is seen most clearly in the photoelectron spectra where clear above threshold ionisation (ATI) peaks are seen for intensities below this value. As the laser pulse duration is increased beyond 75 fs, keeping the fluence constant, the ATI becomes less important and is dominated by a thermal electron energy distribution corresponding to high electron temperatures (on the order of 30000 K). This is interpreted as being due to a statistical electron emission after the electronic excitation energy has been distributed among the electronic degrees of freedom in the molecule. The mass spectra are still characterised by strong multiple charging and sharp mass peaks (indicating prompt ionisation on the ns timescale). The third ionisation mechanism is observed for laser pulses longer than 500 fs. The thermal electron temperature drops dramatically for laser pulses of the same fluence. In addition, no multiply charged ions can be seen in the mass spectra and the C_{60}^{+} parent ion peak develops a long "tail" extending to longer flight times. Such a tail is characteristic of delayed (µs) ionisation. This therefore marks the cross-over to a thermionic-like ionisation after the electronic excitation energy has coupled to the vibrational degrees of freedom [6]. In addition to the above threshold ionisation and the statistical electron emission there is reproducible structure superimposed on the dominant photoelectron peak at electron kinetic energies up to 1.5 eV. This is shown in Figure 3 and has been shown to be Rydberg series of the fullerene produced and ionised with the absorption of one additional photon within the same laser pulse [7]. This is the first time that resolved Rydberg series of C_{60} have been measured. The difficulty of obtaining resolved electronic spectra of gas-phase C_{60} is due to the difficulty of vibrationally cooling molecular beams of C_{60}. In the fs-laser experiments it is the relatively high vibrational excitation of the fullerenes leaving the oven that allow the

Rydberg series to be populated and resolved in the photoelectron spectra. It is the decay of these excited Rydberg states on the 100 fs time scale that leads to the rapid thermalisation of the electronic energy and statistical emission of hot electrons prior to coupling to the vibrational degrees of freedom.

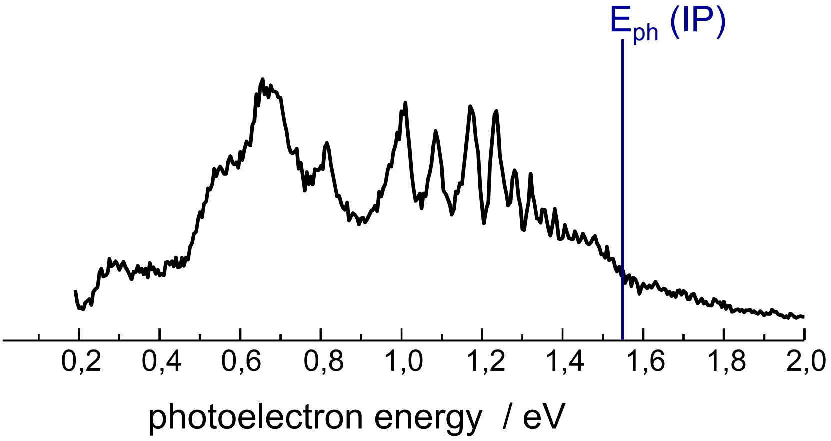

Fig. 3. Photoelectron spectrum from C_{60} using low intensity 1.5 ps laser pulses (800 nm). The structure corresponds to the excitation and one-photon ionisation of three excited Rydberg series in the molecule.

Acknowledgements

I would like to thank my collaborators. I.V. Hertel and R.D. Levine as well as all the students involved in the research discussed here. Financial support from the EU (IHP Network "Delayed Ionisation and Competing Cooling Mechanisms in Atomic Clusters"), VR and the Göran Gustafsson Foundation for Natural Sciences is gratefully acknowledged.

References

---

[1] F. Rohmund, A. Glotov, K. Hansen, E.E.B. Campbell, *J. Phys. B* **29** (1996) 5143

[2] E.E.B. Campbell, A.V. Glotov, A. Lassesson. R.D. Levine, Proc. Of French Academy of Science, Special Issue on Clusters, ed. Brechignac and Cahuzac, in press

[3] A. Glotov, E.E.B. Campbell, *Phys. Rev. A* **62** (2000) 033202

[4] E.E.B. Campbell, R.D. Levine, *Ann. Rev. Phys. Chem.* **51** (2000) 65

[5] E.E.B. Campbell, K. Hansen, K. Hoffmann, G. Korn, M. Tchaplyguine, M. Wittmann, I.V. Hertel, *Phys. Rev. Lett.* **84** (2000) 2128

[6] E.E.B. Campbell, K. Hoffmann, I.V. Hertel, *Eur. Phys. J. D* **16** (2001) 345

[7] M. Boyle, K. Hoffmann, C.P. Schulz, I.V. Hertel, R.D. Levine, E.E.B. Campbell, *Phys. Rev. Lett.* **87** (2001) 273401

Time-Resolved Photodissociation (TRPD) of Biomolecule Ions in the Gas Phase

Chava Lifshitz

Department of Physical Chemistry and The Farkas Center for Light Induced Processes,
The Hebrew University of Jerusalem, Jerusalem 91904, Israel

The development of mass spectrometry of biomolecules has raised again some old questions. For example, does intramolecular vibrational redistribution (IVR) precede fragmentation in very large proteins, having an extremely large number of degrees of freedom? Does electronic energy relaxation take place or is there site selectivity and charge directed reactivity[1]? We have taken upon ourselves the study of the extent of statistical versus site selective fragmentation of small peptide radical cations. The objective is to find out to what degree does the mode of preparation of the ions and the initial site of excitation affect the type, degree and rate of fragmentation. It has recently been suggested theoretically that the charge acts as a scout to find the preferred fragmentation site and IVR does not necessarily precede fragmentation. This contradicts the general wisdom in mass spectral statistical theories such as RRKM/QET and has far reaching implications concerning the fragmentation of large bio-molecules that are now the central topic of analytical research in mass spectrometry. The theoretical effort coincided with some very nice experiments done on small peptides having a chromophore through which laser MPI and photodissociation (PD) proceed[2]. Fragmentation of these peptides has been observed as a direct outcome of the initial ionization and excitation at a specific site, followed by intramolecular charge transfer.

A new instrument has been constructed by us whose purpose is to study time-resolved photodissociation (TRPD) of small peptide ions. Laser desorption of neutral peptides and entrainment in a supersonic expansion is combined with laser photoionization in an ion trap followed by thermalization, laser photodissociation and time of flight mass analysis. Ionization and excitation take place through an aromatic chromophore at the C-terminus of the peptide whereas dissociation produces the immonium ion at the N-terminus. The long-range purpose is to uncover the role of IVR in unimolecular fragmentations of peptide radical cations. One avenue is the determination of microcanonical rate constants at a well-defined internal energy E for a series of peptides possessing the same chromophore, undergoing the same fragmentation but having a variable number of degrees of freedom. This paper demonstrates the feasibility of the method and provides the first attempts at rate measurements for the peptide leucyl tyrosine (LeuTyr).

The experimental apparatus is shown schematically in Figure 1. It consists of three vacuum chambers, for laser desorption, for the quadrupole ion trap and for a reflectron time-of-flight (TOF) analyzer, respectively. The latter two parts have been employed by us and have been described in detail in the past[3]. The reflectron TOF mass spectrometer with a quadrupole ion trap as an ion source has been developed for the observation of unimolecular decay of energy selected ions on the ms time scale combined with a fast mass detection process.

The first chamber is constructed on axis with the other two. Laser desorption (LD) followed by jet cooling is carried out in this chamber. LD of peptides is performed by the 1064 nm fundamental output of a Nd:YAG laser which is focused loosely to a spot of the order of 1.5 mm diameter within 4 mm in front of the nozzle (0.5 mm diameter) of a pulsed supersonic valve. A graphite rod is used as a substrate covered evenly with the peptide sample. The desorbed neutrals are entrained and cooled by collisions with CO_2 or Ar gas through the nozzle. The neutral molecules are introduced into the second chamber downstream, through a 3 mm diameter skimmer.

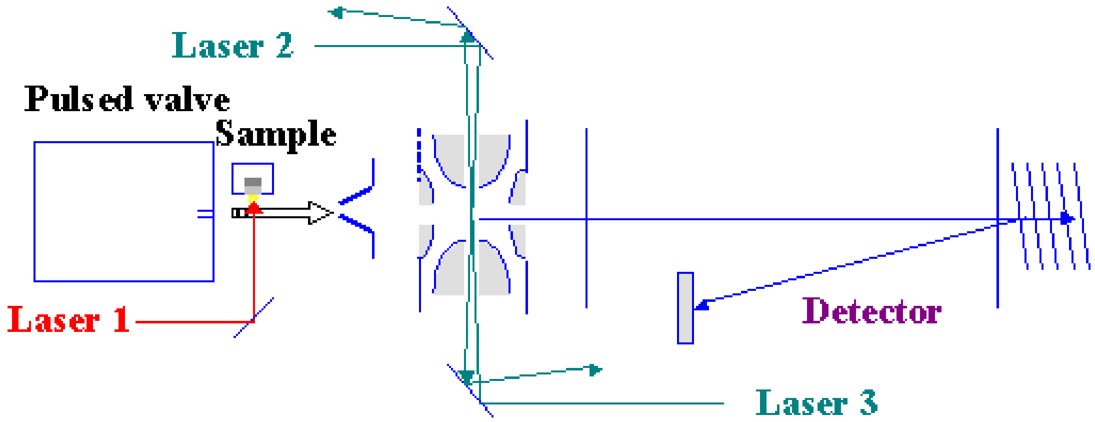

Figure 1

Photoionization and photodissociation take place in the second chamber where a quadrupole ion trap is used as the ion source. There are six 3.5 mm diameter apertures. Two apertures are in the two endcaps, one of which is used as the inlet of the laser desorbed neutral sample and the other for ion ejection. Four are in the ring electrode with two at the top and bottom (vertical direction), and the other two in the horizontal direction for the laser beams. About 1 cm above the top aperture is the nozzle of a General Valve pulsed valve that can provide pulsed helium buffer gas. During operation, the RF voltage is applied to the ring electrode while both endcaps are held at 0 V. The RF field serves to trap ions present within the volume of the trap until they are ejected by application of a DC extraction pulse to the exit endcap. During extraction, the RF voltage is off.

Cold intact neutral molecules undergo two-photon ionization by either one of the following methods: The frequency-doubled output of a dye laser (ND6000, 275–290 nm, 0.3–0.8 mJ/pulse) pumped by a Nd: YAG laser (Surelite from Continuum), or alternatively the 266 nm fourth harmonic of a Nd-YAG laser (Minilite from NewWave, 1.3 mJ/pulse). In one-color experiments, the photon employed for photodissociation has the same wavelength as is used for the two-photon ionization. Photodissociation is achieved in two-color experiments by absorption in the visible wavelength region (530–580 nm, 2–2.4 mJ/pulse). Both the photoionizing- as well as the photodissociating-laser are aligned to pass through the center of the ion trap, but from opposite directions. Two digital delay/pulse generators control all events. Laser desorption takes place after the opening of the nozzle of the pulsed valve. The desorbed neutrals are transported into the ion trap where they are photoionized. The pulse to the ionization laser is synchronized with the RF pulse. The storage time of the ions is controlled by another output of the pulse generator by triggering the extraction pulser that serves the dual purposes of ejecting the ions and providing the start-time reference of the TOF mass analysis. Ionization can produce the parent ions in a variety of excited states. It can also lead to prompt fragmentations. In two-color TRPD, the ionization and excitation steps are separated in time so that the parent ions can undergo radiative and collisional thermalization to lose their excess internal energy acquired in the ionization step. In some of the experiments we are applying two additional pulses between the ionization and excitation laser pulses. Pulsed helium buffer gas is provided for the dual purpose of bringing the ions into the center of the trap and for enhancing collisional thermalization. This event is triggered by the second digital delay/pulse generator that is triggered by the Q-switch output of the ionization laser, which makes sure the nozzle opens after the ionization event. The bulk of the helium gas has to be pumped out by the time the excitation laser leading to photodissociation is turned on to ensure that the photoexcited ions undergo no further relaxing collisions. A second pulse serves to eject any prompt fragments that are formed. This is achieved by temporarily increasing the amplitude of the RF voltage that is applied to the ring electrode.

Following thermalization the photoexcitation laser is fired to excite the thermalized ions to well defined internal energies. This is followed by measurements of the fragment ion buildup as a function of the trapping delay time leading to the TRPD curve. Each time point along the TRPD curve is the result of 500 laser shots. Time dependent daughter ion intensities are normalized via the corresponding parent ion intensities, taking the parent intensity at the shortest trapping time as the reference point, in order to take into account fluctuations in light intensity for different laser shots.

The dissociation kinetics of the photoexcited peptide ions can be deduced by fitting the measured buildup curve of their fragment ions. The one color photoionization and time-resolved photodissociation spectrum for LeuTyr obtained at 266 nm is presented in Figure 2. The experimental results can be fitted with an exponential rise of the normalized yield of the immonium daughter ion with a rate constant k = $(1.3\pm0.3)\times10^3$ sec^{-1}. There is a large non-zero intercept of the daughter ion yield at zero trapping time. This is ascribed to a higher-order, faster multiphoton process than the one depicted by the time dependence on the millisecond time scale. It is plausible that some, or all of the intercept at zero trapping time is due to a three photon process and that the time-dependence observed in the millisecond range is due to the least internally excited ions in the distribution. These are the ions formed by two-photon ionization and excitation just slightly above the dissociation threshold.

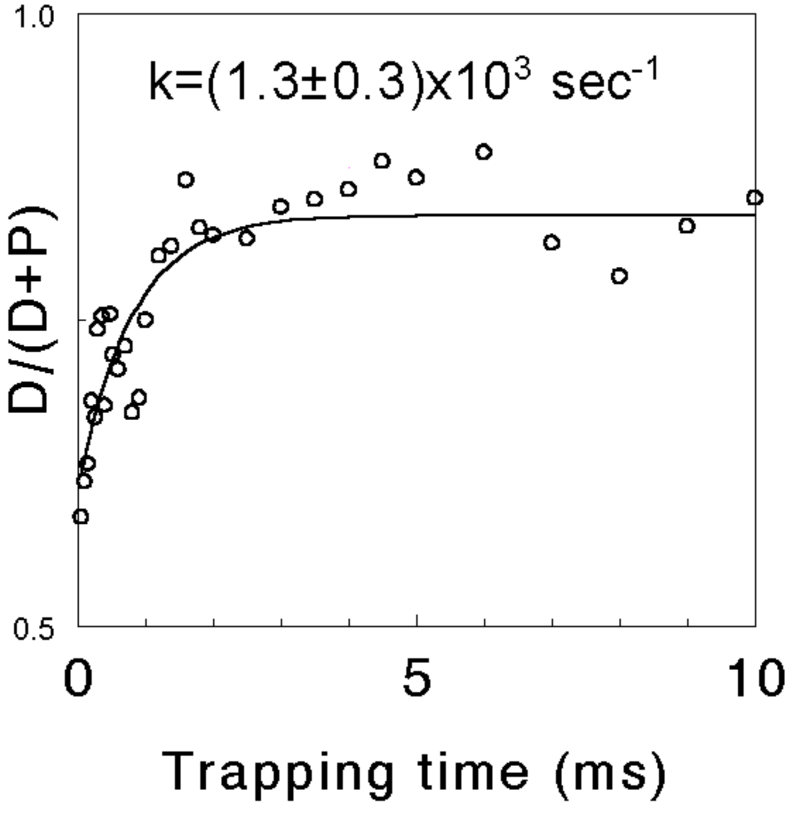

Figure 2

References

---

[1] F. Remacle, R.D. Levine, M.A. Ratner: Chem. Phys. Lett., **285**, 25 (1998).

[2] R. Weinkauf, P. Schanen, D. Yang, S. Soukara, E. W. Schlag: J. Phys. Chem., **99**, 11255 (1995).

[3] W. Cui, B. Hadas, B. Cao, C. Lifshitz: J. Phys. Chem. A **104**, 6339 (2000); 7160 (2000)

Sensitizing Biomolecules to Secondary Electron Damage

Sascha Gohlke, Frank Brüning, Hassan Abdoul-Carime[a], Andrzej Rosa, Michael A. Huels[a], Léon Sanche[a], and Eugen Illenberger

Institut für Chemie - Physikalische und Theoretische Chemie, Freie Universität Berlin
Takustrasse 3, D-14197 Berlin, email: iln@chemie. fu-berlin.de

The genotoxic effects of ionizing radiation in living cells are *not* produced by the mere direct impact of the primary high energy quanta (ß-, X- or γ-rays). Instead, these effects are induced by secondary reactive species which are formed along the ionization track. Among these secondary species, which also include neutral radicals, and positive and negative ions, non-thermal ballistic secondary electrons are created abundantly ($\approx 5\text{x}10^4$ per MeV deposited), the majority of which possess initial kinetic energies between below ≈ 20 eV [11]. In the course of successive inelastic collisions within the medium these electrons are thermalized before they enter some stage of solvation as chemically rather inactive species.

In an extended effort to reveal the molecular mechanisms of electron induced damage in biological material (e. g. single and double strand breaks in DNA [1]) we have investigated the components of large biomolecules (DNA bases and simple aminoacids [2-4]) in the gas phase in order to get information on the *intrinsic* behaviour of these compounts with respect to low energy electron interaction. This is done in a crossed molecular beam/electron beam arrangement where the gas phase molecules interact with an electron beam of well defined energy and a mass spectrometric detection of the negatively charged products. Our results indicate the elementary reactions by which these compounds are degraded at low energies with the most prominent one identified as resonant electron capture and subsequent dissociation.

A further point concerns the molecular mechanisms of radio sensitizers (e.g. 5-bromouracil (BrU)) which are used in cancer therapy. Our results demonstrate that reactive uracil radicals (U) can very effective be generated via dissociative electron attachmernt at energies below 1 eV. This reaction is hence considered as the essentiell mechanism by which this sensitizer operates.

Work supported by Deutsche Forschungsgemeinschaft (DFG), Medical Research Councel (MRC) and National Cancer Institute (NCI) of Canada.

References

---

[1] B. Boudaïffa, P. Cloutier, D. Hunting, M. A. Huels and L. Sanche, *Science* **287** (2000) 1658.

[2] S. Gohlke, F. Brüning, A. Rosa, M. A. Huels and E. Illenberger, *Phys. Chem. Chem. Phys.* (PCCP) (submitted).

[3] H. Abdoul-Carime, M. A. Huels, L. Sanche and E. Illenberger, *J. Am. Chem. Soc.* **123** (2001) 53254.

[4] H. Abdoul-Carime, M. A. Huels, L. Sanche, F. Brüning and E. Illenberger, *J. Chem. Phys.* **113** (2000) 2517.

[a] *Faculté de Médecine, Université de Sherbrooke, Sherbrooke, Québec J1 H 5N4, Canada*

Stark Mixing in Rydberg Atoms by ultralow energy collisions with ions

M. R. Flannery and D. Vrinceanu

School of Physics, Georgia Institute of Technology, Atlanta, Georgia 30332

The theory of Collisional Stark Mixing in Rydberg atoms is presented in the classical and quantal formulations. Quantal and classical probabilities are derived for $n\ell \rightarrow n\ell'$, transitions in a Rydberg system induced by the time dependent (dipole) electric field generated by adiabatic collision with charged particles. A universal classical scaling law permits examination of the (rapid) convergence of the quantal results onto the classical background as n is increased. Comparison is made with measurements of the fractional populations.

I. STARK MIXING

The ion-Rydberg atom/molecule collisional process

$$A^{Z+} + Ry(n,\ell) \rightarrow Ry(n,\ell') + A^{Z+} \tag{1}$$

is called collisional Stark mixing since the ℓ-changing transitions $\ell \rightarrow \ell'$ occur within the same energy shell n of the Rydberg species and are induced by the time-dependent electric field generated by the passing ion A^{Z+}. The process is significant over a broad range of interest and applications. For example, the formation of anti-hydrogen by three-body recombination $e^+ + \bar{p} + e^+ \rightarrow \bar{H} + e^+$ at ultralow energies, where the sequence [1] is collisional capture into high $\ell \rightarrow$ states, followed by Stark mixing collisions $n\ell \rightarrow n\ell'$ and by Radiative relaxation. Since the n-changing collisions are relatively unimportant at ultralow energies, the ℓ-mixing collisions are essential in producing the low angular momentum states required to radiatively decay at relatively high rate to low n-levels, thereby stabilizing the recombination. In $ZEKE$ (Zero Kinetic Energy) Spectroscopy [2] where high ℓ states are produced from low ℓ states by electric fields. It is also significant in dissociative recombination [3–5]. Large cross sections for ℓ-mixing in slow ion- Na collisions have been measured [6].

The process is also interesting from a theoretical point of view and has remained largely unsolved for four decades. Notable historical landmarks include a modified first-order impact parameter treatment [7], a classical diffusion theory [8], hydrogen atom in weak E-B fields [9], a truncated closely-coupled channel system of equations [10], Monte-Carlo simulations [11]), and quantal and classical treatments of $0 \rightarrow \ell'$ transitions [12–15]. The rich dynamical symmetry of the hydrogen atom provides the key which enables both (exact) classical [17,18] and quantal solutions [18–20] to be developed here in a unified way.

II. GROUP SYMMETRY

In addition to the unperturbed Hamiltonian

$$H_0 = \frac{p^2}{2m_e} - \frac{e^2}{r} \ ,$$

the angular momentum $\mathbf{L} = \mathbf{r} \times \mathbf{p}$ and the classical Runge-Lenz vector

$$\mathbf{A} = p_n^{-1}\left[\mathbf{p} \times \mathbf{L} - m_e e^2 \frac{\mathbf{r}}{r}\right] \ ,$$

directed toward the pericenter and normalized to angular momentum units, are all conserved. The operator $\mathbf{A}$ has the symmetrized (Pauli-Lenz) quantal form

$$\mathbf{A} = \left[\frac{1}{2}(\mathbf{p} \times \mathbf{L} - \mathbf{L} \times \mathbf{p}) - m_e e^2 \hat{r}\right] / p_n$$

and the following properties:

$$\begin{array}{rll}
[A_j, H] = & 0 & \text{It is a conserved quantity,} \\
[L_j, A_k] = & i\hbar\ \epsilon_{jkn} A_n & \text{It is also a system vector,} \\
[A_j, A_k] = & i\hbar\ \epsilon_{jkn} L_n & \text{Its components do not commute,} \\
\mathbf{A} \cdot \mathbf{L} = & \mathbf{L} \cdot \mathbf{A} = 0 & \text{The vector } \mathbf{A} \text{ is orthogonal on } \mathbf{L}, \\
A^2 + L^2 = & (n^2 - 1)\hbar^2 & \text{Is constant for intrashell transitions,}
\end{array}$$

where ϵ_{kjn} is the Levi-Civita antisymmetric symbol for any $k, j = 1, 2, 3$. These commutation relations define the $SO(4)$ dynamic symmetry group for the restricted motion of the orbital electron to the energy shell. The $SO(4)$ operators can be disentangled by introducing $\mathbf{M} = (\mathbf{L} + \mathbf{A})/2$ and $\mathbf{M} = (\mathbf{L} - \mathbf{A})/2$. Each $\mathbf{M}$ and $\mathbf{N}$ operator separately generates a $SO(3)$ subalgebra, such that $SO(4) \equiv SO(3) \oplus SO(3)$. The classical analogy is that the set of coupled equations for $\mathbf{L}$ and $\mathbf{A}$ are decomposed into an uncoupled set for $\mathbf{M}$ and $\mathbf{N}$, which then evolve independently with time. In classical mechanics, the operators $\mathbf{L}$ and $\mathbf{A}$ are replaced by their classical vectors and the commutators $(i\hbar)^{-1}[...]$ by the corresponding Poisson brackets.

III. COLLISION INTERACTION

The vectors $\mathbf{L}$ and $\mathbf{A}$ precess about the direction of the electric field $\vec{\mathcal{E}}$ with Stark frequency $\omega_S = \frac{3}{2}\, a_n v_n (\mathcal{E}/e)$. The frequencies of the Rydberg electron and the collision are $\omega_n = v_n/a_n$ and $\omega_R = \dot{\Phi}$, respectively. Here $a_n = n^2 a_0$ and $v_n = v_0/n$ are the averaged orbital radius and velocity. Simulation of the collision will show that the frequencies are ordered as $\omega_S < \omega_R < \omega_n$. It will also show that although $\mathbf{L}$ and $\mathbf{A}$ change little during one orbit, significant change is accomplished during the collision over the course of many ($\sim$50) electron orbits. It also indicates that the ℓ-changing collision at ultralow impact energies satisfies the following three approximations:

- **Weak field**: Here the Stark energy splitting $\hbar\omega_S \ll \hbar\omega_n$, the separation between neighboring energy levels. The collision then occurs at large impact parameters b where the ion-Rydberg atom interaction potential is the ion-dipole potential,

  $$V(\mathbf{r}, \mathbf{R}) = -\mathbf{d} \cdot \vec{\mathcal{E}} = -Ze^2 \frac{\hat{\mathbf{R}} \cdot \mathbf{r}}{R^2}$$

  where $\mathbf{d} = -e\mathbf{r}$ is the dipole. The weak field region is then $b \gg (3Z/2)^{1/2} a_n$.

- **Orbital adiabatic**: In this region $b > (v/v_n)a_n$, the collision frequency $\omega_R = \dot{\Phi} \ll \omega_n$, the orbital frequency of the Rydberg electron. In classical treatments, the electron position vector $\mathbf{r}$ can then be replaced by its average $\langle \mathbf{r} \rangle$. In quantal treatments, then

  $$\langle n\ell' m' | \mathbf{r} | n\ell m \rangle = -\frac{3}{2p_n} \langle n\ell' m' | \mathbf{A} | n\ell m \rangle \qquad (2)$$

  for matrix elements within the same energy shell. This is Pauli's replacement rule [16].

- **Classical path**: The angular momentum of relative motion $-\mu R^2 \dot{\Phi}$ of the collision system of reduced mass μ is $\gg \ell\hbar$, the angular momentum of the Rydberg electron. It is therefore conserved with value $\mu b v$ so that the interaction potential is

  $$V(\mathbf{r}, \Phi) = \frac{Ze^2}{vb} \frac{d\Phi}{dt} \hat{\mathbf{R}} \cdot \mathbf{r} = \frac{Ze^2}{vb} \frac{d\Phi}{dt} (y \sin\Phi + z \cos\Phi)$$

  Under the above three approximations, the interaction is

  $$V(\mathbf{r}, \alpha) = -\alpha \frac{d\Phi}{dt} (A_2 \sin\Phi + A_3 \cos\Phi) \qquad (3)$$

where the dimensionless Stark parameter is

$$\alpha = \frac{\omega_S}{\omega_R} = \frac{3Z}{2} \left(\frac{a_n v_n}{bv} \right) = \frac{3Z}{2} \left(\frac{a_n}{b} \right)^2 \left(\frac{\tau_{coll}}{\tau_0} \right) \qquad (4)$$

where $\tau_{coll} = b/v$ is a measure of the collision duration and $\tau_0 = a_0/v_0$ is the au of time. Equation (3) has the advantage that it is expressed only in terms of the generators of the $SO(4)$ group. Moreover, the components $\{L_1, A_2, A_3\}$ generate a subgroup of the original symmetry group. Under the above three approximations, the resulting set of quantal and classical equations governing the problem of collisional Stark Mixing at ultralow energies can be solved exactly in terms of *collision* parameter χ defined by $\cos\chi = [1 + \alpha^2 \cos\Delta\Phi \sqrt{1 + \alpha^2}]/(1 + \alpha^2)$ where $\Delta\Phi$ is the polar angle swept out by the internuclear vector $\mathbf{R}$ during the collision time τ_{coll}.

IV. RESULTS

Exact solutions [17–20] of Stark Mixing in atomic hydrogen induced by the time-dependent (dipole) electric field generated by (adiabatic) collision with a slow ion will be presented in both classical and quantal formulations. Movies of the process will be shown The exceptionally rich dynamical symmetry of the hydrogen atom provides the key foundation which enables both the classical [17,18] and quantal solutions [18–20] to be constructed in a unified way, by using group representation theory. Fig.1 demonstrates the rapid convergence of the quantal results onto the classical frame as n is increased. The structure will be explained in terms of two distinct regions within the classical accessible region, and two classical inaccessible regions. It remains obscured within the quantal results.

V. SUMMARY OF MAIN POINTS

- Case study of Collisional Stark Mixing for the full transition array $n\ell \to n\ell'$ will be presented.
- The inherent Group Dynamic Symmetry permits our present development of exact solution in both quantal and classical formulations.
- Collisional Stark Mixing at ultralow energies is probably one of the last remaining problems in collision physics capable of an exact analytical solution.
- Our solutions are presented in compact form reflecting the mathematical beauty of the problem as well as pragmatic value.
- Classical results complement Quantal results.
- Quantal-Classical Correspondance and Convergence will be exhibited.
- A modified theory which can account for Quantum Defects (low ℓ) in non-hydrogenic systems will be proposed.
- Essential agreement is obtained with measurements [6] for $Na(28d) \to Na(28f), Na(28f+28g), Na(28f+28g+28h)$ transitions.

ACKNOWLEDGMENTS

This research has been supported by AFOSR Grant No. 49620-99-1-0277 and NSF Grant No. 01-00890.

---

[1] M. R. Flannery and D. Vrinceanu, in *Atomic processes in Plasmas: 11th APS Topical Conference*, edited by E. Oks and M. S. Pindzola (AIP Press, New York, 1998), p. 317.
[2] F. Merkt and R. N. Zare, J. Phys. Chem. **101**, 3495 (1994).
[3] S. R. Lundeen, in *Dissociative recombination: theory, experiment, and applications.*, edited by J. B. A. Michell and S. L. Guberman (World Scientific, Singapore, 1989), pp. 182–192.
[4] R. J. T. Gougousi and M. F. Golde, Int. J. Mass. Spectrom. Ion Processes **149/150**, 131 (1995).
[5] M. R. Flannery and D. Vrinceanu, edited by S. L. Guberman (PUBLISHER, Singapore, YEAR), p. in press.
[6] X. Sun and K. B. MacAdam, Phys. Rev. A **47**, 3913 (1993).
[7] R. M. Pengelly and M. J. Seaton, Monthly Notices Roy. Astronom. Soc. **127**, 165 (1964).
[8] I. C. Percival and D. Richards, J. Phys. B **12**, 2051 (1979).
[9] Y. N. Demkov, B. S. Monozon, and V. N. Ostrovskiĭ, Sov. Phys. JETP **30**, 775 (1970).
[10] I. L. Beigman and V. S. Lebedev, Phys. Rep. **250**, 95 (1995).
[11] P. Bellomo, D. Farrelly, and T. Uzer, J. Chem. Phys **107**, 2499 (1995).
[12] A. K. Kazanski and V. N. Ostrovski, Phys. Rev. A **53**, R1811 (1995).
[13] A. K. Kazansky and V. N. Ostrovsky, J. Phys. B **29**, 3651 (1996).
[14] A. K. Kazansky and V. N. Ostrovsky, Phys. Rev. Lett **77**, 3094 (1996).
[15] A. K. Kazansky and V. N. Ostrovsky, Sov. Phys. JETP **83**, 1095 (1996).

[16] D. Vrinceanu and M. R. Flannery, Phys. Rev. Lett **85**, 4880 (2000).
[17] D. Vrinceanu and M. R. Flannery, Phys. Rev. A **63**, 032701 (2001).
[18] D. Vrinceanu and M. R. Flannery, J. Phys. B **33**, L721 (2000).
[19] D. Vrinceanu and M. R. Flannery, J. Phys. B **34**, L1 (2001).
[20] W. Pauli, Z. Phys. **36**, 336 (1926).

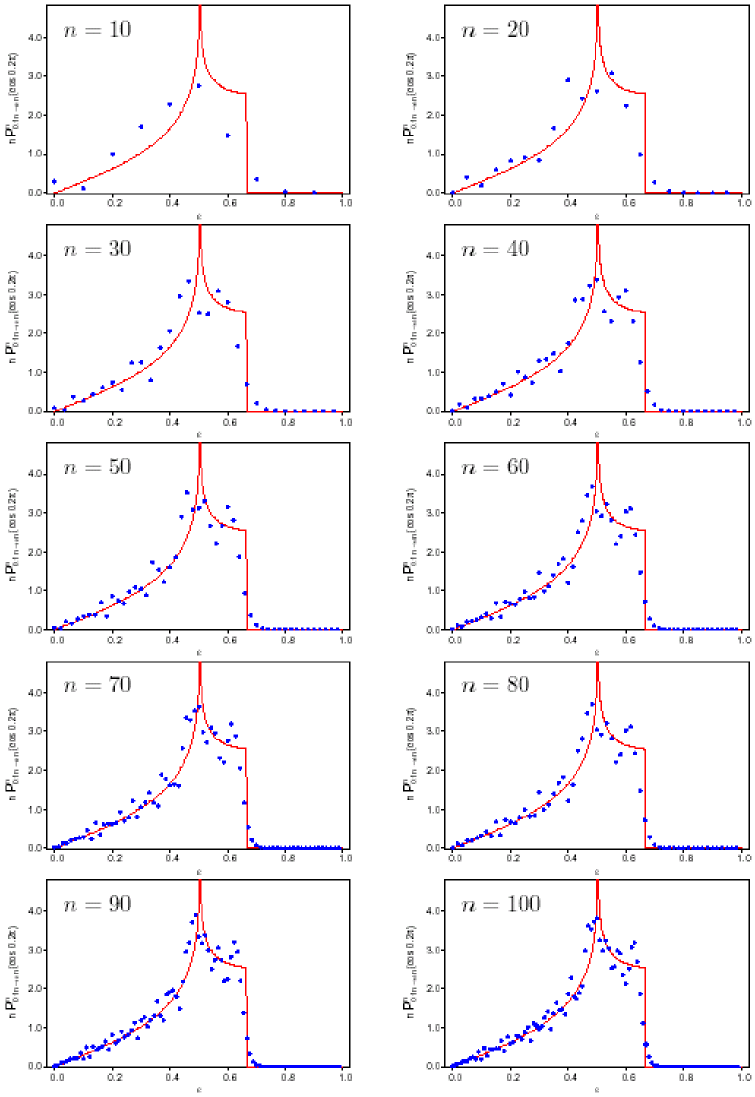

FIG. 1. Plots of the scaled transition probability $nP^{(n)}_{\ell\to\epsilon n}(\chi)$ as a function of the ratio $\epsilon = \ell'/n$ illustrating, as n increases, the convergence of the exact quantal results (blue dots) onto the fixed classical framework (red line), for constant values of the ratios $\ell/n = 0.1$ and $\chi = 0.2\pi$.

Recombination of Highly-charged Ions with Cold Electrons: Plasma Applications and Fundamental Spectroscopy

R. Schuch[*], M. Fogle, P.Glans[&], N. Eklow, E.Lindroth, S. Madzunkov, T. Ali Mohamed

Department of Atomic Physics, Physics Center, Stockholm University, S-169 33 Stockholm, Sweden

Recombination, one of the possible reactions of cold electrons with ions, has several important applications, besides being of fundamental interest. Astrophysical objects are studied through their radiation spectra emitted from electron-ion recombination; plasma modeling and diagnostics are based on the knowledge of recombination cross sections. It is the proposed mechanism for antihydrogen production in a trap filled with antiprotons and positrons. The most fundamental process of recombination is radiative recombination (RR): $Z^{q+} + e \rightarrow Z^{(q-1)+} + h\nu$

Recombination can also proceed via exciting an initially bound electron to form a doubly excited state in the $Z^{(q-1)+}$ intermediate system, in so-called dielectronic recombination (DR). Then the cross sections show strong resonant-like structure. Accurate measurements of these resonances in scattering of electrons at ions can be used for critical tests of calculations. The experiments presented here have both aspects in their motivations.

In the talk, we will present measurements of the recombination rate coefficients in absolute scale both in energy and height. The experiments are done with the electron cooler of the CRYRING storage ring at the Manne Siegbahn Laboratory in Stockholm. This electron cooler has an adiabatically expanded electron beam that gives electrons with mean transversal velocity component of 1 meV and longitudinal component of 0.1 meV.

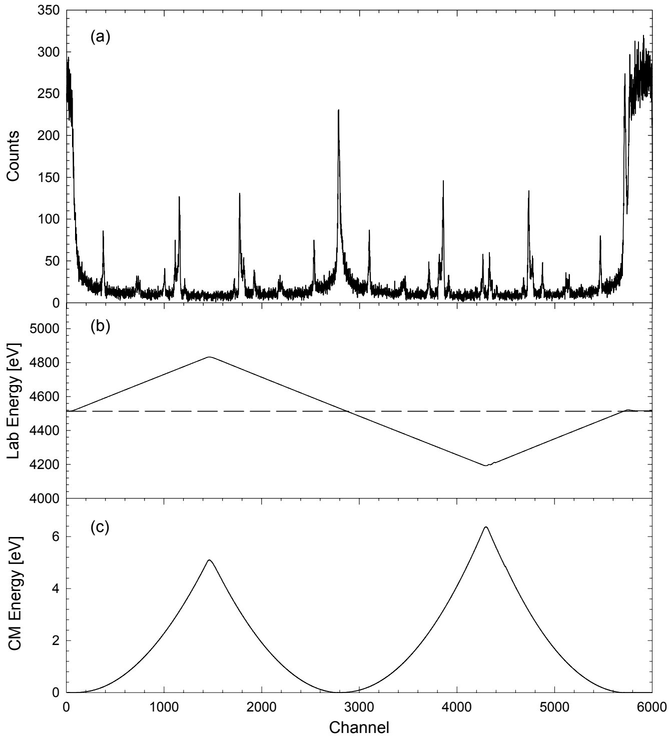

Fig. 1. (a)Time spectrum obtained by the zig-zag energy scan of the electrons as shown in (b). The spectrum consists of 4 complete data sets. Note that the high peak at the center, which is from the non-resonant recombinations, defines precisely the time and electron energy at which the electron velocity equals the ion velocity. For reference, the approximate interaction energy is show in (c).

---

[*] E-mail: schuch@physto.se

[&] present adress: Physics department, Mid- Swedish University, Sundsvall, Sweden

The highly charged ions were created in an electron-beam ion source, injected into the ring, and accelerated to several MeV/amu. After electron cooling of the ion beam for a few (1-3) seconds, the recombination rates as function of relative energy between electrons and ions were measured (Fig. 1). This was achieved by ramping the electron energy up and down from cooling to a maximum energy in the center-of-mass frame so that recombination spectra were obtained both with the electrons being slower and faster than the ions (see Fig 1). With the scans, as displayed in Fig. 1, we can check the correction for the drag effect on the ions when detuning the electron beam energy as well as for the space charge of the electron beam. These corrections are important in order to get accurate energy scales in the spectra[1]. For the low relative velocities scanned in these experiments (energies around 0-1 eV) it is possible to take full advantage of the low energy spread of the adiabatically expanded electron beam and a resolution in the order of meV was obtained. But data was also taken for an extended energy range of 0-40 eV. From fits to the resonances we confirm the longitudinal and transversal temperatures of the expanded electron beam to be less than 0.1 meV and 1-3 meV, respectively.

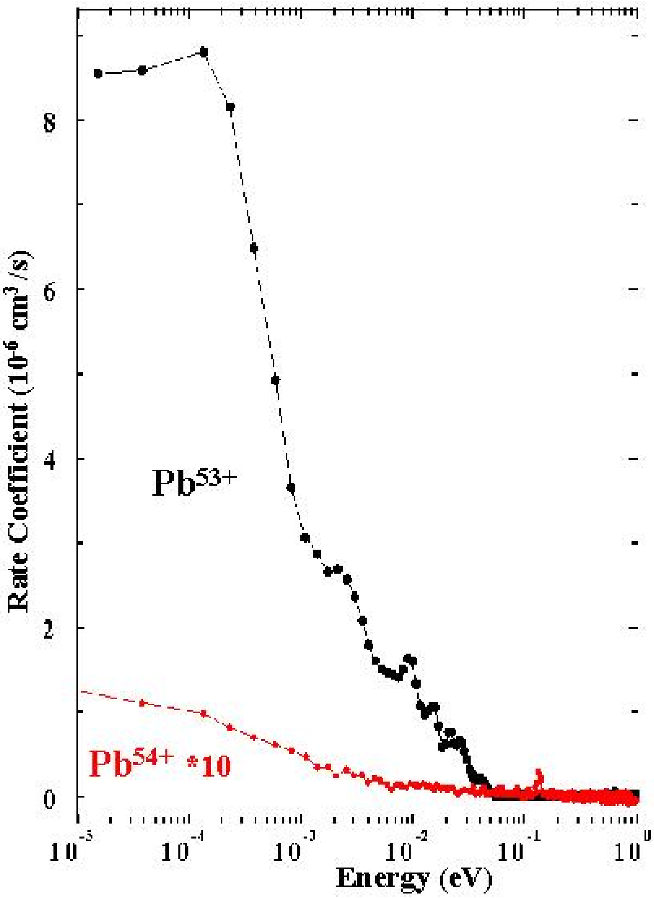

Fig.2 shows the recombination rate coefficients for the cases of Pb^{53+} and Pb^{54+}. Observe, the coefficients for Pb^{54+} are multiplied by 10.

In measurements using bare ions, where only the RR can occur, there is a consistent disagreement between the measured rates and the theoretical RR descriptions at very low relative energy[1-3]. And, it could be shown that this deviation depends on external fields, such as a weak magnetic field in the interaction region [4,5]. We concentrate here on examples for recombination with few-electron ions, such as Cu-like Pb^{53+}[6], Na-like Ni^{17+}[7], and Li-like N^{4+}[8] and Be^{+}[9]. All these ions considered have one valence electron in an s state. The lowest energy resonances are thus most likely formed by exciting the ns electron to np_j and bind the free electron to high n, for the example of Pb^{53+} it is a $4s_{1/2}$ to $4p_{1/2}$ excitation and simultaneous capture in a $18l_j$-state, with j=21/2. QED effects, such as self energy and vacuum polarization, are substantial in this highly charged ion and contribute to the $4p_{1/2}$-$4s_{1/2}$ splitting with 2 eV. In Fig.2 we show the rate coefficient for the case of Pb^{53+} and Pb^{54+}. Thus adding one electron in 4s makes the recombination rate around a factor 100 higher. A quantitative analysis of this experiment shows, that the DR-resonances can be determined with a precision of 1 meV and one is thus sensitive to the $4s_{1/2}$ to $4p_{1/2}$ splitting with the same precision[6]. This splitting is around 120 eV, which gives a relative accuracy in the 10^{-6} regime. It is clear that in cases where resonances are only a few meV above threshold, their position is determined by QED; and, the present-day ability to calculate the QED contribution to such a resonance energy is much larger than the experimental uncertainty.

The experimental results are compared with theoretical results, which were obtained by using three different computational schemes [8]. One method is based on relativistic many-body theory and is capable of meV accuracy for few electron systems (except for the QED effects). This method uses complex rotation to handle autoionizing states. The other two calculations use AUTOSTRUCTURE and R-matrix codes, respectively [8]. All these codes have advantages and disadvantages. Based on the comparison with the experimental spectra the quality of these theoretical methods can be discussed.

As an example we show here comparisons of four different calculations with our measurement for the Li-like ion N^{4+}. In this case we see a $2s_{1/2}$ to $2p_{1/2}$ excitation and simultaneous capture in a $4l_j$-states. QED effects are small in the $2s_{1/2}$ of this light ion, and are well corrected for.

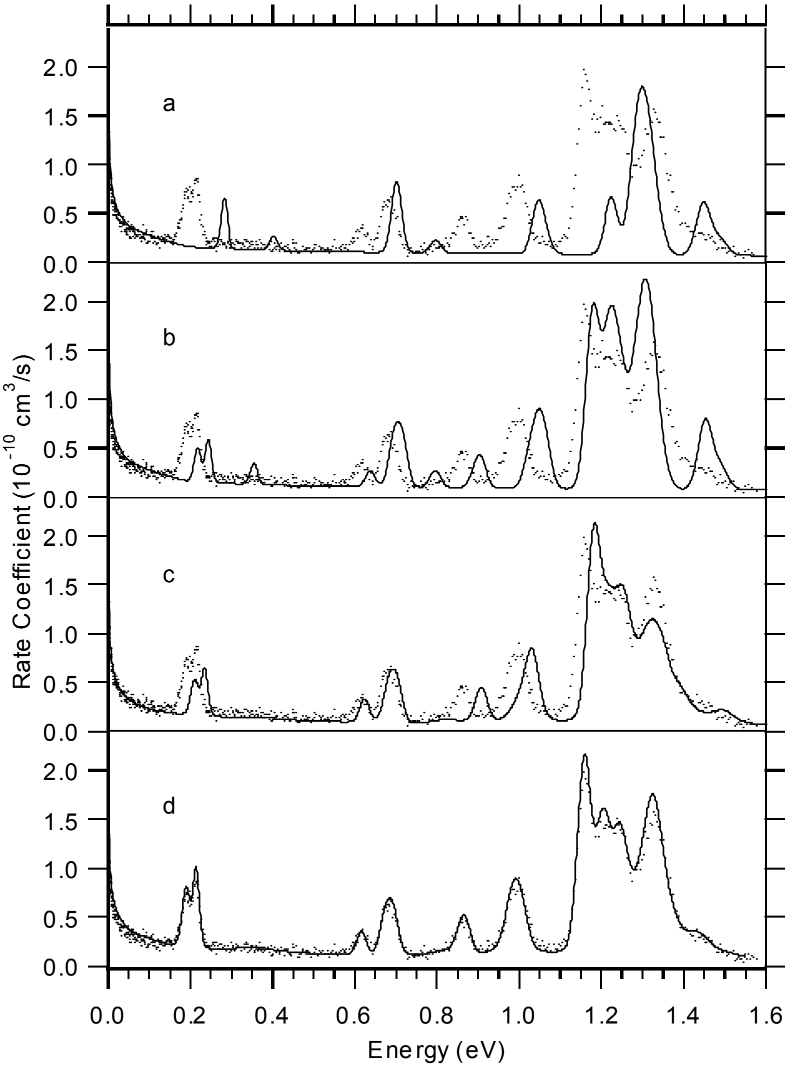

Fig.3: Comparison of the experimental recombination rate coefficient for N^{4+} with 4 different calculations [8]:
a) AUTOSTRUCTURE,
b) configuration interaction,
c) R-matrix,
d) rel. many-body perturbation theory.

Many of these measured rate coefficients are of interest to plasma or astrophysical applications. For some of the candidates such as Be, C, N, O, Fe, and Ni in several charge states, accurate experimental data is now available. For making the measured rate coefficients useful, they can be folded with Maxwellian temperature distributions of the kind as they exist in stars and in fusion plasmas. Examples for such temperature dependent rate coefficients are given and applications in astrophysics and plasma physics are discussed and compared to the theoretical values, which are presently available on data banks.

References

[1] R. Schuch, W. Zong, N. Badnell, *Int. Journ. of Mass Spectrometry* edt. T. Märk, **192**, 225, (1999)

[2] H. Gao, D. DeWitt, R. Schuch, W. Zong, S. Asp, and M. Pajek, *Phys. Rev. Letters* **75**, 4381 (1995)

[3] H. Gao, R. Schuch, E. Justiniano, D.R. DeWitt, W. Zong, W. Spies, and H. Lebius, *J. Phys. B Lett.* **30**, L499, (1997).

[4] G. Gwinner et al., *Phys. Rev. Letters* **84**, 4822 (2000)

[5] N. Eklow, P. Glans, W. Zong, R. Schuch, and H. Danared, *Hyperfine Interactions* **127**, 251 (2000)

[6] E. Lindroth, M. Tokman, P. Glans, Z. Pesic, G. Vikor, H. Danared, M. Pajek, and R. Schuch, *Phys. Rev. Letters* **86**, 5027, (2001)

[7] M. Fogle et al., submitted to P. R. A.

[8] P. Glans, E. Lindroth, N. Badnell, N. Eklöw, W. Zong, E. Justiniano, and R. Schuch, *Phys. Rev. A* **64**, 043609 (2001)

[9] T. Ali Mohamed et al., submitted to P. R. A.

The role of projectile potential energy in ion sputtering of surfaces

S. Cernusca, HP. Winter and F. Aumayr*)

Institut für Allgemeine Physik, TU Wien, Wiedner Hauptstr. 8-10, A-1040 Wien, Austria
**) e-mail: aumayr@iap.tuwien.ac.at*

Abstract

In recent studies on the impact of slow highly charged ions (HCl) on insulator surfaces, a dramatic increase of the sputtering yield with projectile charge has been observed. Compared to kinetic sputtering (i.e. sputtering of target atoms due to momentum transfer in collision cascades), which unavoidably causes radiation damage in adjacent regions, this new form of sputtering is induced by the potential energy of slow HCl (termed potential sputtering - PS) and holds great promise for a more gentle nanostructuring tool. Systematic experiments with slow HCl impinging on Au, LiF, NaCl, SiO_2, Al_2O_3, and MgO have explored the possible mechanisms leading to PS as well as the minimum potential energy necessary for its procedure.

Since during the last two decades intense sources for slow, highly charged ions (HCI) have become available, the possibility of exploiting the huge amount of potential energy stored in such projectiles for surface modification and nanofabrication has captured the imagination of researchers. Applications have been envisaged ranging from information storage via material processing to biotechnology. Compared to kinetic sputtering (i.e. sputtering of target atoms due to momentum transfer in collision cascades), which unavoidably causes unwanted radiation damage in adjacent layers, sputtering induced by the potential energy of slow highly charged ions (termed potential sputtering - PS) holds great promise for a more gentle nanostructuring tool. A profound understanding of the mechanisms responsible for the conversion of projectile potential energy in such PS processes is therefore highly desirable.

PS phenomena have so far been reported by several groups for a variety of insulator target surfaces as, e.g., alkali-halides [1, 2], SiO_2 [2], UO_x [3], GaAs [4], mica [5], and hydrocarbon contaminated surfaces (for recent reviews see, e.g., [6 - 8]). These investigations have in common that a dramatic increase of the total sputter yields, the secondary ion emission yields and/or the size of single ion - induced surface defects with increasing projectile charge state has been observed.

There has been a long debate in the literature whether potential sputtering is best described by a "Coulomb explosion" mechanism [9] or within the so-called "defect-mediated desorption" model [1, 2, 7] (see, e.g., the discussion in [6 - 8]). Recently another model involving structural instabilities because of a destabilization of atomic bonds due to high density electronic excitation [10] was proposed to explain the observed high sputtering yields of ref. [4]. Our data for projectile ions in lower charge states (q 27) [1, 2, 11] are at variance with the "Coulomb explosion" mechanism [7]. They are, however, consistent with the "defect-mediated desorption" model originally developed for electron- and photon-stimulated desorption (ESD, PSD) for alkali halides [12]. In this model localized defects (e.g. "self-trapped excitons", STE or "self trapped holes", STH) are formed following particle-hole excitations in the valence band of insulators with strong electron-phonon coupling such as alkali halides and silicon dioxide. Desorption of mainly neutral atoms follows the diffusion of defects to the surface. Theoretical estimates [7] show that the localization of electronic excitation by forming defects is an essential precursor for PS. In contrast, the lifetime of vacancies in the valence band is too short even in insulators for "Coulomb explosion" to contribute significantly to sputtering. Formation of a self-trapped hole requires a threshold excitation energy of about 10 eV for a LiF target surface [13]. In recent experiments [14] we have found a potential energy threshold, i.e. a minimum potential energy necessary to induce PS, at around this value of 10 eV, which unambigously proved that defect mediated desorption is the dominant mechanism for potential sputtering in alkali halides.

In order to identify further target materials which are subject to potential sputtering, we have extended our investigations to MgO_x, Al_2O_3 and Au. The defect mediated sputtering mechanism should of course not work for a conducting Au target surface. And, indeed, in preliminary experiments with multiply charged Ar ions in low charge state (up to 9+) we did not find any charge state dependence of the total sputter yield [11]. We were, however, curious, whether this pure kinetic behaviour would still hold for ions carrying considerably higher potential than kinetic energy (the potential energy of e.g. Xe^{25+} is around 8 keV, while the kinetic energy in our experiment varied between 0.1 and 1.5 keV.

In Fig. 1 the mass removal (in atomic mass units per incident ion, as determined by our quartz crystal microbalance technique[15]) due to impact of Ar^{q+} (q=1, 3, 8 and 9) and Xe^{q+} (q=9, 14, 19 and 25) ions on Au is plotted as a function of ion impact energy. Also shown are kinetic sputtering yields as calculated for neutral Ar - and Xe projectiles on Au by the SRIM-2000 code (the most recent version of TRIM [16]). Up to the highest charge states investigated (Xe^{25+}), the sputter yields measured for the Au target are independent of the projectile charge state [17]. The data points nicely follow the SRIM-2000 results, a code that only considers kinetic sputtering due to momentum transfer in a collision cascade. Therefore, our results provide convincing evidence that for a conducting Au target the potential energy of highly charged ions is not available for sputtering of surface atoms.

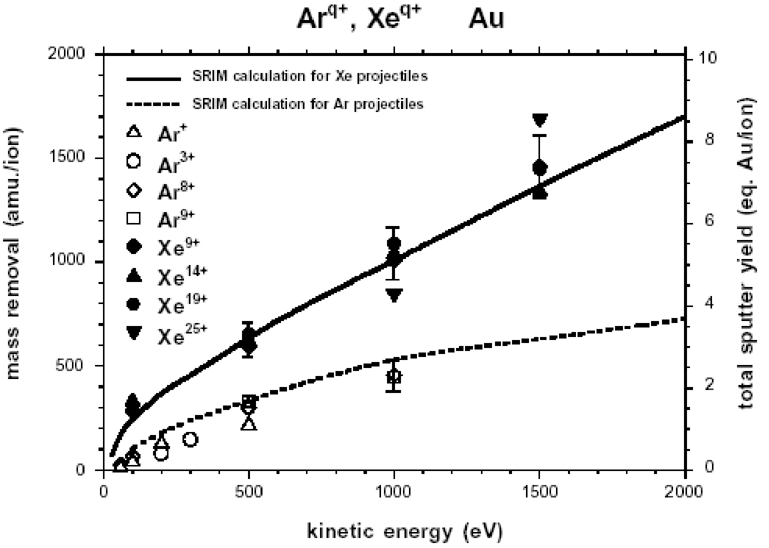

Fig. 1: Mass removal for sputtering of Au by singly and multiply charged Ar^{q+} (q=1, 3, 8 and 9; open symbols) and Xe^{q+} (q=9, 14, 19 and 25, full symbols) ions as function of ion impact energy (data from ref. [17]).

The defect - mediated sputtering mechanism requires a target material with strong electron phonon coupling, where electronic excitation can be localized by forming lattice defects via self-trapping. Self-trapping is known to occur for Al_2O_3 but not for MgO. Consequently we expected a strong charge-state dependence of the sputtering yield in the first case only. It came as a big surprise that a strong charge state effect was present, for both targets under bombardement with multiply charged Xe ions (figs. 2 and 3). While the results for Al_2O_3 can be explained within the defect mediated desorption model, the unusual behaviour of the measured total sputtering yields for MgO with projectile impact velocity, however, led us to the conclusion that we had encountered a new form of PS [18].

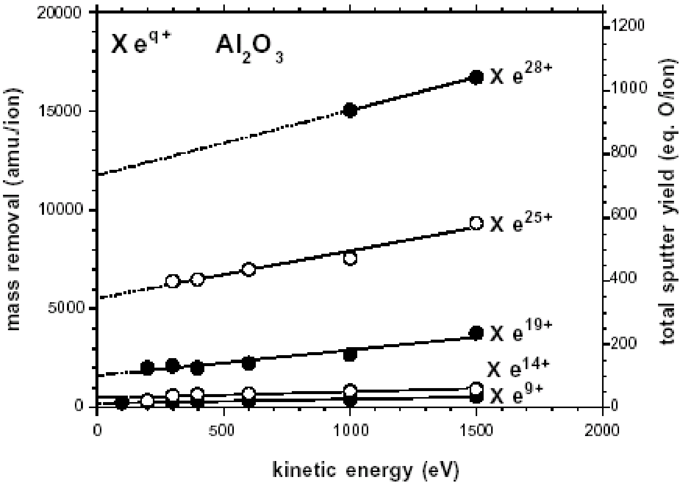

Fig. 2: Mass removal for sputtering of Al_2O_3 by highly charged Xe^{q+} (q=9, 14, 19, 25 and 28) ions as function of ion impact energy (data from ref. [18]). Lines for guidance only.

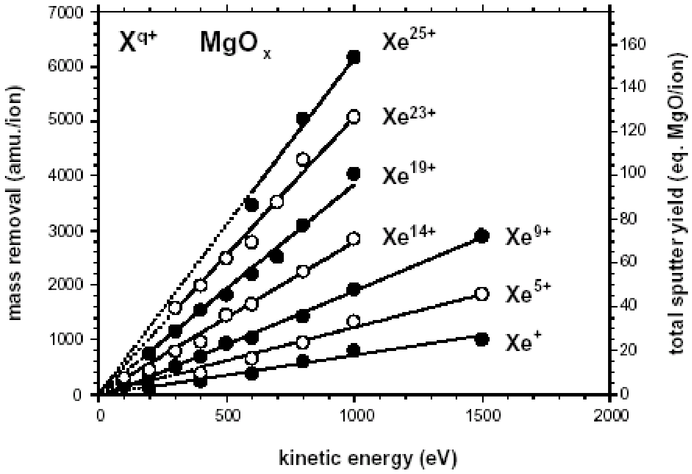

Fig. 3: Mass removal for sputtering of MgO_x by highly charged Xe^{q+} (q=1, 5, 9, 14, 19, 23, and 25) ions as function of ion impact energy (data from ref. [18]). Lines for guidance only.

In contrast to the case of alkali-halide or SiO_2 surfaces this mechanism requires the simultaneous presence of electronic excitations of the target material and of a kinetically formed collision cascade within the target in order to initiate the sputtering process [18]. This kinetically-assisted potential sputtering mechanism has meanwhile been identified to be present for other insulating surfaces as well, e.g. as a minor contribution in LiF (fig. 4), Al_2O_3 (fig. 2), and SiO_2. It might even provide an explanation for some projectile charge state dependent sputtering and secondary ion emission phenomena observed at considerably higher kinetic energies (see [3, 4] and refs. therein).

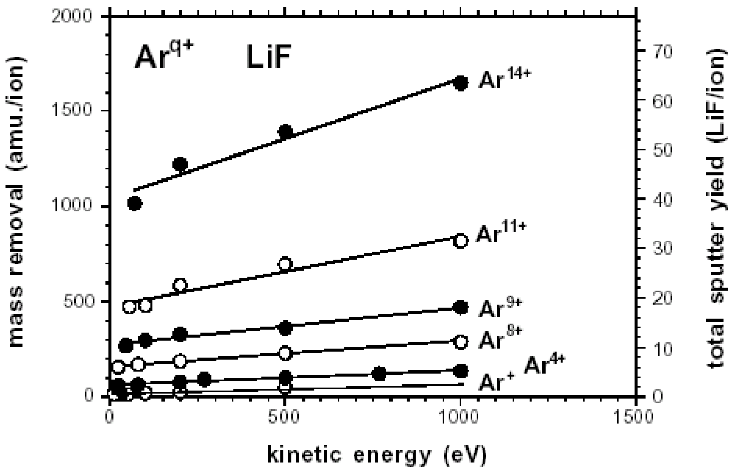

Fig. 4: Mass removal for sputtering of LiF by highly charged Ar^{q+} (q=1, 4, 8, 9, 11 and 14) ions as function of ion impact energy (data replotted from ref. [2]). Lines for guidance only.

ACKNOWLEDGEMENTS

This work was supported by Austrian Fonds zur Förderung der Wissenschaftlichen Forschung and carried out within Association EURATOM-OEAW.

REFERENCES

[1] T. Neidhart, et al. Phys.Rev.Lett. **74** (1995) 5280.
[2] M. Sporn, et al. Phys.Rev.Lett. **79** (1997) 945.
[3] T. Schenkel, et al. Phys. Rev. Lett. **80** (1998) 4325.
[4] T. Schenkel, et al. Phys. Rev. Lett. **81** (1998) 2590.
[5] D. H. Schneider, et al. Rad.Eff.Def.Solids **127** (1993) 113.
[6] A. Arnau, et al., Surf. Sci. Reports **27** (1997) 113.
[7] F. Aumayr, et al. Comments At. Mol. Phys. **34** (1999) 201.
[8] T. Schenkel, et al. Progr. Surf. Sci. **61** (1999) 23.
[9] I. S. Bitenskii, et al. Sov.Phys.Tech.Phys. **24** (1979) 618;
I. S. Bitensky, and E. S. Parilis, J. de Physique (Paris) **C2** (1989) 227.
[10] P. Stampfli, Nucl. Instrum. Meth. B **107**, 138 (1996);
P. Stampfli, K. H. Bennemann, Appl. Phys A **60** (1996) 191.
[11] P. Varga, et al. Physica Scripta **T73** (1997) 307.
[12] M. Szymonski, Mat.Fys.Medd.Kgl.Dan.Vidensk.Selsk. **43** (1993) 495 and references therein.
[13] L. Wirtz, et al. Surf. Sci. **451** (2000) 197
[14] G. Hayderer, et al. Phys. Rev. Lett. **83** (1999) 3948.
[15] G. Hayderer, et al. Rev. Sci. Instrum. **70**, (1999) 3696
[16] J. F. Ziegler, et al. *The Stopping and Range of Ions in Matter*. Pergamon, New York (1985), Vol. **1**.
[17] G. Hayderer, et al. Nucl.Instrum.Meth.Phys.Res. B. **182**, (2001) 143
[18] G. Hayderer, et al. Phys. Rev. Lett. **786**, (2001) 3530

Collisions of polyatomic ions with surfaces: Incident energy partitioning and chemical reactions.

Ján Žabka, Jana Roithová, Zdenek Dolejšek and Zdenek Herman

V. Čermák Laboratory, J. Heyrovský Institute of Physical Chemistry,
Academy of Sciences, Dolejškova 3, 182 23 Prague 8, Czech Republic

Collisions of polyatomic ions with surfaces were investigated in ion-surface scattering experiments to obtain more information on energy partitioning in ion-surface collisions and on chemical reactions at surfaces. Mass spectra, translational energy and angular distributions of product ions were measured in dependence on the incident energy and the incident angle of polyatomic projectiles. From these data distributions of energy fractions resulting in internal excitation of the projectile, translational energy of the product ions, and energy absorbed by the surface were determined. The surfaces investigated were a standard stainless steel surface, covered by hydrocarbons [1], carbon surfaces at room and elevated temperatures [2,3], and several surfaces covered by a self-assembled monolayers (C_{12}-hydrocarbon SAM, C_{11}-perfluorohydrocarbon SAM, and C_{11}hydrocarbon with a terminal -COOH group SAM) [4].

The main processes observed at collision energies of 10 - 50 eV were : neutralization of the ions at surfaces, inelastic scattering and dissociations of the projectile ions, quasi-elastic scattering of the projectile ions, and chemical reactions with the surface material (usually hydrogen-atom transfer reactions). The ion survival factor was estimated to be a few percent for even-electron ions (like protonated ethanol ion, $C_2H_5O^+$, CD_5^+) and about 10-10^2 times lower for radical ions (like ethanol and benzene molecular ions, CD_4^+).

In the polyatomic ion -surface energy transfer experiments, the ethanol molecular ion was used as a well-characterized projectile ion. The results with most of the surfaces studied [1,2,4] showed in the collision energy range of 13 - 32 eV that most collisions were strongly inelastic with about 6-8 % of the incident projectile energy transformed into internal excitation of the projectile (independent of the incident angle) and led partially to its further dissociation in a unimolecular way after the interaction with the surface. The incident energy transformed into the product ion translational energy varied with the incident angle between 18-45 % of the incident energy for the incident angle 40^0 - 80^0 with respect to the surface normal, respectively. The rest of the incident energy was absorbed by the surface. The only exception was the perfuloro-hydrocarbon SAM [4], where about 17% of the incident energy was transformed into internal energy of the polyatomic projectile. The hydrocarbon SAM behaved very similarly as the stainless steel or carbon surfaces, covered by hydrocarbons. The peak of the angular distributions of the product ions showed a simple correlation between the parallel and perpendicular components of the velocities of the incident and product ions.

Collisions of small polyatomic ions CD_5^+, CD_4^+, CD_3^+ (from methane) with carbon HOPG (highly oriented pyrolytic graphite) surface were investigated [3] at room and elevated (600^0 C) temperature of the surface. At the room temperature and collision energies of 7 - 52 eV, the main processes was inelastic dissociation of the projectile ion and chemical reactions with surface hydrocarbons. The main chemical product with CD_4^+ projectiles was CD_4H^+ (H-atom transfer) and its dissociation products, and formation of $C_2X_3^+$ and $C_3X_3^+$ (X=H,D) in reactions with terminal groups of the surface hydrocarbons. Complementary experiments with CH_4^+ and $^{13}CH_4^+$ enabled determination of the fraction of the product from projectile ion-surface chemical reactions and surface sputtering. Translational energy and angular distributions of the product ions together with the isotopic scrambling data provided new information on the details of the ion-surface chemical processes.

Partial support of this research by grants No. 203/97/0351 and 203/00/0632 of the Grant Agency of the Czech Republic is gratefully acknowledged. Part of this work was carried out within the framework of the Association EURATOM-IPP.CR, partly in cooperation with the Association EURATOM-ÖAW, Wien.

References

[1] J. Kubišta, Z. Dolejšek, and Z. Herman, *Eur. Mass Spectrom.* **4,** 311 (1998)
[2] J. Žabka, Z. Dolejšek, J. Roithová, V. Grill, T.D. Märk, and Z. Herman, *Int. J. Mass Spectrom.* **212**, (2001).
[3] J. Roithová, J. Žabka, Z. Dolejšek, and Z. Herman (to be published).
[4] J.Žabka, Z. Dolejšek, and Z. Herman, *J. Phys. Chem.* (submitted)

Dynamics and stability of charged clusters and droplets

B. Manil[$], F. Chandezon, H. Lebius[$], D. Duft*, T. Leisner*, C. Guet[#] and B.A. Huber

Département de Recherche Fondamentale sur la Matière Condensée (DRFMC)
Groupe des Ions Multichargés (GIM)
CEA-Grenoble, 17 rue des Martyrs, F-38054 Grenoble Cedex 9, France

In 1882 Lord Raleigh predicted [1] that a charged, incompressible liquid droplet becomes unstable as soon as the cohesive forces, which create the surface tension and which try to keep the droplet in its spherical equilibrium form, are equal to the Coulomb forces, which try to destabilise the droplet. In terms of energies, this means that the Coulomb energy E_C corresponds to twice the surface energy E_S. About half a century later [2,3] the ratio

$$X = E_C / 2\,E_S \tag{1}$$

has been called the fissility, thus characterising the Rayleigh limit by $X = 1$. Furthermore, Rayleigh claimed that for high charges ($X > 1$) higher multi-pole oscillations will become unstable and will provoke the emission of liquid in form of fine jets. Up to now these predictions have not been confirmed experimentally in a clear and convincing manner.

In the 1930th the liquid drop model has been applied with great success to other systems like atomic nuclei. In this case the charge is volume distributed in contrast to the surface charged droplets. Even the most heavy nucleus which has been produced recently with a nucleus charge of $Z = 114$, is characterised by an X-value smaller than 1 ($X \sim 0.9$ [4]). Therefore, the decay of the nucleus is a thermally activated process well below the Rayleigh limit, characterised by a fission barrier of finite height.

During the last decade a new effort has been started in the field of cluster physics with the aim to test the validity of the Rayleigh limit. In this case, metal clusters are ionised in collisions with highly charged ions, thus, allowing for the first time to prepare charged systems with a fissility larger than 1.

The experimental principle is as follows. Neutral sodium clusters are produced in a gas aggregation source. Sodium is heated in an oven to a temperature of 350 to 400°C. The hot sodium vapour (partial pressure ~ 0.1 mbar) expands into a cold He-atmosphere (pressure of several mbar, T ~77 K) where it condenses due to super-saturation. The formed clusters pass two differentially pumped sections before entering the interaction region, which is kept at a pressure of about 10^{-8} mbar (by using a liquid nitrogen cooled trap which encloses the extraction region). The cluster velocity depends on the cluster size and the source conditions, it ranges from 200 to 400 m/s [5]. The measured mass distribution follows a log-normal distribution as expected for this type of cluster source. The smallest clusters contain several tens of sodium atoms, the maximum occurs at around 150 atoms with a tail reaching to clusters made of 400 atoms. The cluster density within the beam is rather low at the interaction region, integrated over the whole size distribution it amounts to about 10^5-10^6 clusters/cm^3 [5].

The ions which are produced in a CAPRICE-ECR ion source [6] interact with the sodium clusters at the object point of a reflectron-type time-of-flight spectrometer, characterised by a mass resolution of ~ 15000 [7]. The ion beam is pulsed (10 μs, 3 kHz) as well as the extraction field for the produced cluster ions. After passing the time-of-flight system the extracted particles are detected by a channelplate device and finally registered by a ‘multi-hit’ start-stop system. Typical flight times are of the order of 100 to 200 μs.

In Figure 1 a small part of the measured mass spectrum is shown close to the stability limit of five-time charged sodium clusters. The intensity of these cluster ions disappears close to n/q ~ 21.6 corresponding to a so-called appearance size of n_{app} ~108. When we rewrite equation (1) for the case of sodium clusters we obtain :

$$X = E_C \,/\, 2\,E_S = q^2e^2 \,/\, 16\pi r_s^{3} n\sigma = \; 2.5\, q^2 \,/\, n\,, \tag{2}$$

where e is the elementary charge, r_s the Wigner Seitz radius and σ the surface tension. Thus, the measured appearance size for five times charges sodium clusters corresponds to a fissility of X (q=5) = 0.58, which is well below 1. Smaller systems with higher X-values decay by thermally activated processes due to their internal energy.

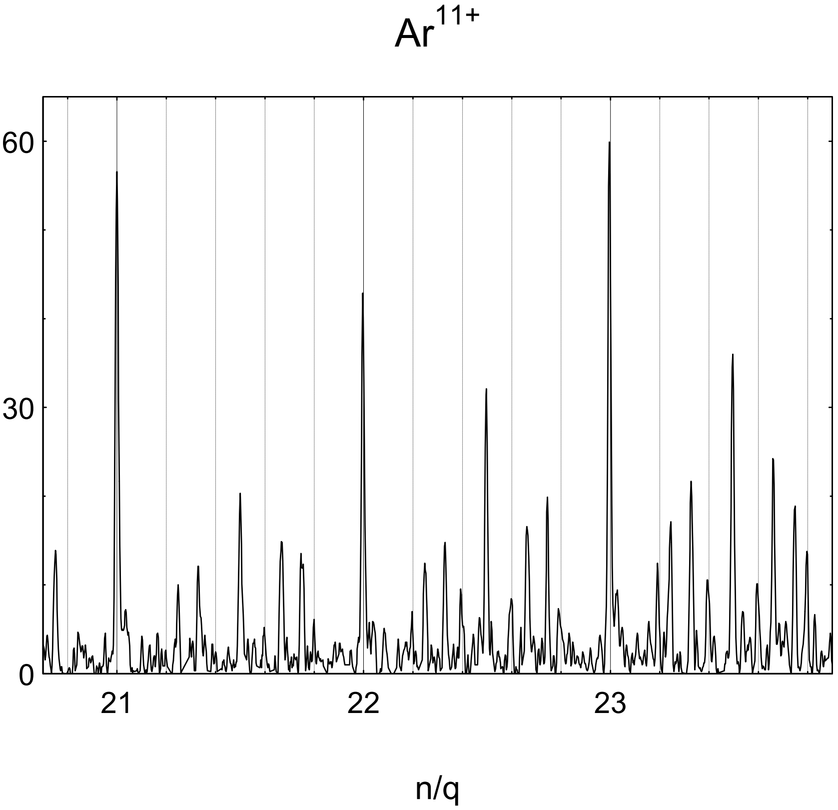

***Figure 1**:* Part of a time-of-flight spectrum of multiply charged sodium clusters Na_n^{q+} (transformed into size/charge values), produced in collisions of Ar^{11+} ions with neutral sodium clusters. The vertical lines mark the positions of five-time charged clusters.

In order to demonstrate the influence of the internal energy on the appearance size, we have performed experiments with highly charged projectiles (Xe^{28+}), in order to minimise the energy transfer during the collision, and clusters, the initial temperature of which has been varied with a heat bath between ~ 80 K and 400 K. In Figure 2 the appearance size of four times charged clusters is shown as a function of the initial cluster temperature and the charge state of the projectile used to ionise the neutral clusters. At the lowest initial temperature, the different points show that the appearance size strongly decreases with increasing projectile charge. This is due to the dominance of peripheral collisions with increasing charge. Whereas for laser ionisation n_{app} is found to be 123, close to the case of proton collisions (119), this value is as low as 71 in the case of Xe^{28+} projectiles. The corresponding X-values vary from 0.33 to 0.57. When comparing appearance sizes for a given projectile (O^{5+} - ions) but different initial temperatures, the value increases from 83 to 120 for T = 80 K to T = 350 K. This means that for a 4-fold ionisation of Na_{120} about 9 eV are transferred more in proton collisions than in collisions with O^{5+} , as in both cases different impact parameter ranges are effective.

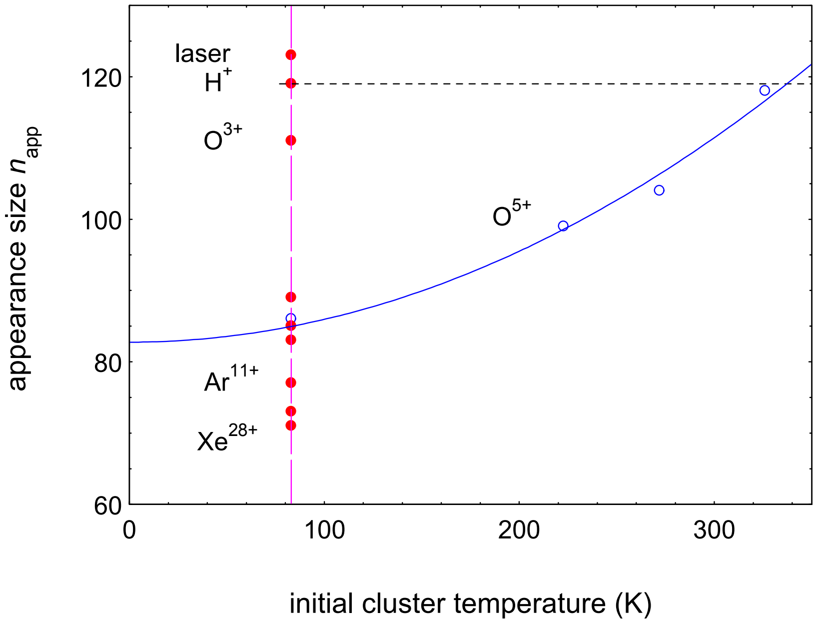

Figure 2: Appearance sizes for 4-times charged sodium clusters as a function of the initial cluster temperature. The values at 80 K (full circles) correspond to different projectiles, the open circles are obtained in collisions with O^{5+} ions at different cluster temperatures.

In Figure 3 the cluster ions at their appearance size are shown in a charge/size plot. The two lines marked by $X = 1$ and $X = 0.3$ characterise those systems where the fission barrier vanishes or its height is of the order of 1 eV, the activation energy for evaporation of neutral monomers. Our measurements show that with increasing cluster charge and consequently cluster size the detected systems indeed approach the Rayleigh limit (for q=10 we find X~ 0.85). However, it is not totally reached due to the initial cluster temperature (80 K) and the energy transfer in the collision.

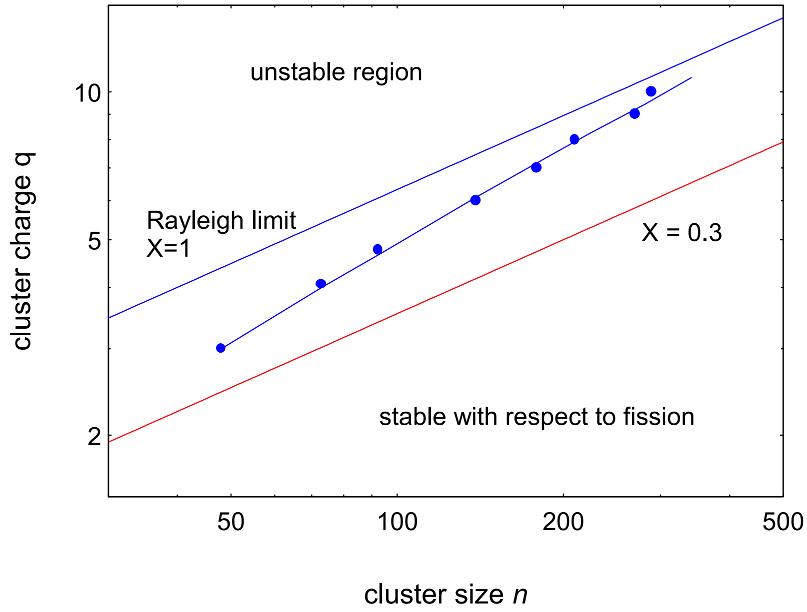

Figure 3: Cluster ions at their appearance size approaching the Rayleigh limit.

The temperature effects should be negligible for very large systems. Therefore, we have studied the stability and the explosion of highly charged microdroplets, which are injected into a Paul trap levitator. The charge to size ratio is determined from the levitator DC-voltage, the droplet diameter by an analysis of the Mie scattering signal from the droplet, which is irradiated with a HeNe laser. The diameters of the glycol droplets are of the order of 100 μm, the charges of several pC. Both entities are followed as a function of time during the evaporation of the droplet. We observe that successive explosions occur where about 20% of the charge is emitted whereas no mass loss is observable.

In addition we can analyse by the integrated scattered light intensity the quadrupole oscillations of the droplet, which are driven by the quadrupole field of the trap. Whereas the driving trap frequency is rather low (200 Hz), the Eigen frequency of the droplet is of the order of several tens of kHz. Therefore, the droplet can easily follow the driving force and we observe a certain amplitude of the oscillation which depends on the strength of the quadrupole field. Only when we approach the value of X=1, the Eigen frequency drops to zero and passes in the vicinity of X=1 the driven frequency. Indeed, we observe resonance phenomena just before each explosion, i. e. a strong increase of the amplitude and a phase shift of the oscillation. As the resonance is linked to $X \sim 1$, this is the first proof that the Coulomb instability of charged glycol microdroplets occurs at $X \sim 1$, as predicted by Lord Rayleigh.

** Institut für Physik, Universität Ilmenau, Postfach 100556, D-98684 Ilmenau, Germany*
$ CIRIL, rue Claude Bloch, BP5133, 14070 Caen Cedex 5, France
[#] *Dép. de Physique Théorique et Appliquée, CEA-Ile de France, BP 12, F- 91680 Bruyères le Châtel, France*

References

[1] Lord Rayleigh, *Phil. Mag.* **14**, 184 (1982)
[2] L. Meitner and O. Frisch, *Nature* **143**, 239 (1939)
[3] N. Bohr and J.A. *Wheeler, Phys. Rev.* **56**, 426 (1939)
[4] Yu.Ts. Oganessian et al., *Nature* (London) **400**, 242 (1999)
[5] T. Bergen et al., *Rev. Sc. Instrum.* **70,** 3244 (1999)
[6] X. Biquard et al., 2000 *Rev. Sci. Instrum.* **71** 2041
[7] F. Chandezon et al., *Phys. Rev. Lett.* **87**, 153402 (2001)

Molecular Chirality and the Dynamics of Electroweak Parity Violation

Martin Quack

ETH Zürich, Laboratorium für Physikalische Chemie, Wolfgang-Pauli-Str. 10
CH 8093 Zürich, Switzerland, email: Martin@Quack.CH

Abstract

New theoretical approaches and calculations of parity violation due to the electroweak force in polyatomic molecules have indicated, that the corresponding parity violating energy differences between enantiomers of chiral molecules are orders of magnitude larger than previously anticipated, although they are still predicted to be very small, on the order of $10^{-(16\pm3)}$ eV, depending on the molecule. This leads to a fundamentally new outlook on the magnitude of the expected symmetry breaking and hence the possibility of observing this phenomenon experimentally. We shall first review briefly the development of the field and outline the fundamental concepts. We then report on the current status with emphasis on recent theoretical work from the Zürich group including a discussion of the concepts for experiments and consequences for biomolecular homochirality as well as potential applications to high energy physics.

Introduction

The understanding of molecular chirality has played a key role in chemistry for a long time since its discovery by Pasteur 150 years ago [1–3]. Most current efforts in chemistry relate to synthetic and industrial applications of chiral compounds and some of these efforts have been honoured in 2001 by the Nobel prizes conferred upon William S. Knowles, Ryoji Noyori and K. Barry Sharpless.

However, molecular chirality is also important in relation to fundamental physics, in particular in relation to the underlying symmetries of physical laws. This relationship was pointed out by van't Hoff in an early review of the stereochemical concepts introduced in parallel by J. A. LeBel and himself [4]. Van't Hoff argues (rewritten here in modern notation) that the Gibbs energy $\Delta_\mathrm{R}G^\ominus$, the enthalpy $\Delta_\mathrm{R}H^\ominus$ and entropy $\Delta_\mathrm{R}S^\ominus$ of an isomerisation reaction between R and S enantiomers of a chiral molecule

$$\mathrm{R} \leftrightharpoons \mathrm{S} \qquad\qquad \Delta_\mathrm{R}G^\ominus = \Delta_\mathrm{R}H^\ominus - T\Delta_\mathrm{R}S^\ominus \tag{1}$$

all must be exactly zero at all temperatures for reasons of mechanical symmetry and thus the equilibrium constant K is always exactly equal to 1 because of

$$\ln K = -\Delta_\mathrm{R}G^\ominus/(RT) \tag{2}$$

This symmetry reasoning within a classical mechanical framework for the hypothetical molecular dynamics was retained in the framework of the quantum mechanics of chiral molecules. Hund noted in 1927 [5] that because of the invariance of the molecular hamiltonian under space inversion ($x \to -x, y \to -y, z \to -z$) nowadays frequently called the parity operation P, there will be a conserved good quantum number "parity" (Π) for the molecular eigenstates, which takes the values $+1$ if the energy eigenfunction is symmetric (χ_+) and -1 if it is antisymmetric (χ_-) under inversion. The probability density corresponding to the eigenfunctions is thus delocalized over R and S structures of chiral molecules and therefore corresponds to "achiral states" [6, 7].

The localized states σ and ρ corresponding to S and R can be generated as superpositions of energy eigenstates of well defined parity, which are separated by a tunneling splitting ($\Delta E_{\pm} = E_{-} - E_{+}$)

$$\begin{aligned} \sigma &= (\chi_{+} - \chi_{-})/\sqrt{2} \quad (3) \\ \rho &= (\chi_{+} + \chi_{-})/\sqrt{2} \quad (4) \end{aligned}$$

σ and ρ are time dependent and interconvert with a tunneling time for a transition from R to S

$$\tau_{\pm} = h/(2\Delta E_{\pm}) \quad (5)$$

Hund already estimated millions of years for such a tunneling process through the high potential barriers in the van't Hoff tetrahedral chiral carbon compounds, thus explaining the effective stability of the chiral enantiomers of these compounds (for a critical review, see [8]). This was actually the discovery and first application of the tunnel effect and in 2002 we shall be celebrating its 75th anniversary. In this context, it may be of interest to note that physics textbooks tend to attribute the discovery of the tunnel effect incorrectly to the later application to nuclear α-decay [9].

In the years following the formulation of modern quantum mechanics in 1925/26 by Heisenberg, Born, Jordan, Schrödinger and Dirac, the belief was expressed that the underlying physical laws relevant for all of chemistry were known [10]. It turns out that this was incorrect, as we know today that a further fundamental physical phenomenon had to be discovered in order to correctly understand molecular chirality. The discovery of parity violation due to the weak nuclear force [11,12] and the formulation of electroweak theory [13–15] has changed our outlook on the structure and dynamics of chiral molecules. It was quickly understood that because of the extremely small tunneling splittings estimated already by Hund, even very small parity violating perturbations in chiral molecules would lead to a real (very small) energy difference between enantiomers and thus a non zero $\Delta_{\mathrm{R}}H^{\ominus}$ in eq. (1). Yamagata already in 1966 [16] pointed out not only the energetic but also in a somewhat speculative manner the kinetic and possible biochemical consequences for the appearance of homochirality of life on earth. It turns out that Yamagata's estimates of $\Delta_{\mathrm{R}}H^{\ominus}$ were many orders of magnitude too large compared to what we know today and the kinetic mechanism that he proposed was even qualitatively inadequate to generate biochemical homochirality under realistic conditions, because of a fundamental quantitative flaw [17, 18]. Still, his proposal certainly kept interest in this question alive. Work in the decade following Yamagata's publication tried to improve the estimates of the effects of parity violation in molecules [19–23] but it is probably fair to say that all estimates remained rather qualitative; for the parity violating energy difference $\Delta_{\mathrm{pv}}E \approx \Delta_{\mathrm{R}}H^{\ominus}/N_{\mathrm{A}}$ they had acknowledged uncertainties of perhaps 5 or more orders of magnitude and, of course, the sign of $\Delta_{\mathrm{R}}H^{\ominus}$ for a given R/S pair was completely uncertain without a quantitative calculation. But this was nevertheless sufficient to confirm the general assumption that the parity violating energy differences $\Delta_{\mathrm{pv}}E$ could dominate over the exceedingly small hypothetical tunneling splittings $\Delta E_{\pm}$ for chiral molecules that are chemically stable against tunneling for long times in the sense of Hund (see for instance [22, 23]). Thus, it was clear that parity violation in spite of its small magnitude had a real stereochemical significance.

Quantitative Calculations of Molecular Parity Violation

Systematic quantitative quantum chemical calculations of parity violating energy differences were initiated with the single determinant excitation-restricted Hartree Fock approach (SDE-RHF) around 1980 [24, 25]. This theoretical approach was widely used for the following decade [26–28] leading to widely publicized results for biochemically relevant molecules such as amino acids and sugars [26–28] (for reviews see [6,28]). While alternatives were considered [29], the results from the SDE-RHF approach were generally believed firm and reliable.

The situation changed dramatically with the introduction of the new CIS-RHF (configuration interactions singles) approach to electroweak quantum chemistry by our group in 1995 [30–32] and later also the more efficient and powerful multiconfiguration linear response approaches (MC-LR) [33]. It turns out that in typical cases the calculated parity violating potentials are by one order of magnitude larger than previously considered [26–28]. Because at the same time it was shown that in the calculations the parity violating potentials appear as a trace of a tensor, $E_{\mathrm{pv}} = E_{\mathrm{pv}}^{xx} + E_{\mathrm{pv}}^{yy} + E_{\mathrm{pv}}^{zz}$, where the individual elements may have different sign and evolve independently in the calculations, this implies that none of the calculations on sign and magnitude of $\Delta_{\mathrm{pv}}E$ in polyatomic molecules prior to 1995 can be maintained.

Our new approaches have been applied to various problems in different molecules such as H_2O_2, H_2S_2, ethylene torsion (all these having been investigated already in the early work, but with very different results [26–28]), distorted CH_4, alanine in the gas phase and in solution, distorted acetylene, N_2O_4, CHBrClF, CDBrClF, fluorooxirane, S_2Cl_2, etc. [34–41]. Some of these new results could be confirmed by independent calculations in other research groups [42–46]. As the approach by Schwerdtfeger and coworkers, in particular, uses quite a different quantum chemical framework within Dirac Fock theory, but agrees nevertheless very well with the results from the Zürich group, one may hope that the recent theoretical approaches give quantitatively accurate results within the limits of basis sets and methodological convergence resulting in remaining uncertainties of perhaps 30 % in $|\Delta_{\mathrm{pv}}E|$, depending on the molecule [33]. With appropriate care (and cost),even much more accurate results are accessible to our approaches. We exclude here the always remaining possibility of some fundamental ommission that might be common to all current theories. This could be tested by experiment [47].

Our theoretical discovery of 1995/96 of the much increased order of magnitude of $\Delta_{\mathrm{pv}}E$ has thus led to considerable stimulus for current theoretical advances and has, at the same time, also stimulated experimental efforts, as the outlook on successful experiments is much better now than it was 10 years ago. Also experiments become increasingly important to test these now much more quantitative calculations for flaws in the theory as well as for their quantitative convergence.

Experimental Approaches towards Molecular Parity Violation

Until today no experiment has been successful in proving molecular parity violation. One may distinguish here spectroscopic experiments on isolated molecules in the gas phase from experiments on macroscopic samples. The latter have led to a number of claims, however not to adequate proof. The first proposal to measure directly the energy difference $\Delta_{\mathrm{pv}}E$ or $\Delta_{\mathrm{R}}H_0^{\ominus}$ between enantiomers was described in [47]. It relies on measuring the time evolution of parity in a coherent superposition of R and S states. However, the experiment can also be carried out in the frequency domain [6]. The key idea is to use an achiral intermediate molecular state of well defined parity.

Already earlier experiments have been proposed and carried out that try to measure spectroscopic frequency shifts [20, 48, 49]. Although these experiments do not provide direct access to $\Delta_{\mathrm{R}}H_0^{\ominus}$ they are more easily carried out, for instance in the microwave [50] or infrared [48, 49] region where they are actively pursued at high accuracy [51]. We refer to three papers presented by Stohner, Albert and Seyfang at SASP 2002 for related current work in our group, as well as to [6, 18] for further review and to [40, 41] for the question of biomolecular homochirality, which we will address in the lecture in detail. If time and space permit, we shall also address the question of the parity of superposition of left and right skis, first raised at SASP 1996 [52].

Acknowledgement

This paper is dedicated to the memory of Werner Lindinger. Our work is supported by ETH Zürich (including C^4 and CSCS) and Schweizerischer Nationalfonds. The work summarized here is the result of a large collaborative effort with many outstanding coworkers contributing as they appear in the list of references. Particular thanks go this time to Jürgen Stohner.

References

[1] L. Pasteur, C. R. Hebd. Seances Acad. Sci., **26**, 535 (1848).

[2] L. Pasteur, C. R. Hebd. Seances Acad. Sci., **27**, 401 (1848).

[3] L. Pasteur, Ann. Chim. Phys., **24**, 442 (1848).

[4] J. H. van't Hoff, "La chimie dans l'espace" in: B.M. Bazendijk (Ed.), Rotterdam 1887, reprinted in C. Bourgois (ed.) "Sur la dissymmetrie moleculaire", Coll. Epistème Paris 1986.

[5] F. Hund, Z. Physik, **43**, 805–826 (1927).

[6] M. Quack, Angew. Chem. Int. Ed. Engl., **28**, 571–586 (1989).

[7] M. Quack, Faraday Discuss. Chem. Soc., **99**, 389–398 (1994).

[8] R. Janoschek. In *Chirality*, page 18, Berlin, (1991). Springer-Verlag.

[9] G. Gamow, Z. Physik, **51**, 204 (1928).

[10] P. Dirac, Proc. Roy. Soc. (London), **A123**, 714–733 (1929).

[11] T. D. Lee and C. N. Yang, Phys. Rev., **104**, 254–258 (1956).

[12] C. S. Wu, E. Ambler, R. W. Hayward, D. D. Hoppes, and R. P. Hudson, Phys. Rev., **105**, 1413–1414 (1957).

[13] S. L. Glashow, Nucl. Phys, **22**, 579–588 (1961).

[14] S. Weinberg, Phys. Rev. Lett., **19**, 1264 (1967).

[15] A. Salam, In: Proceedings of the 8th Nobel Symposium (edited by N. Svartholm), Amkvist and Wiksell, Stockholm, page 367 (1968).

[16] Y. Yamagata, J. Theoret. Biol., **11**, 495–498 (1966).

[17] M. Quack, unpublished results.

[18] M. Quack, Nova Acta Leopoldina, **NF 81**, 137–173 (1999).

[19] D. Rein, J. Mol. Evol., **4**, 15 (1974).

[20] V. Letokhov, Phys. Lett. A, **53**, 275 (1975).

[21] B. Zel'dovich, D. Saakyan, and I. Sobel'man, JETP Lett., **25**, 94 (1977).

[22] R. Harris and L. Stodolski, Phys. Lett., **B78**, 313–317 (1978).

[23] R. Harris and L. Stodolski, J. Chem. Phys., **73**, 3862 (1980).

[24] D. W. Rein, R. A. Hegstrom, and P. G. H. Sandars, Phys. Lett., **A71**, 499 (1979).

[25] R. A. Hegstrom, D. W. Rein, and P. G. H. Sandars, J. Chem. Phys., **73**, 2329–2341 (1980).

[26] S. F. Mason and G. E. Tranter, Mol. Phys., **53**, 1091–1111 (1984).

[27] G. Tranter and A. McDermott, Chem. Phys. Lett., **130**, 120 (1986).

[28] S. F. Mason. *Chemical Evolution: Origins of the Elements, Molecules and Living Systems.* Clarendon Press, Oxford, (1991).

[29] L. Wiesenfeld, Mol. Phys., **64**, 739 (1988).

[30] A. Bakasov, T. K. Ha, and M. Quack. In J. Chela-Flores and F. Rolin, editors, *Proc. of the 4th Trieste Conference (1995), Chemical Evolution: Physics of the Origin and Evolution of Life*, pages 287–296, Dordrecht, (1996). Kluwer Academic Publishers.

[31] A. Bakasov, T. K. Ha, and M. Quack, J. Chem. Phys., **109**, 7263–7285 (1998).

[32] A. Bakasov and M. Quack, Chem. Phys. Lett., **303**, 547–557 (1999).

[33] R. Berger and M. Quack, J. Chem. Phys., **112**, 3148–3158 (2000).

[34] M. Quack and J. Stohner, Phys. Rev. Lett., **84**, 3807–3810 (2000).

[35] M. Quack and J. Stohner. In *SASP 2000, Proceedings of the XII Symposium on Atomic and Surface Physics and Related Topics* edited by Davide Bassi and Paolo Tosi, Univ. di Trento, Folgaria, Italy, pages PR–11, 1–4, (2000).

[36] M. Quack and J. Stohner, Z. Physik. Chemie, **214**, 675–703 (2000).

[37] R. Berger, M. Quack, and J. Stohner, Angew. Chem. Int. Ed., **40**, 1667 (2001).

[38] M. Gottselig, D. Luckhaus, M. Quack, J. Stohner, and M. Willeke, Helv. Chim. Acta, **84**, 1846 (2001).

[39] R. Berger, M. Gottselig, M. Quack, and M. Willeke, Angew. Chem. Int. Ed., **44**, 4195 (2001).

[40] R. Berger and M. Quack, ChemPhysChem, **1**, 57–60 (2000).

[41] R. Berger, M. Quack, and G. Tschumper, Helv. Chim. Acta, **83**, 1919–1950 (2000).

[42] P. Lazzeretti and R. Zanasi, Chem. Phys. Lett., **279**, 349–354 (1997).

[43] R. Zanasi and P. Lazzeretti, Chem. Phys. Lett., **286**, 240–242 (1998).

[44] J. K. Laerdahl and P. Schwerdtfeger, Phys. Rev., **A60**, 4439–4453 (1999).

[45] J. K. Laerdahl, P. Schwerdtfeger, and H. M. Quiney, Phys. Rev. Lett., **84**, 3811–3814 (2000).

[46] J. K. Laerdahl, R. Wesendrup, and P. Schwerdtfeger, ChemPhysChem, **1**, 60–62 (2000).

[47] M. Quack, Chem. Phys. Lett., **132**, 147–153 (1986).

[48] O. Kompanets, A. Kukudzhanov, V. Letokhov, and L. Gervits, Opt. Commun., **19**, 414 (1976).

[49] E. Arimondo, P. Glorieux, and T. Oka, Opt. Commun., **23**, 369 (1977).

[50] A. Bauder, A. Beil, D. Luckhaus, F. Müller, and M. Quack, J. Chem. Phys., **106**, 7558–7570 (1997).

[51] C. Daussy, T. Marrel, A. Amy-Klein, C. Nguyen, C. Bordé, and C. Chardonnet, Phys. Rev. Lett., **83**, 1554–1557 (1999).

[52] A. M. Q. Zack. In *SASP 1996, Proceedings of the Xth International Symposium on Atomic, Molecular, Cluster Ion and Surface Physics* edited by J. P. Maier and M. Quack, VdF Publishers, Zürich 1996, pages 305–309 (ISBN 3-7281-23292).

Infrared spectroscopy of gas-phase clusters using a free-electron laser

Deniz van Heijnsbergen[1], Gerard Meijer[1,2] and Gert von Helden[1]

[1]*FOM Institute Rijnhuizen, Edisonbaan 14, 3439 MN Nieuwegein, The Netherlands*
[2]*Department of Molecular and Laser Physics, University of Nijmegen, Toernooiveld 1, NL-6525 ED Nijmegen, The Netherlands*

Introduction

Laser vaporization in pulsed nozzle sources has made it possible to produce a fantastic variety of atomic clusters. For carbon clusters, variations on these methods made it possible to produce C_{60} and the related fullerenes and nanotubes in macroscopic quantities and to study them using conventional spectroscopy. However, most clusters produced in the gas phase, especially those containing metals, remain largely uncharacterized. Among these are transition metal-carbide,-oxide and -nitride clusters,

The free-electron laser FELIX [1] at the FOM Institute “Rijnhuizen” is ideally suited for a large variety of experiments in gas phase molecular physics. In particular, its wide wavelength tuning range, covering (almost) the full `molecular fingerprint' region, combined with high power and fluence make FELIX ideally suited to excite gas-phase species such as gas-phase clusters. When FELIX is tightly focussed and resonant with an IR active mode of the cluster, the excitation of the cluster can become very high. For hot clusters, several cooling pathways exist and for strongly bound species with low lying ionization potentials, the thermal emission of an electron (thermionic emission) can become the dominant process. We exploit this thermionic emission to record IR spectra of strongly bound gas-phase clusters. Here, results from experiments of titanium carbide clusters are presented [2,3].

Titanium carbide clusters were investigated before using mass spectrometric techniques. The Ti_8C_{12} ``met-cars'' clusters were first reported by Castleman and coworkers [4]. They proposed a structure in which both metal and carbon are present in the wall of a symmetric cage with 12 five-membered rings on its surface (T_h symmetry). The $Ti_{14}C_{13}$ cluster was suggested to have a 3x3x3 nanocrystalline cubic structure [5]. Neither the Ti_8C_{12} nor the $Ti_{14}C_{13}$ clusters have been isolated, and there is no spectroscopic data which can confirm or disprove the proposed structures

Experimental

The clusters of interest are produced by pulsed laser vaporization from a solid metal rod in an expansion containing several percent reactant gas. A scheme of the setup is shown in Figure 1. About 20-30 mJ of a frequency doubled Nd:YAG laser (Spectra Physics GCR 150) are focused on the metal surface. The metal rod can have a diameter of 6 or 12 mm and is rotated and translated to regularly expose a fresh spot on the surface. Gas from a pulsed valve (R.M. Jordan Inc.) quenches the laser plasma, clustering and chemical reactions occur and the clusters and carrier gas expand into vacuum. When performing experiments on metal-carbides, 5 % CH_4 (or $^{13}CH_4$) is seeded in argon. For metal oxides, 1-5 % O_2 in argon and for experiments on metal nitrides, 1-5 % N_2 in argon is used. The beam is skimmed and enters the region between the acceleration plates of a reflectron Time Of Flight (TOF) mass spectrometer (R.M. Jordan Inc.) that is 20 cm downstream of the cluster source. Ions produced directly in the source plasma are blocked with an electric field (500-1000 V/cm) perpendicular to the molecular beam that is located directly after the skimmer, about 5 cm prior to the TOF region.

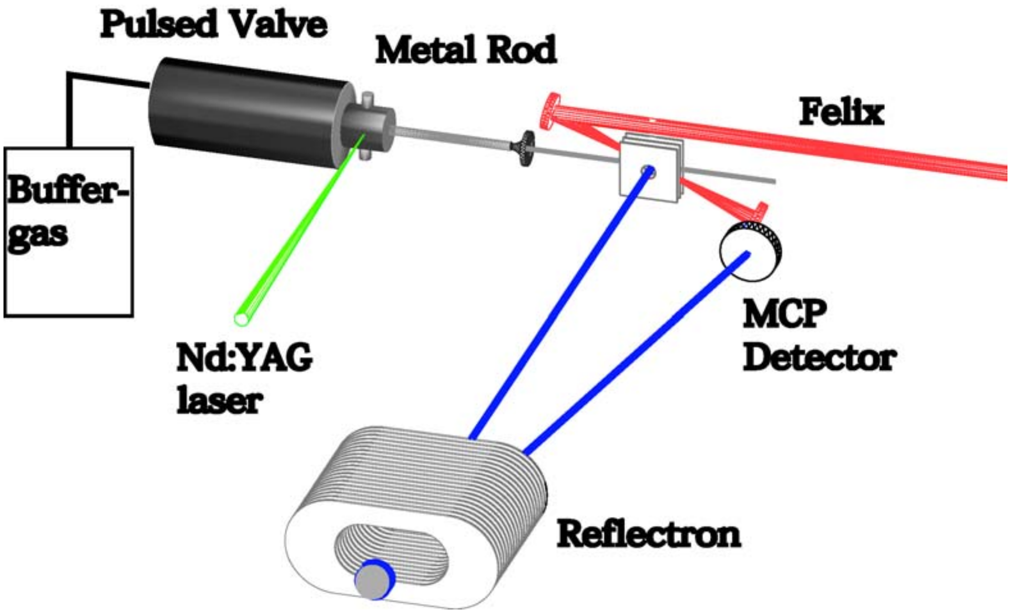

Figure 1: Scheme of the experimental setup. Neutral clusters are generated by laser vaporization techniques. Ions that are created after interaction with FELIX are anayzed in a time of flight mass spectrometer.

The FELIX beam enters the chamber above the axis of the molecular beam and is focussed on the cluster beam using a 7.5 cm focal length gold mirror. The laser beam is focussed back using a 3.75 cm focal length mirror thus effectively doubling the micropulse repetition rate and thus the fluence that clusters are exposed to. The molecular beam moves with a typical beam velocity of 600 m/s. The IR laser beam focus will be, depending on wavelength, between tens of microns to several hundreds of microns in size. The clusters will thus not be exposed to the entire FELIX macropulse but see only up one microsecond of it.

To be able to resonantly pump a large amount of energy into a cluster, the available energy per µs is thus a crucial factor. One feature that really distinguishes FELIX from most other free-electron lasers is that FELIX has the highest output energy per micro-second throughout its tuning range of 5 – 250 µm. The light output consists of macropulses that are 5 µs long and come at a repetition rate of 10 Hz. Each macropulse consists of micropulses that come at a repetion rate of 1 GHz (1 ns spacing) or 25 MHz (40 ns spacing). The micropulse length can be adjusted and range from 300 fs to several ps. The bandwidth is transform limited and can range from 0.5 % FWHM of the central wavelength to several percent. In the 1 GHz mode, the output energy can be up to 150 mJ / macropulse.

Results and Discussion

Figure 2 shows the spectra of three selected clusters as the infrared ionization laser is tuned through the region of 400 to 1670 cm^{-1}. It is immediately apparent that there is a strong wavelength dependence to the ionization yield and that this wavelength dependence is different for the different cluster masses measured. The Ti_8C_{12} ``met-cars" cluster has a strong resonance centered at 1395 cm^{-1} (1345 cm^{-1} for the ^{13}C cluster), while the $Ti_{14}C_{13}$ cluster has no measurable resonance in this wavelength region. The frequencies measured can be associated with vibrational resonances for specific structural patterns in these clusters. The 1395 cm^{-1} band in Ti_8C_{12} is logically associated with a C--C stretching mode. The $Ti_{14}C_{13}$ cluster has two resonances in the longer wavelength region at 630 and 485 cm^{-1} (610 and 475 cm^{-1} for the ^{13}C cluster). The low frequency features are particularly strong for the $Ti_{14}C_{13}$

cluster. Bulk TiC with the well-known rock-salt structure, has surface phonon resonances in this region [6].

For Ti_8C_{11} and Ti_8C_{12}, the measured IR spectra are consistent with those expected for the so called “met-car” structures [4]. All larger clusters show IR spectra that are indicative for bulk-like nanocrystalline structures [5]. The spectra of all those larger clusters do not depend strongly on cluster size and show resonances at positions where k=0 phonons of the TiC (100) surface are known to be [6].

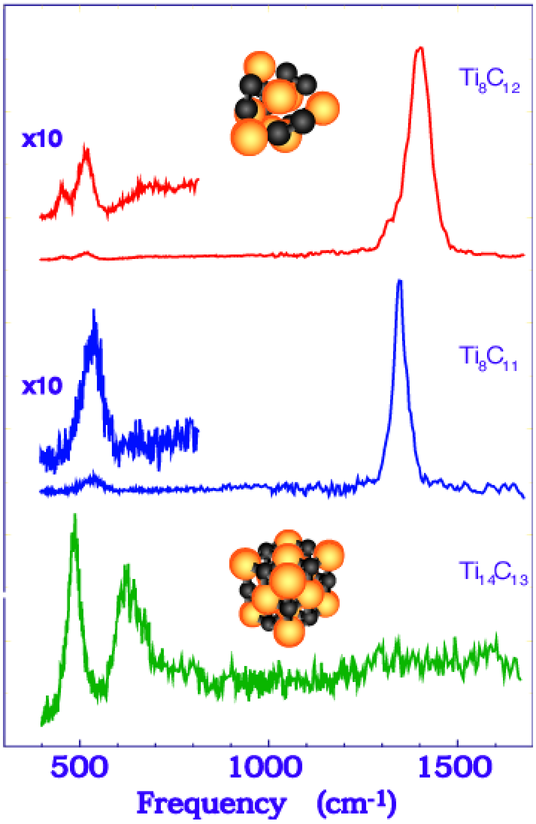

The infrared resonance-enhanced multiphoton ionization spectra obtained for the Ti_8C_{12}, Ti_8C_{11} and $Ti_{14}C_{13}$ clusters are shown. In each spectrum the indicated parent molecular ion yield is measured while tuning the infrared wavelength. The structures proposed previously for Ti_8C_{12} and $Ti_{14}C_{13}$ are shown in the figure.

Surprisingly, strongly bound gas phase clusters can also be of importance in astrophysics. In an active collaboration with a group of astrophysicists, we identified a well-known emission feature observed at wavelengths around 20.1 microns in spectra of post-asymptotic giant branch (post-AGB) stars, to the emission of titanium-carbide clusters. For more than a decade, the strange infrared glow coming from certain red giant stars had puzzled astronomers. Originally identified by the Dutch-American IRAS satellite in 1988, this emission became known in the astronomical community as the `21-micron mystery' [7]. Although it was known that meteorites contain micrometer-sized graphite grains with embedded titanium carbide grains, and although isotopic analysis had identified asymptotic giant branch stars as the birth sites of these grains, the possibility that the mysterious 21-micron emission might originate from titanium carbide crystals was never considered. Only after our laboratory measurements revealed the spectroscopic signature of titanium carbide nano-crystals, the mystery was unambiguously solved. In the figure, an IR spectrum of TiC clusters as measured at Rijnhuizen is shown (lower trace). This can be compared to the emission spectrum of a post-AGB star. Clearly, the match is very good.

The results shown here represent the first infrared spectra of gas phase metal clusters. Infrared spectroscopy is particularly problematic for these species due to the intrinsically weak absorption in this region and the limited availability of intense tunable light sources. The method presented here is uniquely suited to strongly bound clusters with low ionization energies, a condition which is met for many pure metal clusters and metal compound clusters. The IR-REMPI method using widely tunable free electron lasers therefore provides unprecedented opportunities to probe the structures and dynamics of size-selected metal, non-metal and semiconductor atomic clusters in the isolated gas phase environment. Recent results on metal-carbide, -oxide and –nitride clusters will be presented in the talk.

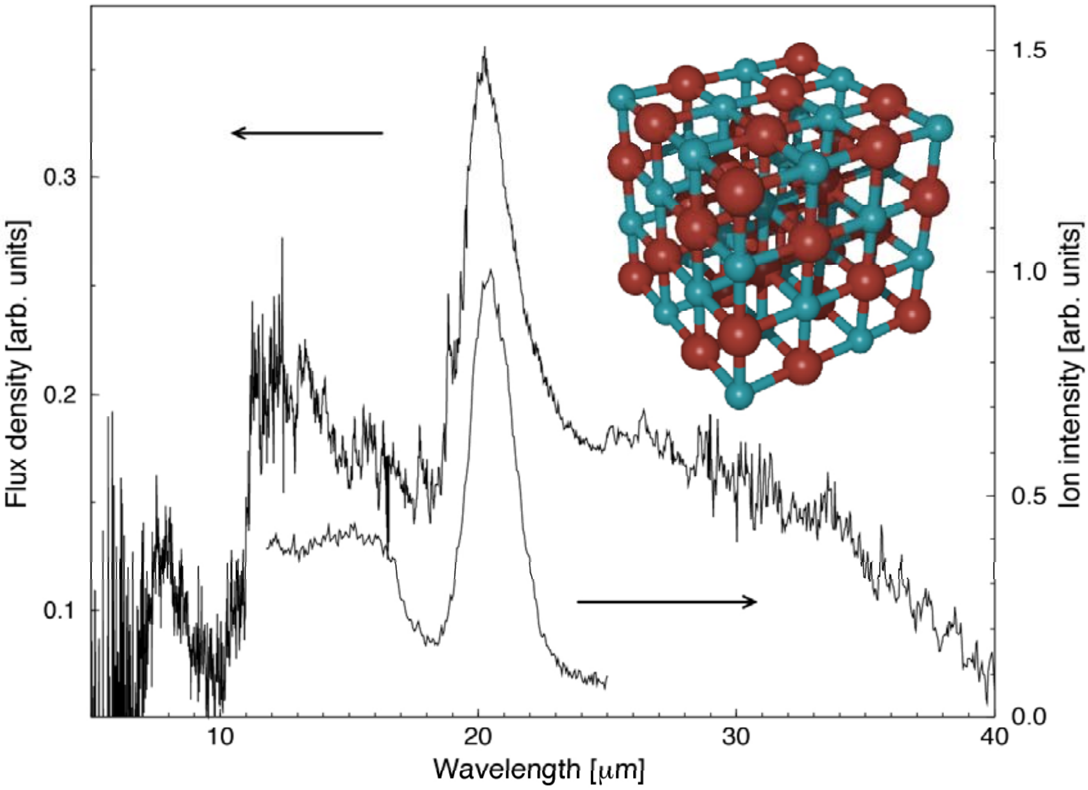

Figure 3: The emission spectrum from the post--AGB object SAO 96709, taken by the ISO satellite (upper trace, left axis) and the wavelength spectra of TiC nanocrystal clusters recorded in the laboratory (lower trace, right axis). Also shown is a pictorial representation of a typical (4x4x4 atom) TiC nanocrystal.

References

[1] G.M.H. Knippels, R.F.X.A.M. Mols, A.F.G. van der Meer, D. Oepts, and P.W. van Amersfoort, *Phys. Rev. Lett*. **75**, 1755 (1995).

[2] D. van Heijnsbergen, G. von Helden, M.A. Duncan, A.J.A. van Roij and G. Meijer, *Phys.Rev.Lett* **83**, 4983 (1999).

[3] G. von Helden, A.G.G.M. Tielens, D. van Heijnsbergen, M.A. Duncan, S. Hony, L.B.F.M. Waters and G. Meijer, *Science* **288**, 313 (2000).

[4] B.C. Guo, K.P. Kearns, and A.W. Castleman Jr., *Science* **255**, 1411 (1992).

[5] J.S. Pilgrim, and M.A. Duncan, *J. Am. Chem. Soc.* **115**, 9724 (1993)

[6] C. Oshima, T. Aizawa, M. Wuttig, R. Souda, S. Otani and Y. Ishizawa, *Phys.Rev.B*. **36**, 7510 (1987).

[7] *News Focus* Article*, Science* **284**, 1113 (1999)

Melting and Boiling of Clusters

Martin Schmidt, Thomas Hippler, Jörn Donges, Bernd von Issendorff and Hellmut Haberland

Fakultät für Physik der Universiät Freiburg, Germany

All properties change with the size of a cluster. The transition from the atom/molecule to the bulk is often quite smooth and the asymptotic behaviour well understood[1]. This is not the case for cluster melting, where large and irregular fluctuations are found even for clusters containing more than hundred atoms.

We have recently developed a method to measure caloric curves for size selected cluster ions[2, 3, 4, 5]. The caloric curve is a plot of the cluster energy as a function of cluster temperature, and contains all its basic thermodynamic properties. Our method can be divided into two steps. In step 1, sodium cluster

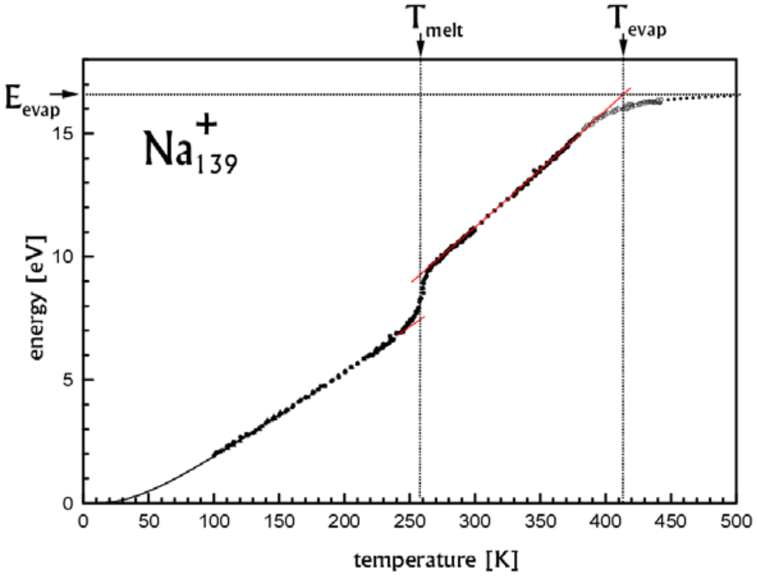

Figure 1: Caloric curve for Na^+_{139}. The cluster energy is plotted against the temperature of the heat bath of the clusters. Below 100 K the curve has been extrapolated using the bulk result. The increase near 260 K is due to the melting process. Melting temperature and latent heat can be easily read off the curve. Above 400 K the data deviate from the caloric curve as the cluster can no longer be thermalized. They are so hot that they evaporates already in the heat bath. This situation corresponds to an evaporative ensemble, whose temperature and energy can be so determined. It has been argued in ref.[6] that the evaporative ensemble corresponds to cluster boiling at a low pressure.

ions are produced and thermalized. The heat bath is a helium gas of known temperature T, where the clusters make so many collisions that they reach thermal equilibrium. The thermalized clusters are extracted, transferred to high vacuum, and mass analyzed. One has thus prepared a cluster of known mass and known temperature T.

In step 2 the internal, dominantly vibrational energy E of the cluster is measured by a photofragmentation technique explained earlier[2, 4, 7, 8]. If one knows E and T one can plot the caloric curve $E = E(T)$. Fig. 1 shows an example. Below the melting temperature, the caloric curve has about the slope expected by the classical Dulong–Petit law of $3\mathrm{k}_B$, where k_B is Boltzmann's constant. Near the melting point, there is a stronger increase of energy over a small temperature interval. For an arbitrarily large system, this increase would be abrupt. We take as melting temperature ($\mathrm{T}_{\mathrm{melt}}$) the position of the largest slope of the caloric curve. The latent heat is given by the step height of the smoothed-out step.

The melting temperatures are given in Fig. 2. They show surprisingly large variations: one additional atom can change T_{melt} by up to 10 K. This result is very far from the expected $(\mathrm{radius})^{-1}$ behaviour often deduced for supported, non–mass selected clusters. Two main points can be observed: 1) the melting

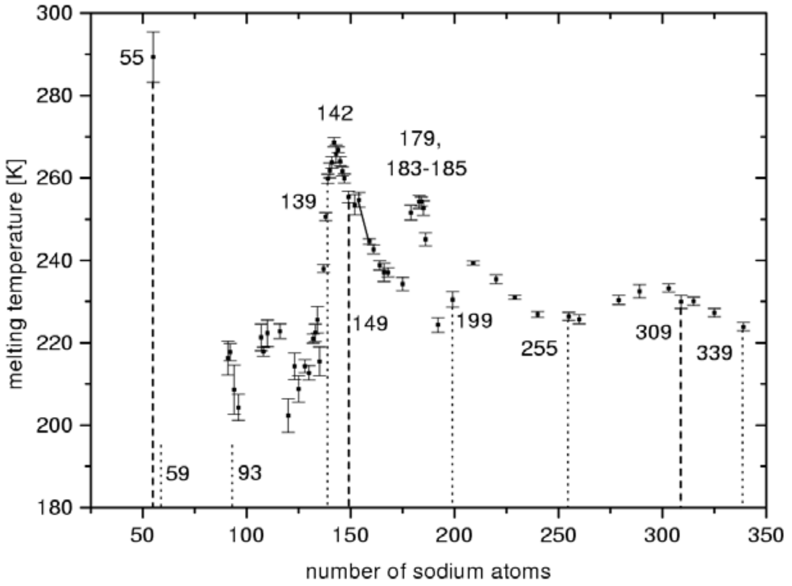

Figure 2: The melting temperatures of Na_n^+ are plotted against the number of atoms. Large fluctuations are seen whose origin is not well understood. They do not correlate with electronic (dotted line) or geometric (dashed) shell closings, which are indicated in the figure. The bulk melting temperature is 371 K. Note, that the zero is suppressed.

temperatures are about one third lower than in the bulk, and 2) they fluctuate by ± 50 K. From less complete data it had earlier been conjectured that the melting points are high, if electronic and geometric shell closings are close to each other[4]. This is no longer supported by the new data covering a wider mass range.

Several calculations have been performed on melting of sodium clusters, but the overall structure of the data in Fig. 2 has not been reproduced so far. The number of atoms for the maxima and minima in Fig. 2 do not generally correspond to any known shell closings, be they electronic or atomic in origin. Also, it might be that the cluster changes its geometry near the melting temperature, as has been observed in a simulation on gold clusters by Landman[9] et al.

There are several features that make cluster melting – or more generally phase transitions in finite systems – an interesting physical problem[3, 5, 10]: One can develop a thermodynamics of finite systems[10] and observe how the standard Boltzmann–Gibbs statistical mechanics (where always infinitely large systems are considered) is emerging as a limiting case. The most important difference between bulk and finite systems is, that the energy in the latter can be non–additive, i.e the sum of the energies of N particles is not proportional to N. This property is also called *nonextensive*. Nonextensivity occurs if the range of interactions is not negligible compared to the diameter of the system. This has far reaching consequences[10]: e.g. the heat capacity can become negative. Near a phase transition, a small system can become cooler upon heating, as was predicted long ago[10, 11] but only very recently observed experimentally[12, 13].

The liquid to gas transition of finite systems has received much less attention. It has been linked to the evaporative ensemble in a Gedankenexperiment[6]. A first measurement was reported[13] by a Lyon/Innsbruck group, which has used a method adapted from Nuclear Physics to study this phase transition in hydrogen clusters.

This research was supported by the Deutsche Forschungsgemeinschaft through SFB 276.

References

[1] J. Jortner, J.Phys.D24, 247 (92)

[2] M. Schmidt, R. Kusche, W. Kronmüller, B. v. Issendorff, and H. Haberland, Phys. Rev. Lett. 79, 99 (1997)

[3] G. Bertsch, Science 277 1619 (1997)

[4] M. Schmidt, R. Kusche, B. v.Issendorff, and H. Haberland, Nature 393 238 (1998)

[5] R. S. Berry, Nature 393 212 (1998)

[6] M.Schmidt, Th.Hippler, J.Donges, B.v.Issendorff, H.Haberland and P.Labastie, Phys.Rev.Lett.87, 203402, (2001)

[7] R. Kusche, Th. Hippler, M. Schmidt, B. v. Issendorff, and H. Haberland, Eur. Phys. J. D9 1 (2000)

[8] H.Haberland, in Proceedings of the Les Houches Summer School (2000) on *Atomic Clusters and Nanoparticles*, should appear in 2002

[9] C. L. Cleveland, U. Landman, T. G. Schaaf, M. N. Shafigullin, P. W. Stephens, R. L. Whetten, Phys. Rev. Lett.79 1873 (1997)

[10] D.H.E.Gross, *Microcanonical thermodynamics: Phase transitions in "small" systems* Lecture Notes in Physics 66, (World Scientific, Singapores, 2001); see also Chaos, Solitons, and Fractals 13, 417 (2002) download: http://arXiv.org/abs/astro-ph/?cond-mat/0004268

[11] W.Thirring, Z.Phys. 235, 339 (1970)

[12] M.Schmidt, Th.Hippler, J.Donges, B.v.Issendorff and H.Haberland, Phys.Rev.Lett.86, 1191 (2001)

[13] F.Gobet, B.Farizon, M.Farizon, M.J.Gaillard, J.P.Buchet, M.Carreé and T.Märk, Phys.Rev.Lett.87, 203401 (2001)

Statistics and dynamics in finite system : Fragmentation of molecular cluster

B. Farizon, M. Farizon, M.J. Gaillard, F. Gobet,

Institut de Physique Nucléaire de Lyon,
IN2P3-CNRS et Université Claude Bernard,
43 boulevard du 11 Novembre 1918, F-69622 Villeurbanne Cedex, France

J.P. Buchet, M. Carré,

Laboratoire de Spectrométrie Ionique et Moléculaire,
CNRS UMR 5579 et Université Claude Bernard,
43 boulevard du 11 Novembre 1918, F-69622 Villeurbanne Cedex, France

P. Scheier, T.D. Märk

Institut für Ionenphysik, Leopold Franzens Universität
Technikerstr.25
A-6020 Innsbruck, Austria

Abstract

One of the great challenges in cluster physics in the last years was the identification and characterization of critical behavior and of phase transitions, including solid-to-liquid and liquid-to-gas phase transitions. Since clusters are particles of finite size one is confronted with the general question of how to detect and/or characterize such a transition in a finite system, a question of interest for many microscopic or mesoscopic systems such as for instance melting and vaporization of metallic clusters [1], Bose condensation of quantum fluids and nuclear liquid-to-gas transition [2].

In a strict sense, sharp second order phase transitions can only occur in the thermodynamic limit that is critical singularities only are present for a system with a large number of particles. In small systems such as two colliding nuclear or molecular systems fluctuations may wash out the signature of the phase transition [3] (see also [1]). Nevertheless, it has been demonstrated theoretically (see [2] and references therein) and also experimentally (see [4] and references therein) that finite systems may indeed exhibit critical behavior to be seen when studying inclusive fragment size distributions, scaled factorial moments, and anomalous fractal dimensions. For instance recent heavy ion collision experiments around the Fermi energy and cluster collision experiments around the Bohr energy (see [5] and references therein) have shown the formation of many different fragments in the exit channel of the reaction exhibiting a power law in total fragment size distributions. Such a power law, as described by the Fisher droplet model [6,7], is expected to hold for droplet condensation /evaporation near the critical temperature, indicating a liquid-to-gas second order phase transition. However, the recent work on the lattice gas model[1] demonstrates that a critical behavior is compatible with a first order phase transition because of the finite size effects.

High energy collisions (60keV/amu) of hydrogen cluster ions with an helium target have been completely analyzed on an event-by-event basis in a recently developed multi-coincidence experiment at the Institut de Physique Nucléaire de Lyon [3]:

- The most abundant decay channels have been studied quantitatively for these high energy cluster ions. This allows us to identify decay reactions and their underlying decay mechanisms responsible for the occurence of the U-shaped fragmentation pattern [8].

- Moreover, the data allows an unbiased look at the true nature of fragmentation including a statistical analysis in terms of fluctuations in the fragment size distribution [9,10]. The comparison with percolation models leads to evidence a transition which exhibits a critical behavior.
- By selecting specific decay reactions we can start after the energizing collision with a microcanonical cluster ion ensemble of fixed excitation energy. From the respective fragment distributions in these selected decay reactions we derive corresponding temperatures of the decaying cluster ions. The relation between this temperature and the excitation energy (caloric curve) exhibits the typical prerequisites of a first order phase transition in a finite system, in the present case signaling the transition from a bound cluster to the gas phase [11].

Acknowledgement

This work is supported by the Amadeus program of the French and Austrian governments

References

---

[1] M. Schmidt, T. Hippler, J. Donges, W. Kronmüller, B. von Issendorff, P. Labastie, and H. Haberland, *Phys. Rev. Lett.* **87** (2001) 203402

[2] F. Gulminelli and P. Chomaz, *Phys. Rev. Lett.* **82** (1999) 1402

[3] M. Belkacem, V. Latora and A. Bonasera, *Phys. Rev. C* **52** (1995) 271

[4] B. Farizon et al., *Phys. Rev. Letters* **81** (1998) 4108

[5] B. Farizon et al., *Int. J. Mass Spectrom. Ion Proc.* **164** (1997) 225

[6] M.E. Fisher, *Rep. Progr. Phys.* **30** (1967) 615

[7] J.E. Finn et al., *Phys. Rev. Letters* **49** (1982) 1321

[8] F.Gobet, B.Farizon, M.Farizon, M.J. Gaillard, S. Louc, M.C. Bacchus, J.P.Buchet, M.Carré, P.Scheier, and T.D. Märk, *Phys. Rev. Lett.* **86** (2001) 4263

[9] B.Farizon, M.Farizon, C. Guillermier, M.J. Gaillard, F.Gobet, J. Buchet, M.Carré, P.Scheier, and T.D. Märk, *EPJD* **5** (1999)

[10] F. Gobet, B. Farizon, M. Farizon, M.J. Gaillard, M. Carré, P. Scheier, and T.D. Märk, *Phys. Rev. A* **63** (2001) 033202

[11] F. Gobet, B. Farizon, M. Farizon, M.J. Gaillard, M. Carré, and T.D. Märk, *Phys. Rev. Lett.* **87** (2001) 203401

Basic Principles and Applications of Atmospheric-Pressure Discharge Plasmas

Kurt H. Becker

Department of Physics and Engineering Physics, Stevens Institute of Technology,
Hoboken, NJ 07030, USA

ABSTRACT

This presentation summarizes the principles that govern the generation and maintenance of atmospheric-pressure discharge plasmas. The properties and operating parameters of various high-pressure discharge plasmas such as dielectric barrier discharge plasmas, corona discharge plasmas, microhollow cathode discharge plasmas, and dielectric capillary electrode discharge plasmas are introduced. Several applications where atmospheric-pressure plasmas have gained prominence recently such as UV and VUV light sources, remediation of pollutants and waste streams, and surface cleaning will be discussed.

1. Introduction

Discharge plasmas at high pressures (up to and exceeding atmospheric pressure), where single collision conditions do no longer prevail, provide a fertile environment for the experimental study of collisions and radiative processes dominated by (i) step-wise processes, i.e. the excitation of an already excited atomic/molecular state and by (ii) three-body collisions leading e.g., to the formation of excimers. The dominance of collisional and radiative processes beyond binary collisions involving ground-state atoms and molecules in such environments allows for many interesting applications of high-pressure plasmas such as high power lasers, opening switches, novel plasma processing applications and sputtering, EM absorbers and reflectors, remediation of gaseous pollutants, and excimer lamps and other non-coherent vacuum-ultraviolet (VUV) light sources. A recent summary of various types of atmospheric-pressure discharge plasmas and their applications was given by Kunhardt [1].

2. Basic Principles of High-Pressure Discharges

Dielectric barrier discharges (DBDs), corona discharges (CDs), dielectric capillary electrode discharges (CDEDs), and microhollow cathode discharges (MHCDs) are all self-sustained, non-equilibrium gas discharges that can be operated at atmospheric pressure. CDs and DBDs represent very similar types of discharges. While DBDs are characterized by insulating layers on one or both electrodes, CDs depend on inhomogeneous electric fields at least in some parts of the electrode configuration to restrict the primary ionization processes to a small fraction of the inter-electrode region. At atmospheric pressure, the physical processes in both types of discharges are similar and resemble those in transient high-pressure glow discharges. In addition to pure CDs and DBDs, there are certain hybrid discharges, which are a mixture between a DBD and CD.

Usually, DBDs at atmospheric pressure consist of many tiny current filaments which are referred to as microdischarges. Homogeneous (i.e. diffuse, non-filamentary) discharges can be obtained under very special circumstances with plasma parameters that are quite different from filamentary DBDs. At atmospheric pressure, the discharge in a conventional DBD device starts with local gas breakdown at many points in the discharge volume. The gas breakdown in a DBD and the formation of microdischarges has been thoroughly studied and is fairly well-understood [2]. The discharge sequence encompasses four phases. The initial gas breakdown at sufficiently high electric fields is called the Townsend phase. Subsequently, the streamer or ionization phase leads to the formation of a highly conducting channel, a so-called filament with a diameter of about 0.1 mm and a current density of up to 100 A/cm^2. Charges are transferred through this channel and accumulate on the dielectric surface (phase 3) until the voltage across the filament is compensated and the discharge dies out (phase 4). The time scale for the completion of a full 4-cycle discharge development is of the order of 10^{-8} s. Typical conditions in a filament are as follows: electron densities up to 10^{14} cm^{-3}; average electron energies of up 20 eV, particularly in the narrow streamer head; gas temperatures only slightly above room temperature, 300 – 400 K. However, these conditions exist only in a filament, i.e. on the ns time scale and in very small spatial volumes.

Common CDs geometries have at least one electrode which favors the generation of highly non-uniform, locally high electric fields, e.g. point-to-plate, wire in a cylinder, knife-edge shapes electrodes, etc.). When the voltage is raised, current starts to flow at the corona onset and increases until the potential for spark breakdown is reached. This range of corona activity is called partial breakdown. The corona discharge is characterized by a faint glow in the region of high electric field accompanied by streamers propagating towards the other electrode. Even with dc pulses the appearance is that of a burst corona with regular current pulses. The physical mechanism of these current pulses is a regular build-up and removal of space charge that modulates the ionization in the high-field region. High concentration of radicals can be generated by using fast-rising high-voltage pulses which lead to the formation of streamers to bridge the gap between the electrodes. The properties of these streamers are similar to the streamers in DBDs (diameter of 0.1 – 0.2 mm, duration of a few nanoseconds, peak average electron energy of up to 20 eV at gas temperature near room temperature near the streamer head. Highest efficiency is achieved when the length of the exciting HV pulse equals the streamer transit time. Thus, the properties of a corona discharge are similar to those of a DBD in the filamentary mode.

The basis for the atmospheric-pressure operation of the CDED is a novel electrode design which uses dielectric capillaries that cover one or both electrodes. The capillaries, with diameters in the range from 0.01 to 1 mm and length-to-diameter ratios of the order of 10:1, serve as plasma sources which produce jets of high-intensity plasma at atmospheric pressure under the right operating conditions. The plasma jets emerge from the end of the capillary and form a “plasma electrode” for the main discharge plasma. The field inside the capillary does not collapse after the formation of the streamer discharge due to the fact that the high electron-ion recombination at the wall of the capillary requires a large ion production rate along the axis of the capillary in order to sustain the current. Under the right combination of capillary geometry, dielectric material, and exciting electric field, a steady state can be achieved. Run-away into the arc is prevented by the fact that the current through the capillaries is self-limiting, i.e. the gas density inside the capillary decreases with time due to gas heating which puts an upper limit to the conductivity as a result of gas starvation. Compared to other atmospheric-pressure discharge plasmas, the CDED plasma requires a lower sustaining voltage, lower energy input per cm^3 of plasma generated. CDEDs achieve plasma parameters (electron densities and average electron energies) in the bulk plasma that are much higher than the corresponding parameters in DBDs and CDs. In fact., the bulk plasma parameters in a CDED plasma are closer to the plasma parameters that are realized in the filaments of DBDs and CDs, average energy of the plasma electrons of up to 6 eV at gas temperature in the 350 - 400 K range and electron densities of up to 10^{14} cm^{-3}.

Another approach towards the generation and maintenance of a high-pressure discharge plasma is based on the hollow cathode (HC) discharge concept and exploits the inverse scaling of the hole diameter with the operating pressure which makes atmospheric-pressure operation possible, if the hole diameter is of the order of about 0.1 – 0.5 mm (microhollow cathode discharge, MHCD). HC discharges have been widely used since the early days of discharge physics and gaseous electronics as high-density, low-pressure discharge devices for a variety of applications [3-5]. A HC discharge device consists of a metallic cathode with a hole in the center and an arbitrarily shaped metallic anode. A HC discharge is created by confining the negative glow of the discharge to the cathode cavity. This is accomplished by an externally applied dc or a time-varying voltage applied to the electrodes which a potential trough in the cathode cavity that results in a strong acceleration of the electrons and a possible oscillatory motion (pendulum electrons). The trapped "pendulum electrons" [4,6,7], can undergo many ionizing collisions with the background gas thus creating a high-density plasma which emits intense radiation and is characterized by a very high current density (hollow cathode effect).

3. Selected Applications of High-Pressure Discharge Plasmas

Among the various applications of high-pressure discharge plasmas, novel light sources in the ultraviolet (UV) and vacuum ultraviolet (VUV) spectral region have gained prominence recently. MHCD plasmas have been used extensively for the generation of non-coherent UV and VUV excimer radiation using either pure rare gases, rare gas - halide mixtures, or gas mixtures of rare gases and molecular gases such as H_2, O_2, and N_2. Schoenbach and co-workers were the first to report excimer emissions from MHCD plasmas in Xe and Ar [8-13]. Subsequently, excimer emissions were also reported from MHCD plasmas in Ne and He [14,15]. Rare gas atoms have a $^1S_0$ electronic ground state. The lowest excited-states result from the promotion of a (np) valance electron to the (n+1)s-level (n=2,3,4,5 for Ne, Ar, Kr, Xe) leading to four "P-states", two of which are metastable, while the other two states decay to the ground state via dipole-allowed transitions . The most common routes to rare gas excimer formation are either via electron-impact ionization

(1a) $e^- + X \rightarrow X^+ + 2\,e^-$
(1b) $X^+ + 2\,X \rightarrow X_2^+ + X$
(1c) $X_2^+ + e^- \rightarrow X^* + X$
(1d) $X^* + 2\,X \rightarrow X_2^* + X$

where X = He, Ne, Ar, Kr, or Xe and the asterisk denotes a metastable rare gas atom, or alternatively directly via excitation of metastable rare gas atoms by electrons

(2a) $e^- + X \rightarrow X^* + e^-$
(2b) $X^* + 2\,X \rightarrow X_2^* + X$

In either case, the excimer molecules are formed in three-body collisions involving a metastable rare gas atom and two ground-state atoms. Efficient excimer formation requires (i) a sufficiently large number of electrons with energies above the threshold for the metastable formation (or ionization), and (ii) a pressure that is high enough to have a sufficiently high rate of three-body collisions. Minimum electron energies required for excimer formation range from 11 – 14 eV in Xe to 20 – 24 eV in He.

Rare gas excimer emission spectra are dominated by transitions from the lowest lying bound $^3\Sigma_u$ excimer state to the repulsive ground state (second continuum) [16,17] with peak emissions at 170 nm (Xe), 145 nm (Kr), 130 nm (Ar), 84 nm (Ne), and 75 nm (He). The so-called first excimer continua in the rare gases are observed on the short-wavelength side of the second continua and are attributed to the radiative decay of vibrationally excited levels of the $^1\Sigma_u$ excimer state. Most work to date has been carried out in Xe, Kr, and Ar, where the high-pressure MHCD can be "sealed off" with a window (LiF or MgF_2) for spectroscopic investigations of the excimer emissions in the 130 - 170 nm region. Studies of the Ne_2^* and He_2^* excimers, on the other hand, require an "open" MHCD source [14,15] connected directly to a VUV monochromator, since no material is transparent below 105 nm.

Kurunczi et al. [14] reported the emission of intense H Lyman-α emissions from MHCD plasmas in gas mixtures of high-pressure Ne with trace amounts of H_2. Kurunczi et al. [14] monitored simultaneously the Ne_2^* excimer emission and the Lyman-α emission and observed a dramatic decline in the Ne_2^* excimer emission when H_2 was added to the gas mixture. This provided direct experimental evidence that the near-resonant energy transfer reaction involving Ne_2^* excimers and H_2 molecules is the source of this intense atomic H emission. Ne_2^* excimers in the bound $^3\Sigma_u$ state have enough energy to dissociate H_2 and excite one of the H atoms to the n = 2 state. The subsequent decay of the excited H atom results in the emission of the 121.6 nm H Lyman-α line. Earlier, Wieser et al. [18] had observed a similar emission of intense, monochromatic H Lyman-α radiation from high-pressure gas mixtures of Ne with trace amounts of H_2 bombarded by high energy electrons and ions and first suggested the above near-resonant energy transfer process as the most likely mechanism leading to the emission of the H Lyman-α line [18] solely on the basis of spectroscopic studies of the Lyman-α emission. Further details of excimer light sources based on high-pressure discharge plasmas are given in the oral presentation.

Other applications of high-pressure plasmas that will be addressed in the conference talk include the remediation of gaseous pollutants from effluent gases and waste streams, the cleaning of conducting and non-conducting surfaces, and the decontamination of chemical and biological agents.

Acknowledgments

This work was supported by the NSF, DOE, and by DARPA/ARO. I gratefully acknowledge the contributions of Peter Kurunczi and Karl Schoenbach to the material presented in this article.

References

---

[1] E.E. Kunhardt, *IEEE Trans. Plasma Sci* **28**, 189 (2000)
[2] U.Kogelschatz, B. Eliasson, and W. Egli, *J. Phys. IV (France)* **7**, C4-47 (1997)
[3] F. Paschen, *Ann. Phys.* **50**, 901 (1916)
[4] A. Güntherschulze, *Z. Tech. Phys.* **19**, 49 (1923)
[5] A. Walsh, *Spectrochim. Acta* **7**, 108 (1956)
[6] H. Helm, *Z. Naturforg.* **27a**, 1712 (1972)
[7] G. Stockhausen and M. Kock, *J. Phys. D* **34**, 1683 (2001)
[8] A. El Habachi and K.H. Schoenbach, *Appl. Phys. Lett.* **72**, 22 (1998)
[9] K.H. Schoenbach, A. El-Habachi, W. Shi, M. and Ciocca M, *Plasma Sources Sci. Technol.* **6**, 468 (1997)
[10] K. H. Schoenbach, A. El-Habachi, M. M. Moselhy, W. Shi, and R. H. Stark, *Physics of Plasmas* **7**, 2186 (2000)
[11] M. Moselhy, W. Shi, R.H. Stark, and K.H. Schoenbach, *IEEE Trans. Plasma Science* (2001), submitted.
[12] A. El-Habachi and K.H. Schoenbach, *Appl. Phys. Lett.* **72**, 22 (1998)
[13] M. Moselhy, A. El-Habachi, K.H. Schoenbach, and U. Kogelschatz, *Appl. Phys. Lett.* **78**, 880 (2001)
[14] P. Kurunczi, H. Shah, and K. Becker, *J. Phys. B* **32**, L651 (1999)
[15] P. Kurunczi, J. Lopez, H. Shah, and K. Becker, *Int. J. Mass Spectrom*. 205, 277 (2001)
[16] W. Waller, U. Schaller, and H. Langhoff, *J. Chem. Phys.* **83**, 1667 (1985)
[17] D.C. Lorents, *Physics C* **82**, 19 (1976)
[18] J. Wieser, M. Salvermoser, L.H. Shah, A. Ulrich, D.E. Murnick, and H. Dahl, *J. Phys. B* **31**, 4589 (1998)

Experimental Electron Impact Ionization Cross Sections of Molecules for Plasma Processing

R. Basner, M. Schmidt, K. Becker[1)] and H. Deutsch

Institut für Niedertemperatur-Plasmaphysik (INP) Greifswald, Germany
[1)]Department of Physics and Engineering, Stevens Institute of Technology, Hoboken, USA

1. Introduction

Non-thermal low-temperature plasmas used in plasma processing are mainly composed of hot electrons (average electron energy 0.5 eV - 5 eV), cold ions, and neutral gas molecules, which both have energies corresponding to temperatures in the range of 300 K to 1000 K. In stationary plasma, the ion loss rate equals the ion production rate. Electron impact ionization of the neutral heavy particles in ground or in excited states is the initial, an important and in many plasmas the dominant ion formation process depending on the shape of the electron energy distribution function. The efficiency of a particular ionization process in the plasma is determined by the overlap of the electron energy distribution function with the respective cross section. The electron impact can produce the molecular ion by direct ionization and by dissociative ionization fragment ions and neutral products such as radicals and smaller neutral stable molecules. Thus, the dissociative ionization is not only important for the charge carrier production, but it is also an essential step in initiating plasma chemical reactions. However, the ions are even more important in the sheath regions of the plasma near the wall of the plasma reactor or near the electrodes where is a large potential drop. In this region, the ions are the main carrier of kinetic and potential energy, which may be transferred to the surface and which serves as the "trigger" for a number of processes there, e.g. recombination, sputtering, chemical reactions etc. Electron impact ionization has been studied since the 1930s. The experiments were developed in two general directions. One is to examine the ionization process at a very fundamental physical level and figure out the finer details of the process. The other one is to determine the probability of ion formation of the specific ions of a given target as a function of the electron impact energy, i.e., the partial ionization cross section on an absolute scale. The charge-weighted sum of all partial ionization cross sections then gives the total ionization cross section. Numerous general reviews have been published on the topic of electron impact ionization of atoms and molecules by this time. For example, we note the earlier summaries of Kieffer and Dunn [1], and Märk and Dunn [2], which include the unchanged fundamentals. Since the middle of the eighties the research is characterized by the improvement and/or new development of the experimental set-ups. The fundamental new aspect is to avoid or to correct ion loss at the extraction, transmission, and detection stage of the ion trajectory. Especially excess kinetic energy of fragment ions was found to be a cause of ion loss. Detailed information of the recent progress and the various experimental techniques is summarized in the reviews of Märk [3], Matt et al. [4], Becker et al. [5], Basner et al. [6] and in the numerous special references quoted therein. The primary emphasis of this contribution is our experimental investigation of the formation of positive ions of molecules for plasma processing.

2. Experimental details

The ionization cross-section measurements were carried out using a time of flight mass spectrometer [7,8] under single collision conditions with operating pressures not higher than 0.5 mPa measured by a spinning rotor viscosity gauge. A schematic diagram of the time of flight mass spectrometer (TOFMS) is shown in figure 1. The TOF-MS can be operated either in a linear mode using detector I or in a reflection mode using the reflector (grids: G_3, G_4, G_5) and detector II. Both detectors are micro channel plate detectors (chevron arrangement, 40 mm diameter) for ion counting. All measurements described here were performed with the TOF-MS operated in the linear mode. The ion efficiency curves were measured simultaneously for Ar and the molecule under study in a well-defined gas mixture in an effort to ensure identical operating conditions for the detection of the ions of each gas. The measured relative partial ionization cross sections were put on an absolute scale by normalization relative to the total Ar ionization cross section of 2.77 x 10^{-16} cm^2 at 70 eV [9]. Typically, the electron gun was operated using electron pulses of 90 ns width at a repetition rate of 15 kHz. The electron beam has a diameter of about 0.6 mm in the interaction region and the amplitude of the electron beam current is in the range from 1 - 10 µA with energy spread of about 0.5 eV (FWHM). The impact energy can be varied from 5 eV to 900 eV and the electron beam is guided by a weak magnetic field (200 G).

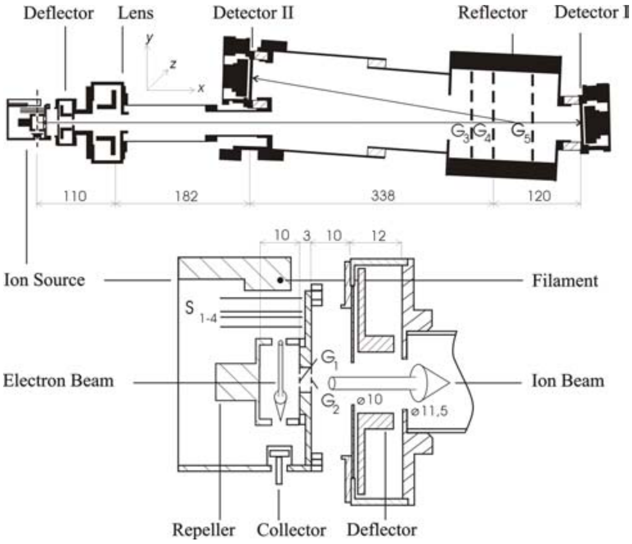

FIG. 1. Schematic diagram of the time-of-flight mass spectrometer (TOF-MS) and an expanded view of the electron impact ion source used in the present study (all dimensions are in mm): electron beam (tungsten filament, 0 - (-900) V); apertures: S_1 (0.5 x 4 mm^2, 22.4 V pre-acceleration), S_2 /S_3 (0.5 x 4 mm^2, 22.4 V or 70 V below the potential of the filament; pulsed), S_4 (0.4 x 0.4 mm^2, grounded); repeller (0 - ±3 kV); collision chamber exit aperture (6.5 x 6.5 mm^2, molybdenum grids (G_1, G2): transmission 90 %; grounded); flight tube entrance electrode (diameter 10 mm, 0 - ±3 kV); deflector (0 - ±500 V); Einzel lens (0 - ±13 kV); reflector (copper grids (G_3,G_4,G_5): transmission 94%); detector I and II (Galileo, 40 mm diameter MCP, active area 12.5 cm^2).

Extraction fields up to 3 kV/cm with a 10 ns rise time can be applied to the repeller at least 10 ns after the incident electron pulse passed through the ionization region. The output from the MCP-detector is preamplified and recorded with a 2 GHz multiscaler using a time resolution of 500 ps. Our TOF-MS was operated in such a way that no more than one ion is created during each electron pulse. This results in a higher number of sweeps and comparatively long data acquisition times, but ensures, on the other hand, that dead time corrections to the recorded signals are negligible. For this set-up the excess kinetic energy of fragment ions causes the following effects:

(i) The ion source region, which is normally determined by the spatial dimensions of the electron beam, is enlarged because of the motion of the ions during the time interval between their formation and their extraction.

(ii) The divergence of the extracted “ion beam” is enlarged both spatially as well as temporally due to the variation in the spatial positions and energies of the ions when the extraction pulse is applied.

Measurements of the ion extraction efficiency as a function of the delay time between the end of the electron pulse and the beginning of the extraction pulse to the repeller revealed constant ion currents for all fragment ions as long as the delay times were below a fixed value. This indicates that all ions from the extraction region of the ion source are transported to the detector under these conditions. Furthermore, extensive studies varying the voltages on the Einzel lens and on the horizontal and vertical deflection plates ensured that the diameter of the “ion beam” at the end of the flight tube is smaller than the diameter of the MCP (40 mm) for every fragment ion. We conclude that the experimental conditions necessary for 100% ion transmission of the ions from the ion source to the detector were established with the exception of ion loss at the grids G_1 and G_2.

Since our techniques relies on measurements of ratios of ions, the detection efficiency of the MCP for the reference ion and the various product ions of the gas under study must be the same. A series of experiments was performed to measure the ion count rate of a constant incident ion flux as a function of the ion impact energy for given operating voltages of the MCP and threshold levels of the multiscaler. Increasing the ion energy and the operating voltage of the MCP while decreasing the threshold level of the multiscaler revealed a saturation value of the recorded ion count rate. The saturation for doubly charged ions at the same ion impact energy always occurred at a lower operating voltage of the MCP as expected. A minimum threshold level of the multiscaler well above the noise level was selected in such a way that the ion count rate was saturated for all singly charged ions and for all doubly charged ions with twice the ion impact energies. We assume that the ion impact energy is high enough to guarantee a 100% counting efficiency for each ion hitting the front channel plate.

3. Results

In this contribution we present a summary of electron impact ionization cross-section results for titanium tetrachloride ($TiCl_4$) [7], tetrafluorosilane (SiF_4) [8], and hexafluoroethane (C_2F_6). $TiCl_4$ is used for the plasma-assisted chemical vapor deposition of titanium nitride films. SiF_4 is a gaseous product of fluorine-based plasmas for silicon etching and is used also in the plasma-enhanced deposition of thin silicon layers. C_2F_6 is well known as etching gas in the semiconductor industry.

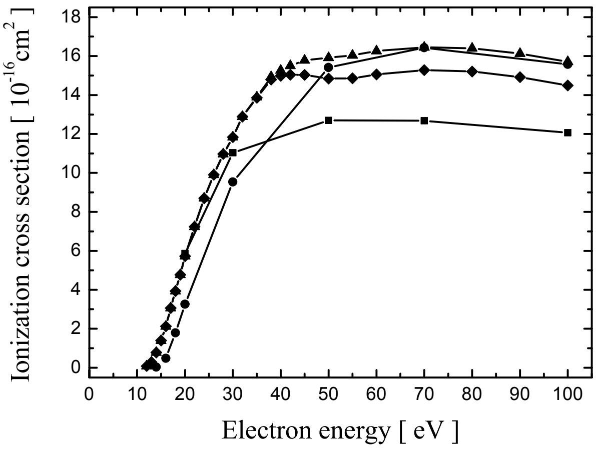

FIG. 2. Absolute total single $TiCl_4$ ionization cross section as a function of electron energy up to 100 eV, present experiment (filled diamonds) and calculated cross sections using the MAR [10] (filled squares) and the DM formalism [11] (filled circles). Also shown are the present results of the charge-weighted sum of the measured singly and doubly charged ions (filled triangles).

Dissociative ionization was found to be the dominant process for all three molecules. We found evidence of the presence of the $TiCl_4^+$ and SiF_4^+ parent ions in our experiments whereas no ion signals were detected that correspond to the formation of $C_2F_6^+$. Electron impact produces only singly charged fragment ions from C_2F_6 but singly and doubly charged fragment ions are formed from $TiCl_4$ and SiF_4.The experimentally determined total single ionization cross section of each molecule is compared with results of semi-empirical calculations [10,11] and reasonable agreement is found.

We studied the electron impact ionization of $TiCl_4$ for electron energies from threshold to 500 eV [7]. Absolute partial cross sections for the formation of all singly charged positive ions ($TiCl_x^+$ ($x = 1 – 4$), Ti^+, Cl^+) and for four doubly charged positive ions ($TiCl_x^{++}$ ($x = 1 – 3$), Ti^{++}) were measured. At lower impact energies up to 40 eV, the ion abundance varies drastically with impact energy, whereas at higher energies, two ionization channels dominate, the formation of the $TiCl_3^+$ fragment ion with a maximum cross section of 3.75×10^{-16} cm^2 at 100 eV and the formation of the Cl^+ fragment ion with a maximum cross section of 4×10^{-16}

cm^2 at 70 eV. All fragment ions with the exception of $TiCl_3^+$ are formed with excess kinetic energy. The cross section values of the doubly charged ions are about one order of magnitude smaller than those of the singly charged ions. The experimentally determined total single ionization cross section of $TiCl_4$ in comparison with results of semi-empirical calculations [10,11] and the total ionization cross section are shown in figure 2.

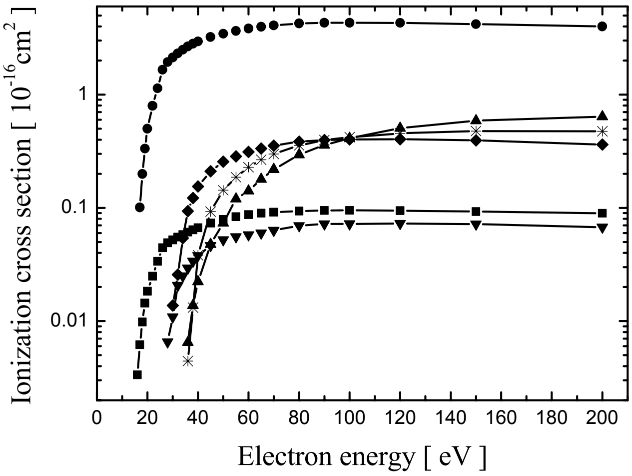

FIG. 3. Absolute partial SiF_4 ionization cross sections for the singly charged ions SiF_4^+ (filled squares), SiF_3^+ (filled circles), SiF_2^+ (filled inverted triangles), SiF^+ (filled diamonds), Si^+ (stars), and F^+ (filled triangles) as a function of electron energy up to 200 eV.

The absolute partial cross sections for the formation of various singly charged (SiF_x^+ (x = 1 – 4), Si^+, F^+) and doubly charged (SiF_x^{++} (x = 1 – 3), Si^{++}) positive ions produced by electron impact on SiF_4 were measured from threshold to 900 eV [8]. The SiF_3^+ fragment ion has the largest partial ionization cross section with a maximum value of 4.3 x 10^{-16} cm^2 at 90 eV. All other singly charged fragment ion cross sections are about one order of magnitude smaller at this impact energy (see figure 3). The cross section values of the doubly charged ions with the exception of SiF_2^{++} are about two orders of magnitude smaller .All fragment ions are formed with excess kinetic energy.

The measurements of electron impact on C_2F_6 include the partial ionization cross sections of $C_2F_5^+$, $C_2F_4^+$, C_2F^+, C_2^+, CF_3^+, CF_2^+, CF^+, C^+, and F^+ in the energy range from threshold to 900 eV. Fig. 4 shows the partial ionization cross section for the four most abundant fragment ions from threshold to

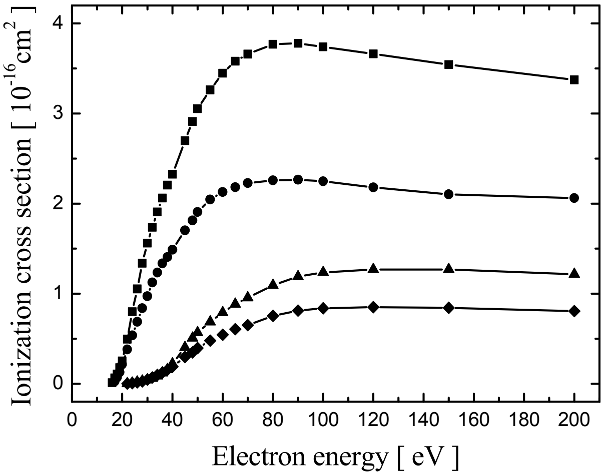

FIG. 4. Absolute partial C_2F_6 ionization cross sections of the fragment ions CF_3^+ (squares), $C_2F_5^+$ (circles), CF^+ (triangles), and CF_2^+ (diamonds) as a function of electron energy up to 200 eV.

200 eV. CF_3^+ is the fragment ion with the largest partial ionization cross section with a maximum value of slightly less than 4 x 10^{-16} cm^2 at 80 eV followed by the $C_2F_5^+$ partial ionization cross section with roughly half the maximum value of the CF_3^+ cross section. Other fragment ions that are formed with a maximum cross section of about 1 x 10^{-16} cm^2 are CF^+ and CF_2^+

References

[1] Kieffer, L.J., and Dunn, G.H.; *Rev. Mod. Physics* **38** (1966) 1

[2] Märk, T.D. and Dunn, G.H.; Electron Impact Ionization, Wien: Springer Verlag (1985)

[3] Märk, T.D.; in: Linking The Gaseous And The Condensed Phases Of Matter, edited by L.G. Christophorou, E. Illenberger and W.F. Schmidt, New York: Plenum Press (1994) 155

[4] S. Matt, T. Fiegele, G. Hanel, D. Muigg, G. Denifl, K. Becker, H. Deutsch, O. Echt, N. Mason, A. Stamatovic, P. Scheier and T.D. Märk; in: Atomic And Molecular Data And Their Applications, AIP Conference Proceedings 543 (2000) 191

[5] Kurt H. Becker and Vladimir Tarnovsky; *Plasma Sources Sci. Technol.* **4** (1995) 307

[6] Basner R, Schmidt M., Becker K, Deutsch H.; *Adv. in Atomic Molecular and Optical Physics* **43** (2000) 147

[7] R. Basner, M. Schmidt, K. Becker V. Tarnovsky, H. Deutsch; *Thin Solid Films* **374** (2000) 291

[8] R. Basner, M. Schmidt, E. Denisov, K. Becker, H. Deutsch; *J. Chem. Phys.* **114**, 3 (2001) 1170

[9] D. Rapp and P. Englander-Golden; *J. Chem. Phys.* **43** (1965) 5

[10] H. Deutsch, K. Becker, R. Basner, M. Schmidt, T.D. Märk; *J. Phys. Chem.* **102** (1998) 8819

[11] H. Deutsch, T.D. Märk, V. Tarnovsky, K. Becker, C. Cornelissen, L. Cespiva. V. Bonacic-Koutecky; *Int. J. Mass Spectrom. Ion Proc.* **137** (1994) 77

Recent Developments at the Atomic and Molecular Data Unit of the International Atomic Energy Agency

Robert E. H. Clark

Atomic and Molecular Data Unit, International Atomic Energy Agency

INTRODUCTION

The main purpose of the Atomic and Molecular (A+M) Data Unit of the IAEA is to establish and maintain databases in support of nuclear fusion energy research. This encompasses a very large number of processes in atomic, molecular, and plasma-material interaction physics. Data for these processes are supplied by research centres around the world participating in several different activities, such as Co-ordinated Research Projects (CRP), a Data Centre Network, and individual consultant agreements. The resulting data are incorporated into the databases maintained at the A+M Data Unit at the IAEA Headquarters in Vienna. These databases are now available through the world-wide-web.

This talk will focus on recent improvements and additions to these databases. Notable points include a new search engine developed by Yuri Ralchenko and Denis Humbert, energy and angle dependent data for physical sputtering and radiation enhanced sublimation, effective rate coefficients for several elements relevant to fusion machines, as well as some new interfaces in the web site. In the near future more data from recently concluded CRPs will be added. In addition, two new CRPs have recently started and a third is scheduled to begin in 2002. These CRPs will generate needed data on molecular processes affecting the edge plasma, data needed for diagnostics in fusion machines, and data for assessing the total tritium inventory in plasma machines.

SEARCH ENGINE

As the number of electronic databases available on the Internet increases, it has become increasingly difficult for any one user to become proficient in using them. Each site has its own format and the user must learn this format for each web site. Discussions have been held on the possibility of constructing one interface that could take a user request and formulate the request for each of several different databases. The requests would then be sent to each database in turn and the results returned to the user.

There is now a prototype of such an interface. Yuri Ralchenko of the Weizmann Institute in Israel and Denis Humbert of GAPHYOR in France have developed the search engine called GENIE. This search engine currently searches five different sites for radiative data and two sites for electron impact excitation and ionisation data. The format is simple and easy to understand. The underlying code is easy to expand for more databases and other types of data. The prototype version is available at the web sites at the IAEA, the Weizmann Institute, and GAPHYOR.

PHYSICAL SPUTTERING AND RADIATION ENHANCED SUBLIMATION

The CRP on “Plasma-Interaction Induced Erosion of Fusion Reactor Materials” produced a large volume of data on erosion of materials. This large volume of data was carefully evaluated by several members of the CRP. The best quality data were then fitted to physically realistic forms for angle dependence and for energy dependence. The resulting fits were checked for accuracy in reproducing the original data and to insure smooth behaviour over the entire range of validity. The results of this work were published in Volume 7B of the journal series *Atomic and Plasma-Material Interaction Data for Fusion.* The fit coefficients have been added to the online electronic database along with the evaluation functions so that users can obtain the data for arbitrary energy or angle.

EFFECTIVE RATE COEFFICIENTS

The computer modelling of non-LTE plasmas can be very time consuming. It is often the case that the densities are such that a simple coronal model is not sufficient. In such a case, each individual energy level of each ion must be included in the solution of the rate equations. This can result in massive amounts of data and solutions of very large sets of equations. In a CRP on radiative power losses in plasmas, many such lengthy modelling calculations were carried out. In addition to providing the calculated radiated power, effective ionisation and recombination rate coefficients were derived. These data were stored along with the populations of the ion stages as well as the total radiation from each ion stage. It is possible to use these data to interpolate in temperature and electron density to obtain the radiated power at an arbitrary temperature and density. In the steady state case this does not require the use of the effective rate coefficients. The effective rate coefficients are needed in the case of a plasma that is evolving with time. In that case it is possible to use interpolated effective rate coefficients to solve the time dependent problem and obtain the populations of each ion stage as well as the total radiated power. Since the effective rates coefficients do not require any explicit energy levels, this calculation is very quick computationally. These effective rate coefficients will soon be available on the A+M Data Unit web site.

NEW INTERFACES

Recent work by Jeff Stephens and Yuri Ralchenko has resulted in a preliminary version of a new interface to the bibliographic database at the A+M Data Unit. In the past, access to the bibliographic data was possible only through a Telnet session. That method is no longer adequate and a new interface was needed. While at the A+M Data Unit, Stephens did a large amount of work on the bibliographic database to bring it into a form suitable for more modern database management. During a recent period as a consultant, Ralchenko continued this work and put a preliminary version of an interface on the Unit web page. This interface allows the user to search the extensive bibliographic database by author and/or keyword. The resulting references are displayed along with a link to the home page of the journal where possible.

In may cases it is necessary to model a particular element for which data such as electron impact excitation cross sections, are not available. Such data may take a considerable time to generate. Often it would be of great value to have at least a good estimate of these data. This is now possible for electron impact excitation of atomic ions. During a consultancy visit to the Unit, James Peek installed a code for calculation of these cross sections using the so-called “average approximation”. Along with the cross section code, a version of the Hartree-Fock atomic structure code of R. Cowan was also installed. It is now possible to run these codes through an interface at the Unit web page. This allows the calculation of cross section versus impact electron energy for an arbitrary ion in a relatively short time, typically a second for each energy point. The calculations are all in configuration average mode only, no angular coupling to form LS terms is carried out. However, the results should be useful in cases where no other data exist. In most cases the average approximation is fairly accurate compared to a distorted wave calculation. The worst case is for singly ionised at very close to threshold energy, where the average approximation could be in error by as much as a factor of two. For higher ion stages and for higher energies, the average approximation is within approximately 10% of the distorted wave.

NEW CO-ORDINATED RESEARCH PROJECTS

In the past year two new CRPs have been started, one on the subject of “Data for molecular processes in edge plasmas”, the other on the subject “Atomic and molecular data for fusion plasma diagnostics”. Each CRP had a research co-ordination meeting last fall and each group formulated a plan for research in these areas. In addition a new CRP to assess the overall inventory of tritium in fusion reactors will start this year. This CRP will include processes that retain tritium as well as methods to release the tritium back to the plasma.

THE URL FOR THE ATOMIC AND MOLECULAR DATA UNIT IS:

http://www-amdis.iaea.org/

Electron Impact Ionization and Dissociation of Ions

P. Defrance

Université Catholique de Louvain, Département de Physique
Chemin du Cyclotron, 2, B-1348 Louvain-la-Neuve (Belgium)

Electron impact ionization of ions is a process playing a fundamental role in any discharge or plasma. Measurements of absolute ionization cross-sections for various ions have long been performed, in the case of single and double or even triple ionization. The data concern various ion species, negative and positive ones, including multiply-charged ions on which most of the recent measurements where focused. In addition to the direct electron ejection, experiments have demonstrated the significant — even dominant in some cases — contribution of indirect mechanisms to ionization processes. These mechanisms are inner-shell ionization or excitation followed by Auger emission of one or two electrons. Furthermore, some experiments have enlightened the existence and importance of resonant mechanisms such as resonant excitation followed by multiple autoionization.

When polyatomic ions are concerned, dissociation may also take place, following excitation or ionisation. In these cases, internal potential energy may be transformed into fragments kinetic energy. In the laboratory frame, these fragments exhibit angular and energy distributions which are much larger than the primary beam distributions. The angular dispersion is controlled by appropriate focusing elements but the spatial distribution of energetic fragments at the exit of the analysing device (here a double focusing magnet) is too large to ensure their total collection: the actual fraction of detected fragments is determined by scanning the magnetic field. A total transmission is achieved only for non dissociative ionization reactions, either atomic or molecular.

Let us consider the dynamics of dissociation fragments. The energy of a fragment ion (A^+) in the laboratory frame is given by:

$$E_A = \frac{m_A}{M}(E_M - q_M V_b) + \frac{\mu}{m_A}\Delta E_{CM} \pm 2\cos\theta\sqrt{\frac{\mu}{M}(E_M - q_M V_b)\Delta E_{CM} + q_A V_b} \qquad (1)$$

where E_M, M, q_M are the energy, mass and charge of the primary molecular ion, respectively. m_A and q_A are the mass and the charge of the fragment and μ is the reduced mass. ΔE_{CM} is the internal energy converted into kinetic energy (KER) released to fragments and θ is the emission angle of fragments with respect to the primary ion beam velocity. V_b is the collision region bias potential. From (1), it can be seen that the energy difference between fragments emitted forward ($\theta=0$) and backward ($\theta=\pi$) may be large (several tens of eV) even if ΔE_{CM} is small (a few eV). That difference represents the width of the product energy distribution which can be deduced from the magnetic field scan and this width allows the determination of the KER. A transformation of this distribution also leads to the transmission efficiency.

EXPERIMENTAL METHOD

In the experiments, the animated crossed beam method has been employed [1]. The cross electron-ion beam set-up is divided in three sections: the incident beam preparation section, the collision region and the analysis section. In the first section, the ion beam is formed after extraction from the ion source. This section includes a magnetic mass selector and appropriate optical elements [2]. In the collision region, the ion beam interacts with the ribbon electron beam. In the animated crossed beams method, the electron beam is swept across the ion beam in a linear see-saw motion at a constant speed. In the analysis section, product ions are magnetically separated from the primary beam which is collected on a Faraday cup. Finally, product ions are directed by an electrostatic deflector to the particle detector.

In the animated crossed electron ion beam method, the cross section is related to the measured quantities in the following way [1]:

$$\sigma = \frac{v_e v_i u K}{(v_e^2 + v_i^2)^{1/2} \left(\frac{I_i}{qe}\right)\left(\frac{I_e}{e}\right)} \qquad (2)$$

Here, u is the sweeping speed, K is the total number of events produced during one passage of electrons across the ion beam, v_e and v_i, I_e and I_i, e and qe are the velocities, currents and charges of the electrons and ions, respectively. In order to achieve good precision, careful measurements are needed for all the parameters in equation (1). Details of the apparatus as well as of the method are given in the reference [2].

RESULTS

Single and double ionisation of Krypton ions: q=10,18

At the meeting, I will review recent experimental and theoretical results concerning electron impact single and double ionization of Kr^{q+} (q=10-18).

The presence of ions formed in metastable states belonging to the ground configuration is observed for Kr^{12+}, Kr^{14+} and Kr^{16+} but for Kr^{18+}, the observed metastable state belongs to the lowest excited configuration. The important signals observed below the ground state ionization threshold indicate that the corresponding metastable state population is probably dominant for all the concerned ions. It is not possible to estimate the metastable population in the present experiment.

The comparison of experimental results with the prediction of the semi-empirical Lotz formula shows the dominant role of the excitation autoionization processes in the low energy range. The ACDW calculation performed for Kr^{18+} in the metastable only will be improved in order to explain most of the experimental observations. The results clearly show the increasing role of excitation to autoionising states via the 2p-3l transitions. One generally expects that the ionization cross section reduce as the ion charge increases. In the present study, the cross section for q=14 exceeds the one for q=15 above the 2p-3p excitation autoionization threshold. Detailed calculations should give an explanation of this effect.

It is interesting to relate the absence of any spectroscopic data corresponding to the present studied ions. The one and only source of information being the calculation of Blanke et al [3], the present energy data are, up to now, the first experimentally determined ionization and excitation thresholds for these ionic species.

The double ionization cross sections are dominated by L-shell ionization followed by autoionization for q > 14. This process is roughly estimated by the semi-empirical Lotz formula and the difference does not exceed 30 % at the maximum. The comparison with recent semi-empirical formulae shows that further improvement for these approaches is necessary. Resonant capture and excitation processes implying the L-shell are also obtained for charge states 14-16.

Ionisation and dissociation of polyatomic ions

Absolute cross sections for electron impact ionization, dissociative excitation and dissociative ionization of N_2^+ are reported in the energy region from threshold to 2.5 keV. The experimental procedure has been developed in order to separate the contributions from different ions with identical charge-to-mass ratio. The maximum KER for both dissociative processes are determined. The role of states contributing to different reactions is discussed. For dissociative excitation, present results are found to be much smaller than the results of Peterson et al. For ionization, (single and dissociative), a good agreement with their result is obtained as well as with the prediction of the model of Deutsch et al [4].

References

[1] Defrance P, Brouillard F, Claeys W and Van Wassenhove G 1981 *J. Phys. B: At. Mol. Phys.* **14** 103

[2] Duponchelle M, Zhang M, Oualim E M, Bélenger C and Defrance P 1995 *Nucl. Instr. Meth. Phys. Res. A* **364** 159

[3] Blanke J H, Fricke B and Finkbener M 1992 Database “Plasmarelevante Atomare Daten”, University of Kassel, Germany

[4] H. Deutsch, K. Becker, P. Defrance, U. Onthong, R. Parajuli, M. Probst, S. Matt, T.D. Märk *J. Phys. B : At. Mol. Opt. Phys. Letter*, (2002) in press

Collisional and Photon Induced Molecular Synthesis within ice mantles

N.J. Mason, A. Dawes, P. Tegeder and P. Holtom

Department of Physics and Astronomy, University College London, Gower Street, London, WC1E 6BT, United Kingdom

Multilayers of molecules condensed on bulk surfaces at temperatures below 270K are of great importance in several major areas of modern physical and chemical research;

(1) in the terrestrial stratosphere where they play a key role in the heterogeneous catalytic destruction of ozone on the surfaces of ice crystals in polar stratospheric clouds [1], and

(2) in the interstellar medium where they provide a 'habitat' for the synthesis of molecules [2], indeed such processes are postulated to underpin the formation of those prebiotic compounds that have been suggested to be the origins of life itself.

The interaction of photons, electrons and ions with a molecular adsorbate produces highly reactive species (radicals, cations, anions) which can subsequently react with neighbouring molecules to form new products and hence initiate further chemical and physical processes.

To date there have been few studies of the synthesis of molecules by collisions within multilayers and these are largely restricted to ***ion-molecule*** reactions. In a new research programme project we are studying ***neutral atom/molecule-molecule*** collisions stimulated by photon, electron and ion impact. Such processes have recently been shown to play an important role in stratospheric ozone depletion. Solar UV radiation dissociates the chlorine reservoir species OClO on the surface of ice crystals composing Polar Stratospheric Clouds (PSCs) [3] to form ClOO i.e.

$$h\nu + OClO \rightarrow ClO + O \qquad (1)$$

and subsequently,

$$ClO + O \rightarrow ClOO \qquad (2)$$

This is a process we may describe as ***photon induced isomerization*** of OClO. ClOO (chlorine peroxide radical) is thermodynamically more stable than OClO, but is kinetically very unstable and will quickly dissociate liberating Cl atoms which catalytically destroy ozone leading to an enhanced ozone loss in the stratosphere.

Such mechanisms can not occur in the gas phase since the kinetic energy of the dissociative fragments (ClO & O) is too high to allow reaction 2 to occur however such kinetic energies may be dissipated within the film and ClO and O trapped for sufficient time to allow ClOO to be formed.

Recently we demonstrated a second type of atom/molecule process within a thin film leading to the direct synthesis of a new molecular species within the multilayer. Low energy electron bombardment of a condensed molecular oxygen film was found to lead to the formation of significant concentrations of ozone through the following mechanism:

$$e^- + O_2 \rightarrow O + O \qquad (3)$$

$$O + O_2 \rightarrow O_3 \qquad (4)$$

the product ozone being detected by anion spectroscopy [4]. This mechanism is analogous to that proposed to occur in the gas phase in the Earth's stratosphere as part of the Chapman mechanism for ozone formation i.e.

$$h\nu + O_2 \rightarrow O + O \qquad (5)$$

$$O + O_2 + M \rightarrow O_3 + M \qquad (6)$$

M being a third body (usually O_2 or N_2) necessary to ensure that the produced ozone (formed in excited vibrational states) is de-excited to remain stable, within the multilayer adjacent oxygen molecules or the bulk may act as the third body M greatly enhancing the rate of molecular synthesis.

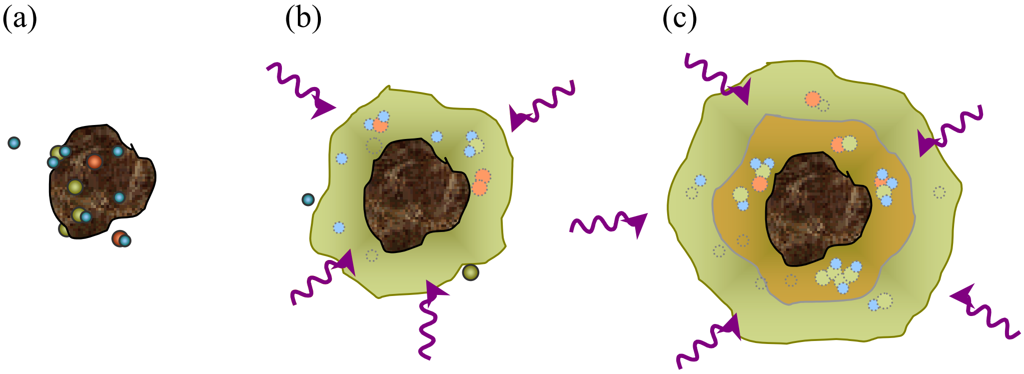

Figure 1: Molecular synthesis on a dust grain in Interstellar Space. (a) Atoms accrete to the cold grain surface. (b) An icy mantle is formed as atoms react to form simple molecules. The mantle is processed by stellar radiation as simple molecules are photolysed to form radicals, which react to form more complex molecules. (c) An inner mantle of organics is formed, protected by an outer layer of volatile ices.

Such processes may also occur in the interstellar medium (ISM) and may explain the synthesis of many of the molecular species recently observed by astronomical telescopes. For example in the ISM synthesis of many of the larger polyatomic species recently observed by the Hubble telescope (e.g. the amines, acetic acid and glycerol) may be explained by photolysis of trapped species in the ice mantles coating ISM dust grains (Figure 1). Most recently it has been postulated that *ion bombardment* of the ice surfaces of other planetary bodies can not only lead to the formation of new chemical species but can significantly alter the albedo of the planetary surface! For example abiotic ozone found on Rhea and Dione (two satellites of Saturn) and on Ganymede (a Jovian moon) is postulated to have been formed by high-energy charged particle impacts of oxygen or carbon dioxide molecules trapped in the water ice forming the surface of such satellites.

A prototype instrument has been constructed (figure 2) in which multilayers of ice with co-adsorbed molecular species may be formed on a cold substrate at temperatures compatible with the terrestrial atmosphere, the ISM or planetary bodies. These films maybe bombarded by UV irradiation, electrons and ions. Molecular synthesis within the mantle is probed by a combination of FTIR, UV-vis and mass spectrometry as a function of incident flux, energy and polarisation - the latter perhaps explaining the inherent chirality of biological systems. UV radiation is provided by tuneable lamp sources and, uniquely, by utilizing synchrotron radiation. Electron bombardment will be provided by using a high resolution electron gun and ion bombardment by using the research accelerator facilities at Queens' University of Belfast.

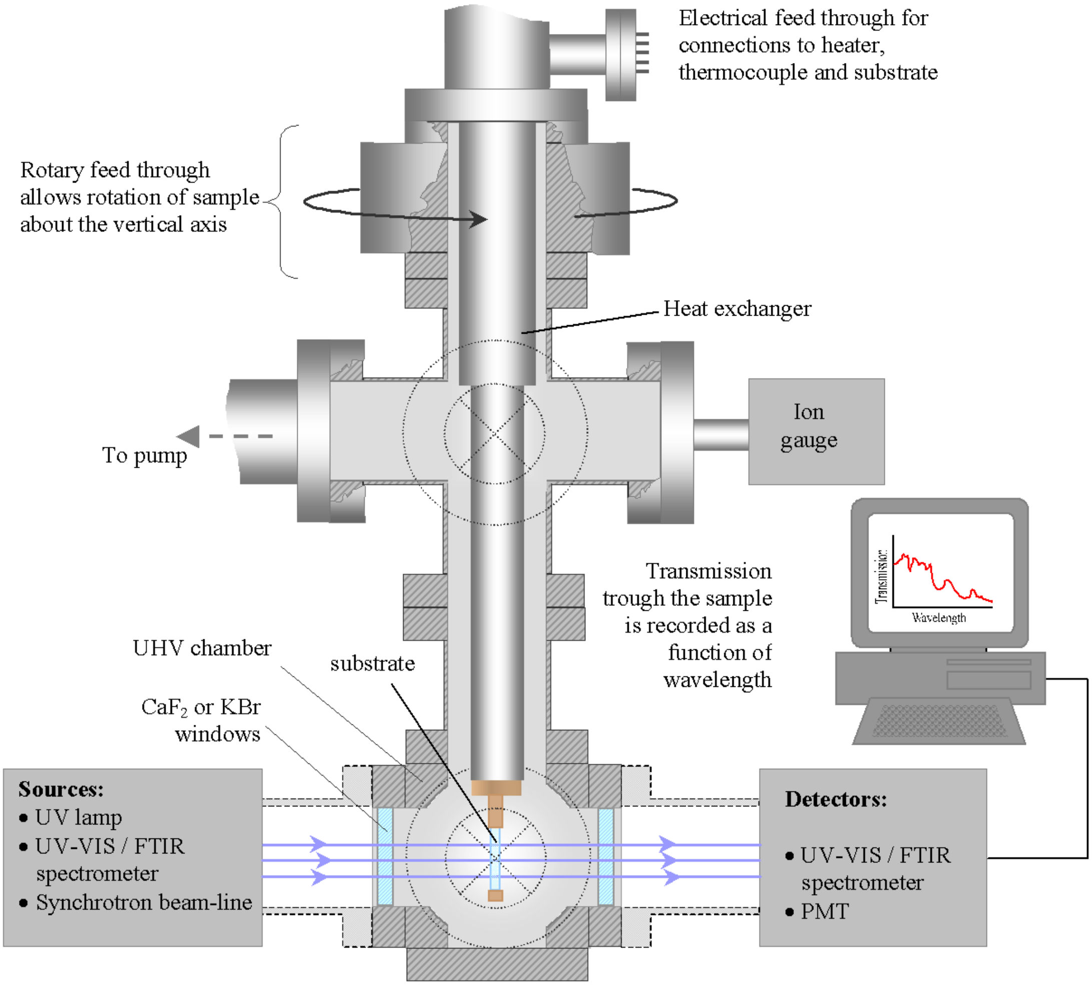

Figure 2: UCL Apparatus for Studying Synthesis in Ice Mantles

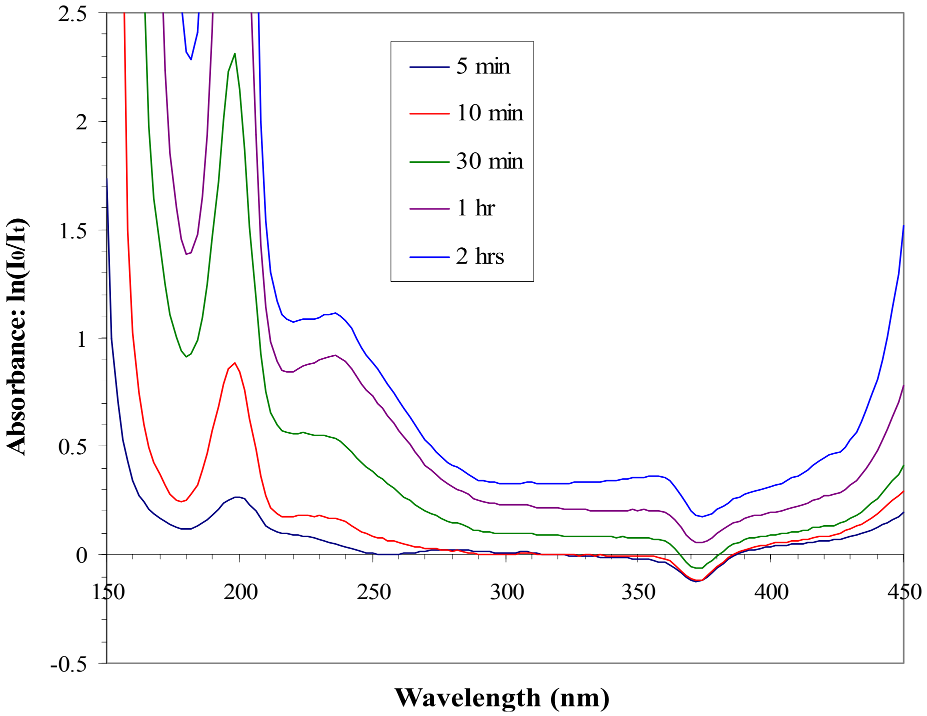

Figure 3: Photoabsorption spectra of water ice after various irradiation times with zero-order Synchrotron irradiation.

Figure 3 shows the first results of synchrotron irradiation of a water film. During the course of several hours continuous irradiation a new feature is observed at 235nm characteristic of the formation of OH radicals by photolysis of the water ice. These radicals are isolated and trapped in the ice but may subsequently react with neighbouring molecular species. An interesting (and unexpected) phenomenon was also observed around 370 nm where it appears that there is some luminescence from the ice (leading to a negative photoabsorption!). This may be due to the formation of excited O_2 molecules formed by the production of O atoms in the ice and has been observed in some earlier experiments using flash photolysis and electron irradiation.

These results and others will be discussed in this presentation and future experiments related to aeronomy, astrophysics, planetary albedo studies and the new scientific discipline of astrobiology will be described.

References

---

[1] T Peter *Annual Rev of Phys Chem.* **48** 785 (1997)

[2] W H Sorrell *Comments on Modern Physics section E* **1** 9 (1999)

[3] V Vaida, S Solomon, E D Richard , R Ruhl and A Jefferson *Nature* **342** 405 (1989)

[4] P Tegeder, P A Kendall, M Penno, N J Mason and E Illenberger *Phys. Chem. Chem. Phys.* **3** 2625 (2001)

Stable Isotopes in Global Change Research

Willi A. Brand

Max-Planck-Institute for Biogeochemistry, PO Box 10 01 64, 07701 Jena, Germany
Email: wbrand@bgc-jena.mpg.de

In a globally changing world the composition of the atmosphere, in particular the abundance of the trace gases plays an important role for life on earth as a whole. All organic matter is synthesized from water and CO_2, which contributes only 0.037 % to the gas volume of the atmosphere. This quantity, while seemingly small, is at the heart of our concern because the earth has seen an unprecedented rise of CO_2 in the last 200 years. An important property of CO_2 and other trace gases in the atmosphere is the ability to absorb infrared photons and thus retain some of the heat of the sun scattered at the surface of the earth that would otherwise be lost to open space. As a consequence the earth has become warmer in the past [1]. For mankind and life on earth as a whole the question is, how much more the average global temperature can increase before the consequences may become unbearable.

High precision concentration measurements of CO_2 were started in 1958 by C.D. Keeling in Hawaii and shortly after at the South Pole. These measurements have proven to be an invaluable tool, almost like an earth clinical thermometer, by tightly monitoring the continuous increase and inter- and intraannual variability of CO_2 as well as the phase difference of these properties between the hemispheres. Other trace gases like CH_4 and N_2O have since proven their importance as greenhouse gases or in connection with the ozone chemistry and today are closely observed in a large number of stations around the globe. Because of the small differences from year to year or inside functioning ecosystems quantification of the trace gases must be made with utmost precision, stretching the physical limits of existing analytical instrumentation.

CO_2 in the atmosphere is only a small fraction of the global CO_2 (most of it is dissolved in the world oceans) and carbon in CO_2 is only a small fraction of the global carbon cycle. In order to quantitatively understand the processes involved in the rise (and possible future decline) of CO_2 in the atmosphere, all sources and sinks of this gas must be considered and quantified over space and time. Due to natural fractionation processes, stable isotopes of carbon and also – to a lesser degree – of oxygen have proven to be one of the most valuable tools in understanding the fate of CO_2 during photosynthesis, respiration, biomass burning and fossil fuel combustion. The isotope ratios $^{13}C/^{12}C$ and $^{18}O/^{16}O$ must, however, be measured with very high precision over long time periods in the atmosphere and in fossil proxies of ancient atmosphere. Such proxies are for instance the large ice shields over Greenland and Antarctica. From measuring stable isotopes of oxygen in ice at the Vostok station we have a complete record of the climate changes of the last 440000 years with dramatic changes of the global temperature through several ice ages. From such studies we have learned that the current warm period that started about 10600 years ago is unusually stable. Most of the time, the earth was colder than today, interrupted by shorter warm periods. CO_2 concentration has remained below 300 ppm during the whole time frame covered, compared to 380 ppm today.

The presentation will focus on the role of stable isotope measurements or measurement techniques in our understanding of the changes of the global biogeochemical cycles, in particular the carbon cycle that we are witnessing at present.

---

[1] IPCC report 2001

Dissociation of macromolecules; a slow process studied with FTICR-MS

Ron M.A. Heeren

FOM-Institute for Atomic and Molecular Physics, Kruislaan 407, 1098 SJ Amsterdam, The Netherlands

Collisional induced fragmentation in ion traps is becoming more and more important as an analytical tool for structural analysis of macromolecular systems. Low energy activation techniques, which can be applied for extensive periods of time, are especially suited for macromolecular studies. The determination of activation and dissociation energies of high molecular weight macromolecules may provide insight into structures/conformations and functionalities of a wide scope of polymeric systems ranging from peptides, proteins and/or their complexes to industrial synthetic polymers. Gas-phase activation/dissociation studies on isolated/trapped macromolecular and/or their complex ions may potentially relate therefore bond energies with structural/conformational information in solution [1]. It is known that upon activation ions will gain internal energy which eventually can lead to dissociation [2-4]. Ions can also be excited to an internal energy level below the dissociation threshold [5]. This may cause slight changes in the conformations of macromolecules and/or their complexes prior to the occurrence of dissociation. Information on the correlation between small internal energy changes and conformational changes in biomacromolecules is of special interest for studies of non-covalent interactions in biomolecular complexes. The experimental determination of the influence of the collision energy, the initial ion temperature and even the mass of the ions on the conversion of kinetic energy into internal energy are subjected to further investigation.

The measurement of the internal energy deposition was achieved by the so-called pump-probe experiments. Details to construct ion breakdown diagrams at different temperatures have been published previously [5]. Briefly, the cell was first heated up to a certain temperature and then kept constant, while ions generated in the external ESI source were transferred into and trapped in the ICR cell. A delay of at least 60 seconds was set to allow the ions to equilibrate (thermalize) with the hot cell walls and eventually reach the temperature of the ICR cell by the absorption of IR photons during blackbody infrared irradiation. Then the ions were probed by a series of on-resonance excitations with different excitation energies to induce dissociation. The breakdown diagrams were constructed by plotting the ion survival yield of the isolated ions versus the laboratory-frame kinetic excitation energy.

To perform the ion survival yield versus the ion temperature (pump-probe) experiments, the ICR cell was also first heated up to a certain high temperature. After the ion introduction and isolation steps, the ions were pumped up to a certain internal energy level by blackbody infrared irradiation from the hot cell walls during the long thermalisation delay (60 s) and subsequently probed by an on-resonance collisional activated dissociation pulse with a fixed excitation energy. Then the heater was switched off and the temperature started to drop down. During this cooling process, a series of on-resonance collisional excitation pulses were applied to dissociate the ions and to probe the internal energy change at different temperatures by plotting the ion survival yield versus the temperature of the ions. In fact, three different but fixed laboratory frame kinetic energy pulses were applied to probe the internal energy change at different temperatures.

We have employed a very similar methodology for the separation isomeric structures, based on a difference in activation energy. The methodology is based on the creation of an isomerically depleted ion population. This depleted ion population is subsequently investigated by means of CAD and ECD to assess the occurring structures. This DoDIP

(Dissociation of Depleted Ion populations) method has been employed for the study of structural changes in synthetic polymers as well as the molecular aging phenomena in phospholipids from egg-tempera based paint systems. In addition FTICR-MS offers the possibility to perform a sequence of experiments to investigate the internal energy loss rate. Both experimental results, using our thermostated ICR cell and theoretical calculations demonstrate that the main internal energy loss mechanism after collisional activation is radiative cooling.

References

---

[1] Cooks, R. G. (ed). Collision Spectroscopy. Plenum Press: New York, 1978.

[2] McLafferty, F. W. (ed). Tandem Mass Spectrometry. Wiley: New York, 1983.

[3] Vekey, K. *J. Mass Spectrom.* **31** (1996) 445-463.

[4] Schukla, A. K.; Futrell, J. H. *J. Mass Spectrom.* **35** (2000) 1069-1090.

[5] Heeren, R.; Vekey, K. *Rapid Commun. Mass Spectrom.* **12** (1998) 1175-1181.

New View of the Surface of Salt Solutions with Implications for Atmospheric Chemistry

Pavel Jungwirth[1] **and Douglas J. Tobias**[2]

1) *J. Heyrovsky Institute of Physical Chemistry, Academy of Sciences of the Czech Republic, and Center for Complex Molecular Systems and Biomolecules, Dolejskova 3, 18823 Prague 8, Czech republic.*
2) *Department of Chemistry and Institute for Surface and Interface Science, University of California, Irvine, California 92697-2025, USA.*

It has been known for almost a century that simple inorganic salts raise the surface tension of water. Interpretation of this phenomenon via the Gibbs adsorption equation has led to the generally accepted picture of ions being repelled from the air/solution interface. Here, we report results from molecular dynamics simulations of a series of sodium halide air/solution interfaces. In all cases, the simulations reproduce the experimentally observed increase in surface tension relative to pure water. Analysis of the simulations reveals that the small, nonpolarizable fluoride anion is excluded from the surface in accord with the traditional picture. However, all the larger, polarizable halide anions (Cl^-, Br^-, and I^-) are present at the surface. Moreover, bromide and iodide exhibit surfactant activity, i.e. their concentration at the surface is higher than in the bulk. On the basis of the simulations a molecular picture of hydrogen bonding in the interfacial region, which can be tested by surface sensitive spectroscopic experiments, is developed. The novel microscopic view of the interfacial structure of aqueous salt solutions is in a stark contrast with the traditional belief (which, incidentally, is not supported by any direct measurements with molecular resolution) that the surface of aqueous electrolytes is devoid of ions. The results of the present simulations have also direct implications for reactivity of aqueous sea salt aerosols in the marine boundary layer, as well as for bromine chemistry on Arctic snow packs during the polar sunrise.

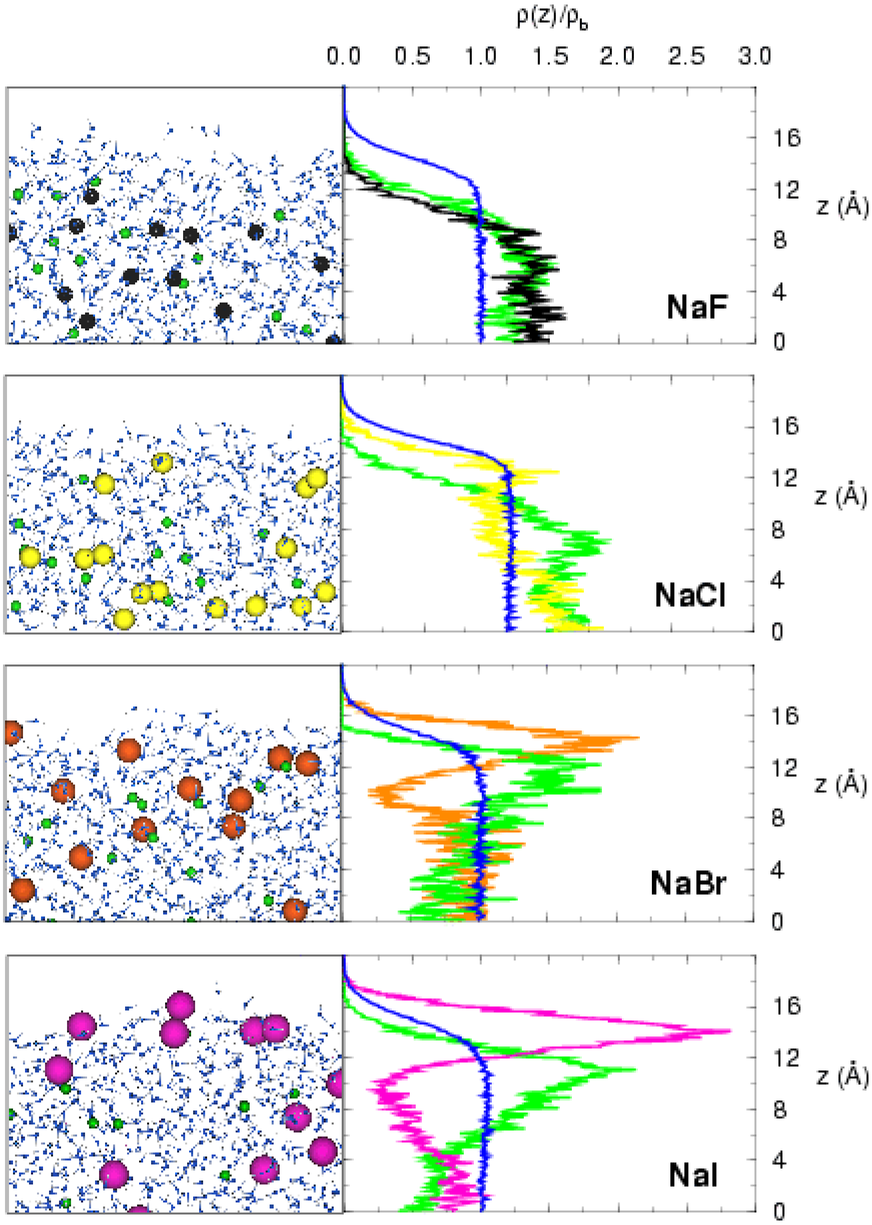

Figure1. Snapshots of the air/solution interfaces from the simulations (left) and the corresponding density profiles of the sodium and halide ions and water oxygens (right).

Electronic Spectra of Carbon Chains and their Relevance to Astrophysics

John P. Maier

Institute for Physical Chemistry, University of Basel, Klingelbergstrasse 80, CH-4056 Basel, Switzerland

The electronic spectra of neutral carbon chains, their cations and anions have been obtained in the gas phase. Three different approaches have been used. The transitions of the chain radicals $C_{2n}H$ n=3-6 and of the bare carbons C_4, C_5, have been detected by cavity ringdown spectroscopy with a supersonic slit-discharge source. The electronic spectra of the polyacetylene and cyanopolyacetylene cations such as $HC_{2n}H^+$ and $HC_{2n}CN^+$ n=2,3 have been measured at high resolution in cell and jet discharges at low temperatures using frequency modulation absorption spectroscopy. Carbon anion chains of the type C_n^- and C_nH^- with n in the range 3-10 have been studied by a two colour resonant photodetachment approach. The electronic transitions of very long polyacetylene chains $HC_{2n}H$ n-4-13 have also been detected in the gas phase by a two photon ionisations technique. The gas phase spectra obtained in the laboratory have enabled for the first time a direct comparison with astronomical measurements in the diffuse medium for polyatomic carbon chains to be made. The implications of this are discussed.